Filtration mechanism of suspensions of microgels

Swati Kaushik

université de BORDEAUX

THÈSE PRÉSENTÉE

POUR OBTENIR LE GRADE DE

DOCTEUR DE

L'UNIVERSITÉ DE BORDEAUX

ÉCOLE DOCTORALE DES SCIENCE CHIMIQUES

SPÉCIALITÉ : Physico-chimie de la matière condensée

Par

Swati KAUSHIK

Mécanisme de filtration des suspensions de microgel

Sous la direction de : Guillaume OVARLEZ

Soutenue le 13 fevrier 2019

Mme. RAVAINE, Valérie	Professeur, Université de Bordeaux	Président
M. CLEGG, Paul	Professeur, Université d'Edimbourgh	Rapporteur
M. PIGNON, Frederic	Directeur de Recherches, CNRS, Université de Grenoble Alpes	Rapporteur
M. BODIGUEL, Hugues	Professeur, Université de Grenoble Alpes	Examinateur
M. MEEKER, Steven	Ingénieur, Solvay	Examinateur
M. OVARLEZ, Guillaume	Directeur de Recherches, CNRS, Université de Bordeaux	Encadrant

Titre : Mécanisme de filtration des suspensions de microgel

Résumé : Les écoulements de suspensions dans des milieux poreux sont particulièrement complexes, notamment à cause du couplage d'écoulements de cisaillement et d'écoulements élongationnels (Herzig, Leclerc et Goff, 1970). On les retrouve fréquemment dans les applications industrielles, l'une des applications principales se trouvant lors des opérations de production de pétrole et de gaz. Lors de la construction d'un puits, des additifs polymères anti perte de fluide empêchent à plusieurs étapes l'écoulement de fluide entre le puits et la formation de roche poreuse environnante. La perte de fluide est un problème grave si elle n'est pas maîtrisée ; elle s'ajoute alors au coût total des opérations et pourrait surtout avoir des conséquences néfastes pour l'environnement et les opérateurs. Parmi les technologies disponibles, des additifs polymères connus sous le nom d'additifs anti perte de fluide, tels que des microgels et des particules de latex, sont ajoutés aux fluides injectés pour limiter les pertes de fluide (généralement de l'eau) via un mécanisme de colmatage / blocage de pores du support poreux.

Le comportement de blocage de beaucoup de ces additifs anti perte de fluide a été testé par des méthodes conventionnelles qui impliquent l'application d'une différence de pression élevée (typiquement 35-70 bars) sur le fluide formulé comprenant les additifs contre un filtre représentatif de la taille typique des pores de la formation (une grille métallique, de la céramique ou du papier filtre) et la mesure du volume de filtrat en fonction du temps. Cependant, ces méthodes standard ne permettent pas de comprendre le mécanisme sous-jacent de la dynamique de blocage des supports poreux. Par conséquent, une meilleure compréhension du mécanisme de blocage d'un support poreux par des additifs industriels anti perte de fluide est nécessaire.

Dans ce travail, nous utilisons des suspensions de microgels réticulés chimiquement comme additifs anti perte de fluide et nous étudions leur comportement de blocage dans des milieux poreux modèles transparents. Nous utilisons des dispositifs à base de polydiméthylsiloxane (PDMS) comme modèle de support poreux permettant l'observation directe du processus de blocage couplée à des mesures quantitatives. Nous fabriquons des dispositifs microfluidiques de filtration frontale et de filtration latérale avec différentes tailles de pores afin de déterminer comment des paramètres tels que la mouillabilité de la surface, la concentration en particules, la taille des particules et le débit affectent la formation du gâteau de filtration.

Nous présentons une méthode de contrôle de la taille des particules constituant les suspensions de microgels. Nous décrivons ensuite une approche pour préparer des suspensions à plus haute concentration et étudions la rhéologie des suspensions en fonction de la concentration en particules. De plus, nous présentons un procédé simple pour former un gâteau de filtration à partir de la suspension de microgels sur une membrane et estimons la perméabilité à l'eau du gâteau de filtration formé selon la loi de Darcy.

MOTS-CLÉS: Suspensions de microgels, Perte de fluide, Gâteau de filtration, Rhéologie, Milieux poreux, Microfluidique, Perméabilité.

Title : Filtration mechanism of suspensions of microgels.

Abstract : The flow of suspensions in porous media is a complex phenomenon due to the mechanisms involved such as both shear and extensional flows (Herzig, Leclerc, & Goff, 1970). Their use in industrial applications is quite extensive with one of the major applications being at various stages of oil and gas production operations. At several stages of a well construction, flow of fluid between the well and the surrounding porous rock formation is prevented thanks to the polymeric fluid loss control additives. Fluid loss is a severe problem if not controlled, which would add up to the total cost of operations and more importantly could have hazardous impacts on the environment or operators. Among several technologies industrially available, polymeric additives popularly known as fluid loss additives such as microgels and latex particles are added to the injected fluids to limit the loss of fluid (usually water) via the mechanism of pore clogging/jamming in porous media.

Many of these fluid loss additives have been tested for their jamming behaviour by conventional methods which involve the application of a high pressure difference (typically 35-70 bars) on the formulated fluid comprising of the additives against a filter representative of the formation's typical pore size (either a metallic grid, ceramic or filter paper) and the measurement of the filtrate volume versus time. However, these standard methods do not give any insight in understanding the underlying mechanism of jamming dynamics in porous media, hence, a better understanding of the mechanism of jamming in porous media by industrial fluid loss additives is needed.

In this work, we use chemically cross-linked microgel suspensions as the fluid loss additive and study its jamming behaviour in transparent model porous media. We make use of polydimethylsiloxane (PDMS) devices as model porous media which allows direct observation of the jamming process coupled with quantitative measurements. We fabricate microfluidic devices for frontal flow filtration and lateral flow filtration with different pore sizes to see how parameters like surface wettability, particle concentration, particle size and flow rates affect the filter cake formation.

We present a method of controlling the size of the microgel suspensions. We then describe an approach for preparing higher concentration suspensions and investigate the rheology of the suspensions as a function of concentration. Furthermore, we present a simple method of forming a filter cake of the microgel suspension on a supporting membrane and estimate the permeability of the filter cake formed for the flow of water using Darcy's law.

KEYWORDS: Microgel suspensions, Fluid loss, Filter cake, Rheology, Porous media, Microfluidics, Permeability.

Solvay- Rhodia Laboratoire du futur
[UMR 5258, 178 Avenue du Dr Albert Schweitzer, 33608 Pessac, France]

Acknowledgement

First of all, I would like to thank the director of the laboratory, Kazuhiko, for welcoming me to the laboratory. Profuse thanks to Dr. Paul Clegg, Dr. Frederic Pignon, Dr. Hugues Bodiguel and Dr. Valerie Ravaine for their participation to my thesis committee. I appreciate the very interesting discussions and their comments on the thesis. I also appreciate the precise and efficient reviewing of the complete thesis by the reviewers.

I would first like to express my deepest gratitude and appreciation to my supervisors Dr. Guillaume Ovarlez and Dr. Steven Meeker for advising, supporting me and giving their valuable insights throughout the course of this thesis. Their help, insight and encouragement were never missing. They gave me the keys to organise the work in an efficient, accurate and autonomous way. Thank you for the all the encouragement that allowed me to defeat my fears. I have learned a lot from you.

I owe sincere thanks to Prof. Wilson Poon for the insightful discussions and brilliant ideas. I have gratitude towards Dr. Pierre Guillot, Dr. Jacques Leng for the helpful discussions. I am greatly thankful to Dr. Emmanuel Mignard and Dr. Pascal Herve for his endless motivation and enthusiasm. I am grateful for having worked in a team full of brilliant and intelligent scientists both from academia and industry in LOF.

I would like to extend my gratitude to my colleagues in LOF, particularly Dr. Charles Loussert for his tremendous help regarding microscopy techniques and providing me motivation, Dr. Tristan Aillet for helping me pressure measurements, Dr. Laura Romasanta for being helpful especially in the early years of my thesis and sharing insights on my work, Ms. Sara De Cicco for help in scanning electron microscopy, Ms. Laetitia Pinaud for helpful discussion in rheology, Dr. Jeremy Decock for helping me with the permeability measurements set-up, Dr. Anne Bouchady for discussion in droplet drying setup and lastly, Gerald Clisson for assistance with microfabrication. I would like to appreciate all my colleagues and research teams in LOF for their cooperation, help and positive comments.

I am deeply thankful to Marie Curie Initial training network (Colldense) network for its funding and support. In addition, I am grateful to Solvay-Rhodia Laboratory of the Future for providing the lab equipments and other facilities that helped me accomplish my research objectives.

I want to thank my friends in Bordeaux who have shown tremendous support and have been kind throughout my PhD. I owe special thanks to Dr. Deewakar Sharma for helpful discussions and encouragement throughout these 3 years. A special thanks to Dr. Siddhartha De, Ms. Shaheen Pathan, Ms. Meghna Selvakumar, Mr. Vikas Jangid and Mr. Arvind Mehra for their endless support and enthusiasm.

Last but the not the least, I would like to express my special thanks to my uncle, Dr. Yogesh Kaushik and my aunt, Dr. Geeta Kaushik for inspiring me and my parents, Mr. Mukesh Kaushik and Ms. Anita Kaushik for their patience, support and encouragement.

This thesis is

dedicated to my family.

Table of Contents

List of Symbols

$\dot{\gamma}$	Shear rate (1/s)
γ	Shear strain (%)
σ	Shear stress (Pa)
σ_y	Yield stress (Pa)
η	Shear viscosity (Pa s)
η_s	Shear viscosity of solvent (Pa s)
G'	Storage/ Elastic Modulus (Pa)
G''	Loss/ Viscous Modulus (Pa)
M	Torque (Nm)
Ω	Angular frequency (1/s)
θ	Angular displacement (rad)
ϕ	Volume fraction (-)
ϕ_m	Maximum packing fraction (-)

ϕ_j Jamming fraction

c Concentration (% wt)

c_i Initial Concentration (% wt.)

c_j Jamming concentration (% wt.)

c_m Maximum jamming concentration

$\mathcal{K}$ Permeability (m^2)

k_0 Voluminosity

K Geometric factor

ε Self crowding factor

ϕ_p Porosity

R_e Reynolds number

n Power law index

k Consistency factor ($Pa\ s^n$)

List of Figures

List of Tables:

Chapter 1

Introduction

Table of Contents

1.1 Background

The recovery of oil and gas from the porous rock structure is a complex process for any industry dealing with it. The complexity of the procedure arises due to the fact that the oil is extracted from rock formations that are situated miles below the surface of the earth where the temperature and pressure are very high. These very high pressures within the rock formations from which the oil is to be extracted has to be carefully dealt with to avoid uncontrolled leaks of oil or gas at any time. The highest risk is when the well is built, as the hole is drilled through several formation layers with varying porosities, fluids composition, pore pressure and temperature. Leaks from an oil well can sometimes only cause some minor production issues but it can also lead to catastrophic leaks, causing injuries or casualties to the operating crews and a dramatic impact on the environment. On a general basis in the design and implementation of the construction of a well, hydrostatic overpressure (versus pore pressure) is applied on the open hole section to prevent any splintering or blowout from the formation. As a consequence, to maintain balance, it is also necessary to prevent leaks from the operating fluids (drilling mud, cement slurries or completion fluids) towards the formation.

There has been a growing interest in new chemical polymeric products used as fluid loss additives which prevent the flow of fluids between the well and the surrounding rock formations in the last 30 years. The interest has grown with the environmental regulations imposed by various organisations that restrict the use of toxic and non-ecofriendly chemicals in oil exploration in order to maintain and preserve the marine ecosystems. Another reason lies in the increasing technical challenges associated with unconventional resources exploitation. Indeed, these so called unconventional resources such as shale gas or shale oil are typically found in deeper rock formations than conventional reservoirs with increased operating temperatures and circulation or pumping times requirements. In addition the engineering of wells to exploit such reservoirs are also much more complex than conventional ones. Indeed, well construction implies directional, long deviated horizontal sections drilling and isolation as well as multiple well pad drilling operations.

In the next section, we will throw some light on the different processes involved in the drilling and construction of a well to explain issues associated with the lack of control of fluid loss. More detailed information on current techniques on the cementing operations can be found in the Petroleum Engineer's Guide to Oil Field Chemicals and Fluids by Jonannes Fink ("Chapter 1 - Drilling muds," 2015; "Chapter 2 - Fluid loss additives," 2015).

The construction of a well involves several successive operations of drilling and cementing. The main technical features are presented here below:

I. Drilling

Drilling of a well is completed by several stages of openhole drilling where rock is literally drilled by a rotational drill bit which crushes and penetrates the rock formations. Throughout this process drilling mud is injected from the inside of the drill string through nozzles at the drill bit into the wellbore. This drilling mud has several functions: cooling the drillbit, lubricating the contact points, lifting the rock cutting up to the surface and applying hydrostatic pressure towards the bottom hole formation.

Drilling fluids are usually classified in two categories: water based drilling fluids and oil based drilling fluids, based on the continuous phase used (Guichard, 2008). In water based drilling fluids, water is the continuous phase and is at least 50% of the total volume of the composition. It contains viscofiers to change the rheology of the mud. For example, mixing mixed metal hydroxides with Bentonite drilling mud imparts an extremely shear thinning behavior to the mud. Other additives include fluid loss control agents, weighting agents, emulsifiers, pH control agets, salts etc. Oil may also be present in small amounts. In oil base drilling fluids, hydrocarbon oil is the continuous liquid phase with other additives like clays and asphalts in order to get the desired viscosities.

The density of the drilling fluid is usually adjusted by addition of heavy colloidal particles such as barium sulphate (barite) or by the addition of highly concentrated salts. These drilling fluids are

dense enough and apply sufficient hydrostatic pressure to compensate the bottom hole pore pressure and prevent splintering, kicks or blowout of underground fluids. Typically drilling fluids are designed to be used when about 35 bars of excess pressure is applied against the formation. Nevertheless to ensure smooth operations it is of utmost importance that minimal loss of base fluid from the mud towards the formation occurs. This ensure that the rheology, density and lubricating properties of the fluid are stable throughout the circulation of mud against the formation. This is where fluid loss control additives play a crucial role. Fluid loss control additives limit fluid loss towards the formation typically by forming a thin impermeable layer at the interface between the borehole and formation.

II. Casing and Cementing

Once a stage of drilling is completed according to well planification, casing and cementing are performed. Typically the sections to be cemented can be of several hundreds of meters. Stages are limited by the pore pressure balance between the top and the bottom of the well against rock fracturation pressure. Indeed, if excessive overbalance is applied on the surrounding rock formation, a fracture may open and dramatic losses occur. As a consequence, every section is cased and cemented to ensure a safe progression of the drilling and zonal isolation of the well. A steel casing is placed downhole. As soon as the casing is fitted, the annular space between the casing and the formation is filled with cement (see Figure 1-1).

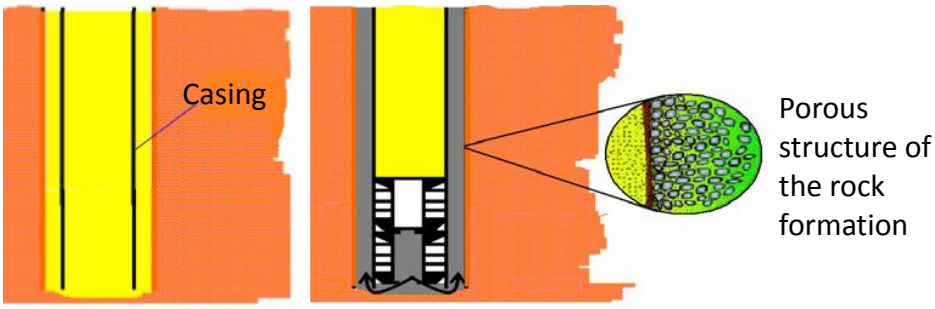

Figure 1-1 Schematic representation of the well bore with the steel casing and porous rock formations

The most commonly used cement slurries in oil wells consists mostly of Portland cement and occasionally Pozzolanic admixtures. On account of operational limitations on cementing jobs, no fillers or coarse particles are used in O&G cement formulations. Once placed against the formation, the cement is left to set i.e. it develops compressive strength on hydration (formation of hydrate phases from dissolution-reprecipitation from anhydrous cement particles). Once set, the cement sheath forms an impermeable barrier ensuring zonal isolation which should remain very stable over years (/decades) and safely seal the well.

Several cement additives are needed to operate cementing jobs. Setting time is controlled through the addition of retarders (and sometimes accelerators), density and rheology control additives are also critical to ensure a pumpable yet stable slurry is designed.

Here again as for drilling, the cement slurry is pumped from the inner casing and forced up through the outer casing against the rock formation. During placement the overpressure against the formation is typically considered to reach 70 bars, thus severe filtration processes may occur, and as cement is a fairly concentrated solid dispersion viscosity divergence may clog and block the annular space which is only a few centimeters wide. In the case of partial or irregular filling of the annular space, leaks can occur as well as casing degradation. Fluid loss control is thus a key component of all cement designs.

Role of Fluid loss control additives

In both operations of drilling and cementing, fluid loss control additives are crucial ingredients of the fluids formulation. They ensure that the base fluid remains in the wellbore and prevent invasion into the formation while fluids are being pumped with large overpressure. At early stages of the fluid placement or circulation against the formation, an impermeable filtercake is formed through a tangential filtration process. The filter cake can be “external” at the surface of the formation, consisting mostly of fluid loss additive and solids present in the fluid (bentonite, barite, cement…) or “internal” within the first few millimeters of the rock formation, which is plugged

by the penetration of the fluid loss additive. Once the filter cake is formed, ideally with minimal loss of fluid, the wellbore remains stable and further filtration is very limited.

There have been many fluid loss additives developed by the O&G industry over the past decades to ensure smooth and efficient operations. These additives may be categorized in 2 types. One is based on linear polymers which, through interaction with the suspended solids, seals the filter cakes porosity. The second type of additives are based on particulate additives such as colloidal latexes or prehydrated cross-linked starches, other natural polymers or synthetic microgels.

This thesis will focus on this second category of additives and specifically on synthetic microgels. Fluid loss control though porous rock formations is usually considered to be achieved by the plugging of the rock pores by soft deformable cross-linked particles. These soft deformable microgel particles may penetrate to some extent into the pores of the rock formations to clog the throats. Figure 1-2 shows the schematic of the mechanism of fluid loss control.

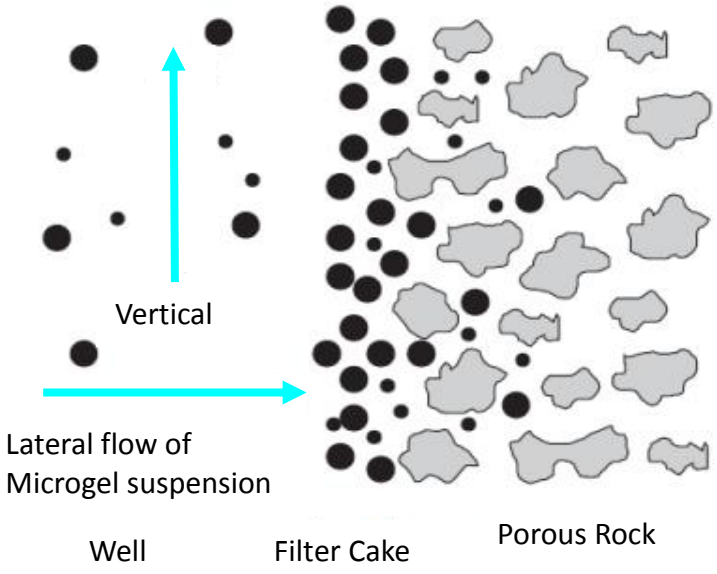

Figure 1-2 Schematic showing the flow of fluid loss additives in both vertical and lateral direction resulting in the formation of the Filter Cake (Image reproduced from:Petroleum Engineer's Guide to Oil Field Chemicals and Fluids by Johanees Fink (Fink, 2015)).

In the case of microgels as fluid loss control additives, either drilling fluids or cement slurries contain suspended soft deformable particles which move laterally from the borehole towards the rock formations as the fluid is pumped vertically with excess pressure. The rock formation being porous acts like a sieve retaining the suspended particles and forming a thin layer of filter cake.

1.2 Research Objectives and Goals

The main objective of this thesis is to study the jamming dynamics of a microgel suspension in porous media and investigate the fluid loss mechanism and the filter cake build up. To answer these questions, we perform experiments that help us understand the mechanism better. These experiments aim at:

- Developing model microfluidic porous media to mimic the frontal and lateral filtration processes.

- Visualizing directly the build up of the filter cake in the porous media using phase contrast microscopy.

- Designing an experimental protocol to have a better control over the size of the microgel particles (as the suspension provided by Solvay is quite polydispersed) and develop a method to prepare high concentration suspensions.

- Characterizing the bulk rheology of the microgel suspension as a function of concentration to better understand the mechanical properties of the concentrated jammed microgel or filter cake in porous media.

- Designing an experimental set up and procedure to measure the permeability of the filter cake using Darcy's Law.

- Understanding how properties like surface wettability, particle size, pore size and flowrates affect the jamming of the microgel suspension in porous media.

- Demonstrating fluid loss in real time in porous media with dilute microgel suspensions.

1.3 Research Methodology

1.3.1 Microgel

Microgel suspensions are cross-linked (either chemically or physically) soft particles that are swollen in a good solvent (Saunders & Vincent, 1999). The term 'Microgel' was first coined by Baker (Baker, 1949) to describe cross-linked polybutadiene latex particles. The 'micro' refers to the size of the particles and the 'gel' part came as a consequence of the swelling of particles in a good solvent (in Baker's case it was an organic solvent). Staudinger and Husemann were the first to synthesize microgel particles in the laboratory (Staudinger & Husemann, 1935).

The definition of a microgel particle is inclusive of the following criteria:

1. The particle size range is between 10nm to 100µm
2. They are dispersed in a solvent
3. They are swollen in a solvent
4. They have stable structure. The stabilization of the polymer network can be either due to covalent or physical forces.

I. Preparation

The microgel suspension used in this work is a **chemically cross-linked** industrial microgel suspension (available at about ~4% wt. active in water) provided by Solvay. It is synthesized by copolymerization of monomers. It is a loosely cross-linked microgel with an amphiphilic character. The polymer chains are chemically cross-linked to provide stability so that the microgel particles maintain a permanent structure. The microgel suspension in its original state is found to be highly

polydispersed, we call it **inhomogeneous microgel** or simply **Microgel-IN.** Owing to the high polydispersity (which we will later see in chapter 2), it is recommended to get rid of the bigger particles to have a narrower particle size distribution for applications in model porous media. To achieve this, we used two techniques to prepare suspensions of smaller and narrower particle size distribution: (A). Ultra-turraxing and (B). Centrifugation.

A. Ultra-turrax/ Mechanical Cutter

We use a disperser (T18 ULTRA-TURRAX disperser, IKA) at speeds, 3500, 7000 and 11000 RPM for 5 mins each which acts as a mechanical cutter to break the bigger microgel particles (see Figure 1-3).

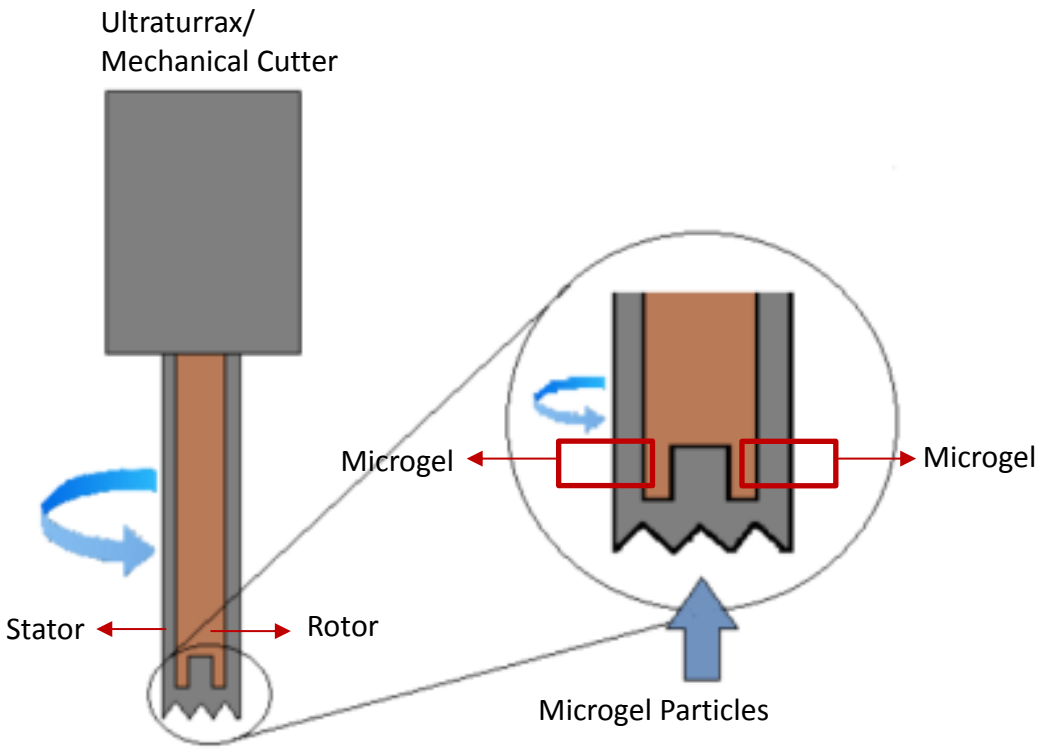

Figure 1-3 Schematic showing the process of the mechanical cutting of big microgel particles to yield a smaller particles.

The mechanical cutter comprises a rotor within a stationary stator. As the circumferential speed is very high, the particles to be dispersed are drawn axially towards the dispersion head. Due to the small gap and high speed (which corresponds to the cutting speed), the shear forces break

the particles into smaller ones. These smaller particles then move radially outwards through the slots available in the rotor-stator arrangement.

B. Centrifugation

For centrifugation, the Microgel-IN is first diluted with water to achieve a concentration of 0.9% wt. This 0.9% wt. of Microgel-IN is then taken in 50ml Corning vials and centrifuged at different speeds for 10 mins using JOUAN B4 Centrifuge by Thermo Scientific (see Table 1-1 for the centrifugation conditions and sample names given). After centrifugation, 72.5% of the total volume of the supernatant is slowly extracted using pipette.

Of the centrifugation conditions mentioned in Table 1-1, only Microgel-2000-10 and Microgel-4000-10, along with Microgel-IN were used for further experiments for a thorough comparative study in this work. The centrifuged supernatants of different concentrations were obtained by keeping the samples in a convection oven at 50°C for 2-10 days depending on the desired concentration.

Table 1-1 Table denoting the centrifugation conditions used for Microgel-IN and the sample names given to the supernatants.

Centrifugation Speed (rpm)	Time, t	Sample name
1000	10 mins	Microgel-1000-10
2000	10 mins	Microgel-2000-10
3000	10 mins	Microgel-3000-10
4000	10 mins	Microgel-4000-10

For Microgel4000-10, the highest concentration of homogenous suspension we are able to achieve is 6% wt. and it is 5% wt. for Microgel2000-10. For Microgel-IN, this concentration is 4.2% i.e. the same as received. As we tried to prepare microgel suspension of concentration higher than the aforementioned limit, we get a lumpy suspension which is not homogenous at all (see Figure 1-4).

Figure 1-4 Images of microgel suspensions with concentration, c > 6% wt. and >5% wt. for Microgel4000-10 and Microgel2000-10 respectively.

1.3.2 Particle Size Measurements

Particle size measurements were performed using light scattering (Malvern Mastersizer 2000, Malvern Instruments Ltd, Malvern UK). In this technique, a laser beam of wavelength 600nm is allowed to pass through the sample. The intensity of the light scattered by the particles is detected/measured by the photodetector. The volume of the particles is then calculated by using Mie theory (Rawle, 2010). The wavelength of the light changes when it transverses through the particle. This technique requires knowledge of the refractive index of both solvent and the particles. It should be noted that Mie Theory assumes the particles to be spherical. The collimated laser beam passes through the particle and the distribution of the scattered beam is recorded by the photosensitive detector as a series of concentric rings (see Figure 1-5). This distribution of the scattered intensity is analysed by the computer to give the particle size distribution. The distribution gives measurements like mean particle size ($d_{0.5}$), the surface weighted mean ($d_{3,2}$), and the volume weighted mean ($d_{3,4}$) often referred to as the De Brouckere Mean diameter (explained in detail in chapter 2). These average sizes obtained from light scattering are equivalent of to that of a sphere. The techniques is adavantageous in several aspects like it is simple to use, non-intrusive (low power laser), fast, has a wide size range (1- 1000 μm), no calibration required and highly versatile.

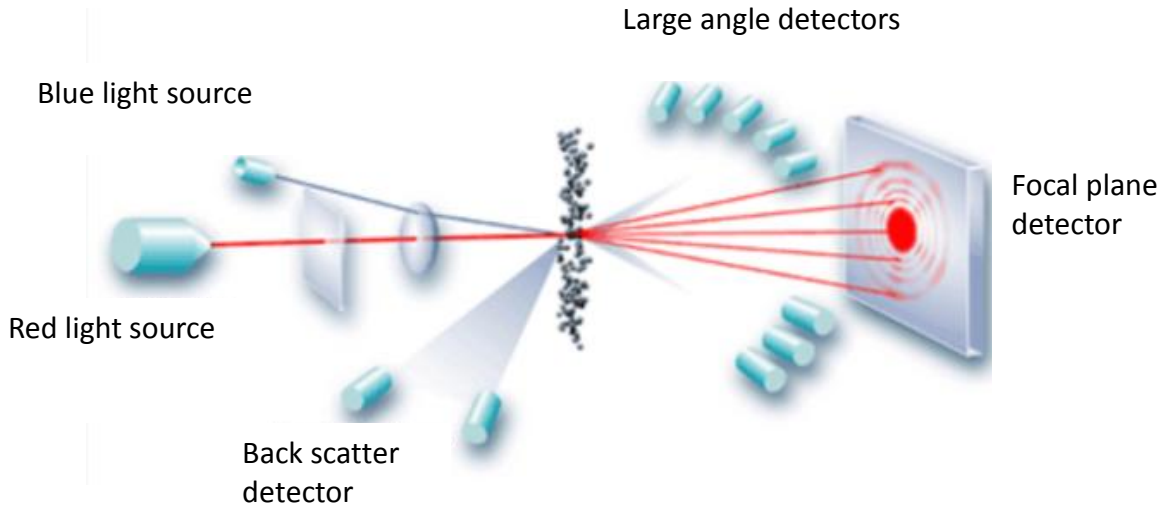

Figure 1-5 Schematic of a typical light diffraction system (Source: (PDF) (Report) https://www.tcd.ie/CMA/misc/particle_size.pdf)

1.3.3 Moisture Determination

We used an IR Moisture Analyser (Model IR 60, Denver Instruments) to measure the dry mass of the microgel suspensions. The IR moisture analyse offers fast analysis time, efficient and high repeatability for measuring the moisture content in the samples using thermogravimetric method. It works by drying the sample and registering the weight loss. The IR rays penetrate through the interior of the sample and subsequently are converted to heat energy which triggers the evaporation, thus drying the sample (see Figure 1-6).

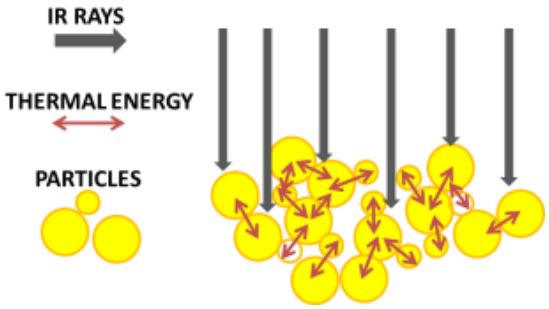

Figure 1-6 Schematic showing how IR rays works in the analyser to evaporate the sample and measuring the dry mass of the sample.

The wet samples are placed in an aluminium pan inside the analyser and dried at a temperature of 120°C. For dilute samples, the initial mass taken is around 5-10 g and for concentrated ones,

we take around 2-5 g. The heating stops automatically when the weight stabilizes which happens when all the solvent evaporates. The analyser then calculates the percentage solid content from the mass lost.

1.3.4 Rheology

I. Rheometer

All the rheological measurements were carried out in a Malvern Ultra+ stress controlled rotational rheometer. This rheometer can be used in both stress controlled and strain controlled mode. In the stress controlled mode, the torque or stress is applied to the sample at the desired level and the angular motion is detected . In the strain controlled mode, the feedback from the sample is used to adjust the torque to get the desired shear rate. All the experiments in this thesis are performed under the stress controlled mode. Figure 1-7 shows the schematic of the stress controlled rheometer. The stress controlled rheometer have good torque sensitivity, and the fact that stress and strain are measured in the same shaft lowers down the cost of the instrument however its major limitation is the instrument inertia.

The optical encoder measures the angular displacement. It consists of a non contacting light source and an array of photocell which is arranged on both the sides of an transparent disk attached to the shaft. The optical encoder can detect displacements as small as 50 nRad. There is another stationary disk present between the light source and the encoder disk. As the two disks interacts, a light pattern is generated and this pattern is detected by the photocell. When the sample is strained on the application of a stress, the encoder disk moves and disturbs the pattern. This change in the light pattern is detected and digitalised to give the data. This data is related to the defelection of the disk and therefore gives a value of the strain (Macosko & Larson, 1994).

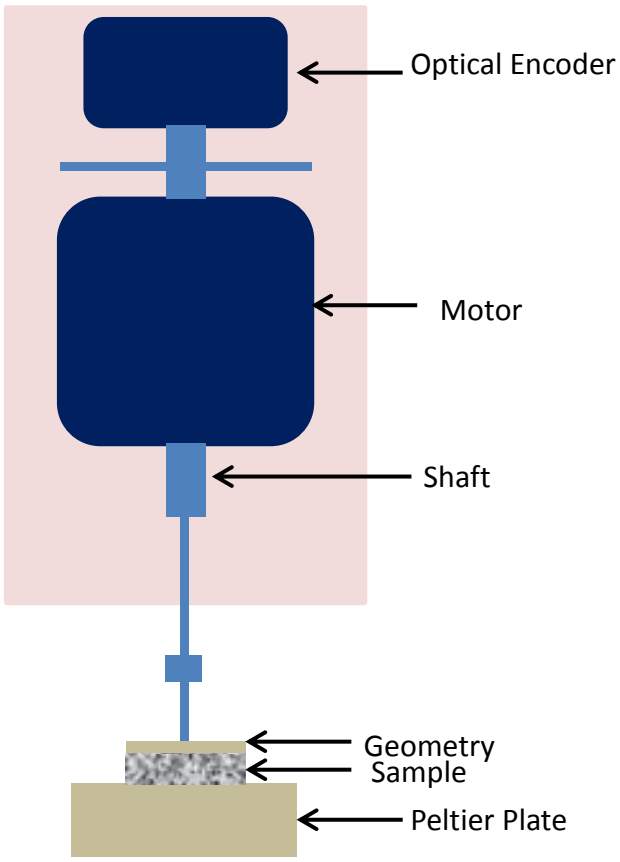

Figure 1-7 Schematic diagram showing a typical stress controlled rheometer main unit.

II. Geometries used:

We used three different types of geometries for the rheological measurements. The choice of the geometry was based on how concentrated and viscous the sample is. Table 1-2 summarizes the different geometries used for different concentrations of the microgel suspension.

Table 1-2 Table denoting the rheometer geometries used for varied concentrations of Microgel-IN, Microgel4000-10 and Microgel2000-10. (SDG= Smooth Double gap geometry, SBCP= Sand blasted cone and plate geometry (Cone angle-4°).

Microgel-IN		**Microgel-4000**		**Microgel-2000**	
Concentration (%wt)	Geometry used	Concentration (%wt)	Geometry used	Concentration (%wt)	Geometry used
0.8%	SDG	0.1%	SDG	0.1%	SDG
1.8%	SDG	0.3%	SDG	0.3%	SDG
2.2%	SBCP	0.5%	SDG	0.4%	SDG
3.3%	SBCP	0.8%	SDG	0.7%	SDG
4.2%	SBCP	0.9%	SDG	1%	SDG
		1.9%	SDG	1.9%	SDG
		2.3%	SDG	2.5%	SDG
		2.9%	SDG	2.9%	SBCP
		3.1%	SBCP	3.1%	SBCP
		3.5%	SBCP	3.9%	SBCP
		4.6%	SBCP	5%	SBCP
		6%	SBCP	6.9%	SBCP
		6.8%	SBCP	8.5%	SBCP
		7.5%	SBCP		

We now describe briefly the three geometries used, their working equations along with their advantages and disadvantages.

A. Double gap geometry

In this axially symmetric geometry, the fluid sample stays between the coaxial and stationary surface (red portion in the Figure 1-8) (Macosko & Larson, 1994).

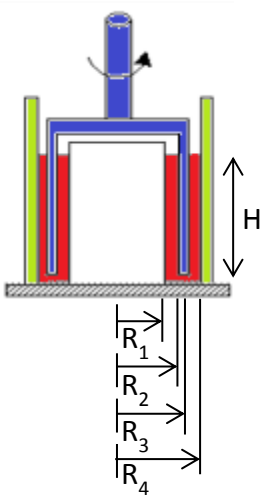

Figure 1-8 Schematic illustration of the Double gap geometry (red portion represents the fluid sample, blue represents the rotor, green is the static part)(Image source: google images)

The torque (M) on the rotor is given as

$$M = \frac{4\pi\,\sigma\,(\delta^2 R_3^2 + R_2^2)}{1 + \delta^2}$$

where, $\delta = \frac{R_4}{R_3} = \frac{R_2}{R_1}$, is the aspect ration, σ is the nominal shear stress

The shear rate, $\dot{\gamma}$ is a product of the geometrical factor (K) and the angular velocity (Ω)(rad/s) and K is given as

$$\frac{2R_4^2}{R_4^2 - R_3^2} = \frac{2R_2^2}{R_2^2 - R_1^2}$$

So, shear rate, $\dot{\gamma}$ can be written as

$$\dot{\gamma} = \frac{2R_4^2\,\Omega}{R_4^2 - R_3^2}$$

Pros
Low stress measurements
Large contact area
Cons
Difficult to clean
Not easy to run temperature ramps

B. Cone and Plate geometry

A cone and plate geometry gives constant shear rate, $\dot{\gamma}$ across the diameter of the plate (Macosko & Larson, 1994).

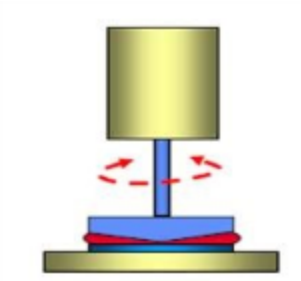

Figure 1-9 Schematic of the cone plate geometry used. (Image source: Google (https://polymerinnovationblog.com/rheology-thermosets-part-2-rheometers/)).

In our experiments, we used a 40mm/4° sand blasted cone and plate geometry. The shear rate, $\dot{\gamma}$ is given as

$$\dot{\gamma} = \frac{\Omega}{\tan\theta}$$

where, Ω is the angular rotation in rad/s and θ is the angle of the cone plate. Shear stress is also uniform across the diameter of the plate and is given as

$$\sigma = \frac{3M}{2\,\pi\,R_{Plate}^3}$$

where, M is the torque (in Nm), R_{plate} is the radius of the plate. The only disadvantage of using a cone and plate geometry is the small gap (~0.14mm) between the tip of the conic plate and the bottom plate. This small gap is not suitable when working with sample with big aggregates of particles as it can break the particles and can lead to errors in measurements. To avoid this, the parallel plate geometry is the best option where the gap can be changed according to the user's preference.

Pros
Uniform shear rate
Cons
Drying
Small fixed gap
Not good for particle greater than 1/10th of the gap distance

C. Parallel plate

In the case of the parallel plate geometry, the shear rate is not constant across the diameter of the plate. The fluid experiences greater shear rate at the edges than at the centre of the plate (Macosko & Larson, 1994).

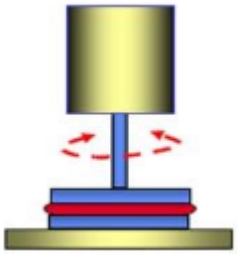

Figure 1-10 Schematic of the parallel plate geometry used. (Image source: Google (https://polymerinnovationblog.com/rheology-thermosets-part-2-rheometers/))

The equation for the shear rate for Newtonian fluids is given as

$$\dot{\gamma} = \frac{R_{plate}\Omega}{h}$$

And the shear stress is given as,

$$\sigma = \frac{2M}{\pi R_{Plate}^3}$$

where, Ω is the angular rotation, M is the torque (in Nm), R_{plate} is the radius of the plate, h is the gap between the plates.

Pros
Can alter gap and deal with large particles
Cons
Shear rate varies across the plate

1.3.5 Optical Imaging

All the imaging of the microgel samples and microchips are done using an Olympus IX51 microscope. Uniform illumination to have high contrast images is achieved by Koehler illumination. The steps are of Koehler illumination are as follows:

- Focus on the sample and then decrease the size of the field iris diaphragm so that its edges can be clearly seen.
- Using the condenser knob, focus on the edges of the field iris diaphragm.
- Once the edges are in focus, center the field iris image using the condenser- centering knobs.
- Then open the focussed and centered field iris diaphragm so that its edges just stay beyond the field of view.
- After this, the condenser iris is adjusted to increase or decrease the contrast of the image.
- The light intensity is adjusted using the lamp.

After the sample is uniformly illuminated following the above steps, the imaging of the sample or the microchips is done. In this thesis, we have employed bright field imaging and phase constrast imaging as imaging technique.

I. Bright Field Microscopy

For experiments where very high contrast was not need, we used bright- field microscopy with white light. The light contrast in the image is caused by the transmission through the dense areas in the sample.

II. Phase Contrast Microscopy

This technique of microscopy was invented by Frederik Zernike in 1930s prior to Electron Microscopy. Phase contrast Microscopy was a useful technique to view transparent samples like biological speciment and still continues to be. It is a vital technique used to view transparent and colourless samples like biological cells. Staining the sample is another alternative process that can be used but in biological systems, staining may hinder some processes. Phase contrast microscopy was invented to view as well as study living cells. A Nobel Prize was awarded to Frederik Zernike in 1953 for the same. We used two different objectives, 4X and 10X with the annular rings.

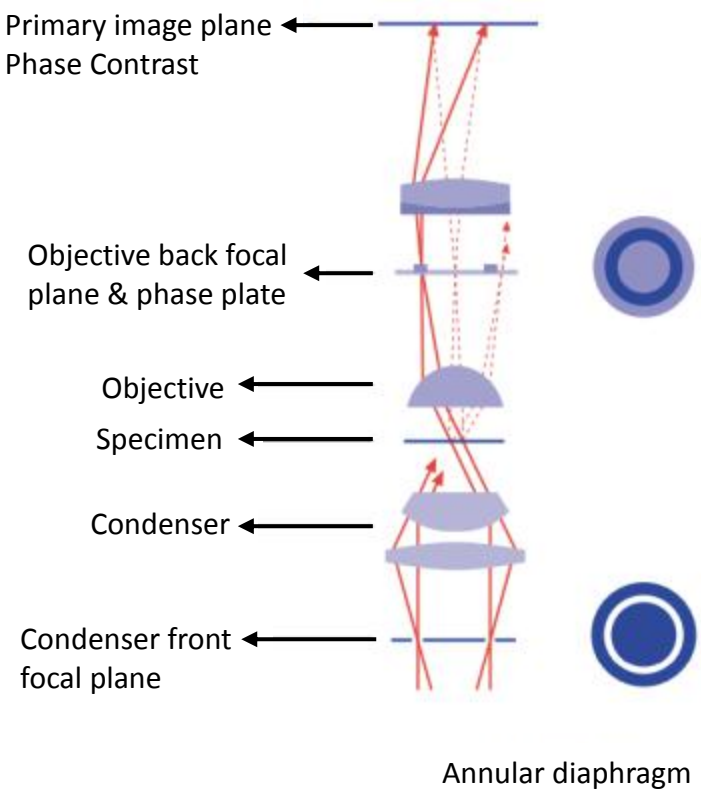

Figure 1-11 A typical Ray diagram of phase contrast. The solid red lines denote the un-diffracted beam and the dashed lines represent diffracted beams. Reproduced from Plasek and Reischig (J, 1998)

1.3.6 Microchannel Fabrication

I. Mask Design

All the photomasks used in this work were designed using Clewin software. The mask printing was done by CAD/Art Services, Inc, Oregon, USA. The final mask obtained were transparency sheets with transparent and opaque region denoting the desired geometry.

II. Fabrication of Silicon Master Moulds

We fabricated Silicon master moulds (for PDMS stamps) in a clean room using a photolithography technique. We used SU8 negative photoresist (SU8 3035 and 3050, Microchem) because it has a very high mechanical stability and gives a very high aspect ratio. The SU8 photoresist is spin coated on the silicon wafers at different speeds to get the desired heights. Different SU8

photoresists are available, each have different viscosities and give different heights ranging from 1-500 micron. The desired spin coating speed is made available on the calibration curve in the manual supplied by the resin supplier. Figure 1-13 illustrates the fabrication protocol (single step height) of the silicon moulds. The stages involved in one step photolithography are as follows:

i. The resin is spin coated on the Si wafer.
ii. The Si wafer with the thin layer of resin is then soft baked on a hot plate.
iii. The resin is then illuminated by UV (~365 nm) selectively using the photo masks. UV exposure assists in the cross linking of the resin exposed.
iv. Post exposure bake (PEB) is done to strengthen the cross linking.
v. After PEB, development is done to remove the unexposed areas.
vi. Hard bake is done to improve the adhesion of the resin on to the Si wafer.
vii. Development to remove the soluble parts.

For the soft bake, PEB and hard bake, the temperature and duration of baking depends on the thickness and type of resin used. Two step photolithography is done to get two step channels. step (vii) of developement is skipped and all the other steps are repeated for the stepped part of the microchannel.

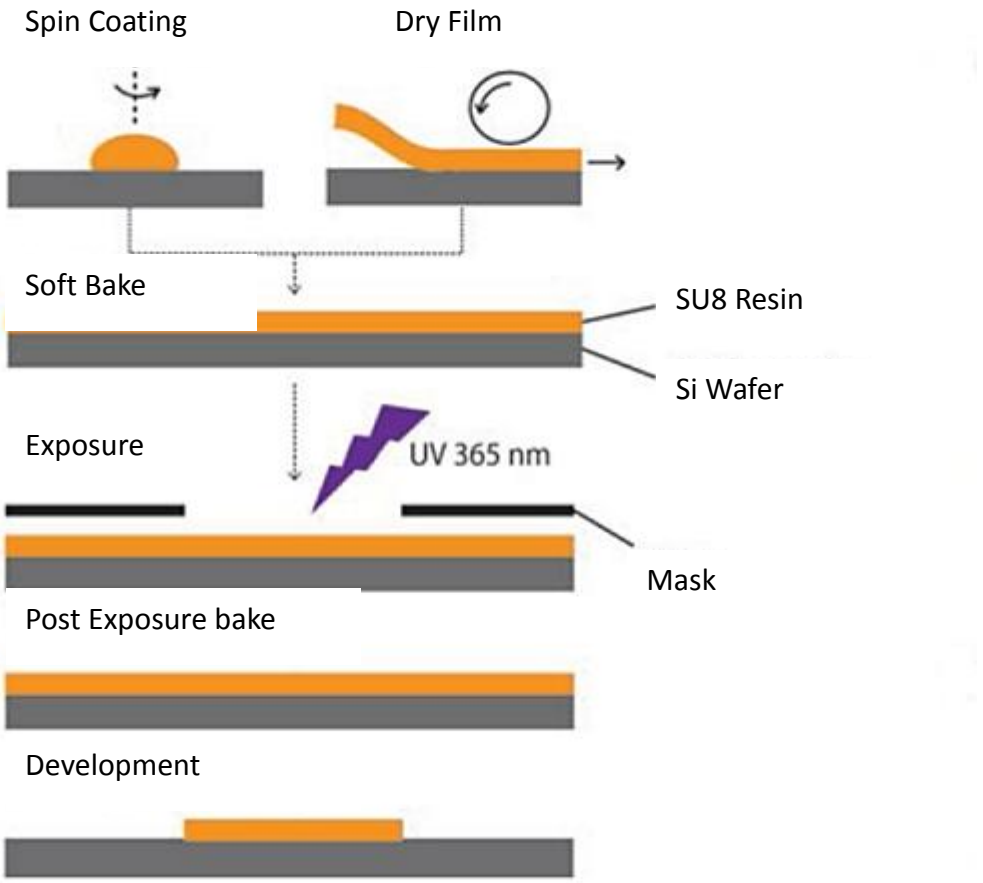

Figure 1-12 Schematic showing the several steps involved in Photolithography (Image reproduced from: Thesis: Anne-Laure Vayssade,'Flows of Herschel-Bulkley fluids in confined environments. Applications to the cementing of oil wells.').

III. Soft Lithography

Poly (dimethylsiloxane) (PDMS) is the most widely used elastomer for fabrication of elastomeric stamp. It has several advantages such as optically transparency (good for optical imaging), its stiffness which can be controlled, inertness, permeability to gases, non-toxic nature and fabrication (Psaltis & Fainman, 2006), ease of moulding, ease of bonding to itself (Mata, Fleischman, & Roy, 2005). The stamp is made by the method of cast molding (Duffy, McDonald, Schueller, & Whitesides, 1998; Xia & Whitesides, 1998). We used PDMS elastomer (Sylgard^{TM} 184 by Dow Corning). It is usually supplied in two parts: a PDMS elastomer and curing agent are mixed well in the ratio 10:1 and degassed to remove air bubbles. This mixture is poured over the Si

master mould having the features on the surface and left to cure in a convection oven at 65°C. Once cured, the mixture becomes a cross linked solid which can be easily peeled off from the Si master mould.

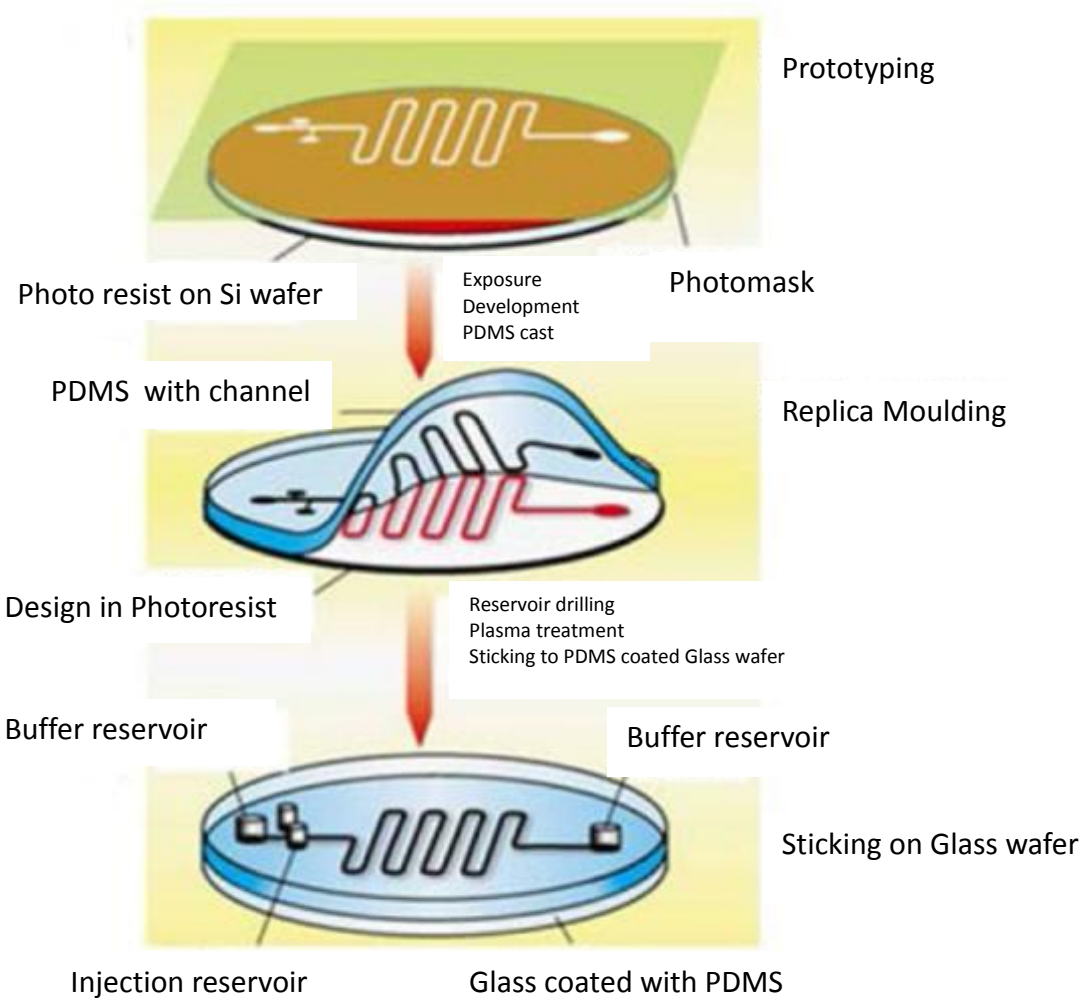

Figure 1-13 Schematic showing the various steps involved in soft Lithogtaphy using PDMS elastomer (Image reproduced from: Thesis: Anne- Laure Vayssade,'Flows of Herschel-Bulkley fluids in confined environments. Applications to the cementing of oil wells.').

IV. Surface Modification techniques

Although PDMS has many advantages, its inherent hydrophobic nature and its fast recovery after surface modification (usually hydrophilization) has impacted its use as a material of choice for microfluidic devices. A lot of research has been done to develop methods for achieving long lasting surface hydrophilization.

The most widely used dry phase method to change the surface wettability is using a plasma surface treatment (O_2, Air etc.) among others like UV/Ozone, chemical silanization, LbL etc (Hillborg et al., 2000; Hillborg & Gedde, 1998). Plasma renders a high surface energy layer to the surface. Oxygen plasma introduces polar functional group on the surface of PDMS making it hydrophilic. However, it is found that PDMS undergoes a hydrophobic recovery minutes after plasma treatment (Bhattacharya, Datta, Berg, & Gangopadhyay, 2005; Morra et al., 1990). This hydrophobic recovery is due to the reorientation of the functional groups and diffusion/migration of the PDMS chains from the bulk of the sample to surface (Makamba, Kim, Lim, Park, & Hahn, 2003).

For completely hydrophobic channels, we employed the thermal bonding technique. In this technique, PDMS elastomer is mixed with the curing agent at different concentration for the two different surfaces to be stuck. In one case, we use the ratio 1:5 (Curing agent: Elastomer) ratio and for the other surface we use 1:12 (Curing agent: Elastomer). Both the mixtures are degassed to remove the air bubbles. After degassing, one of the mixtures is spin coated on the glass plate and is partially cured by keeping inside the oven at 65°C for only 20 mins. The other mixture is poured over the Si mould and cured for 1 hr. After curing, both the surfaces are stuck together and kept on the hot plate at 80° C for 1 hr. Care must be taken to avoid excessively pressing the channels as this can lead to the partially cured PDMS entering the channel moulds.

We introduce a new technique to preserve the hydrophilicity of O_2 plasma treated PDMS. This technique involves the application of a surface modifying agent provided by Solvay. Here, the cured PDMS substrates and moulds (with the channels) are first treated with O_2/ Air plasma for 60s and are kept in the convection Oven at 65°C for 15mins. Surface modifying agent (10 times

diluted) is injected to the channels once they are at the room temperature. After 15 minutes, water is flushed through the channels to remove surface modifying agent. The hydrophilic microchannels are then used for experiments.

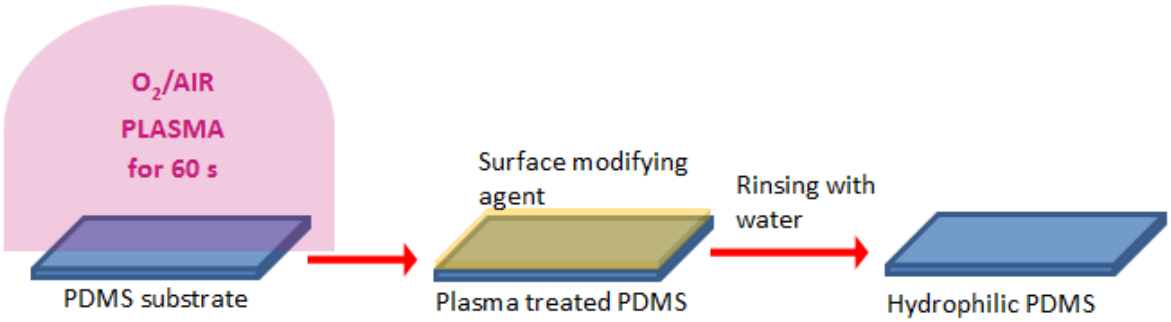

Figure 1-14 Schematic of the chemical modification technique used to preserve the hydrophilicity of plasma treated substrates.

V. Contact Angle Measurements

Contact angle is actually the quantitative measure of the wetting of the surface by a liquid. The Young's equation given below defines the contact angle as the angle which is formed between the three phase interfaces of solid-liquid-gas, by the liquid.

$$\gamma_{sg} = \gamma_{sl} + \gamma_{lg} cos\theta_c$$

where, γ_{sg}, γ_{sl} and γ_{lg} are the interfacial tensions between solid-gas, solid-liquid and liquid-gas respectively. θ_c is the wetting contact angle.

Low contact angle indicates that the liquid spreads well on the surface and wets the surface while a higher value of the contact angles signifies poor spreading. We measured the Water Contact angle in air (WCA) on different substrates namely, Untreated PDMS, Plasma treated PDMS, surface modifying agent treated PDMS and PEG treated PDMS using tensiometer (BIOLIN Scientific). De-ionised water (DI) was used for contact angle (CA) measurements. Static CA measurements are used to measure the wetting properties of the substrates. A droplet of DI

water of known volume (usually between 2-3µl) is carefully injected on the substrates and the image of the droplet is captured from which the CA is obtained. This setting time of capturing of the image should be small to ensure that no evaporation takes place and large enough to give the droplet time to deposit and react with the substrate.

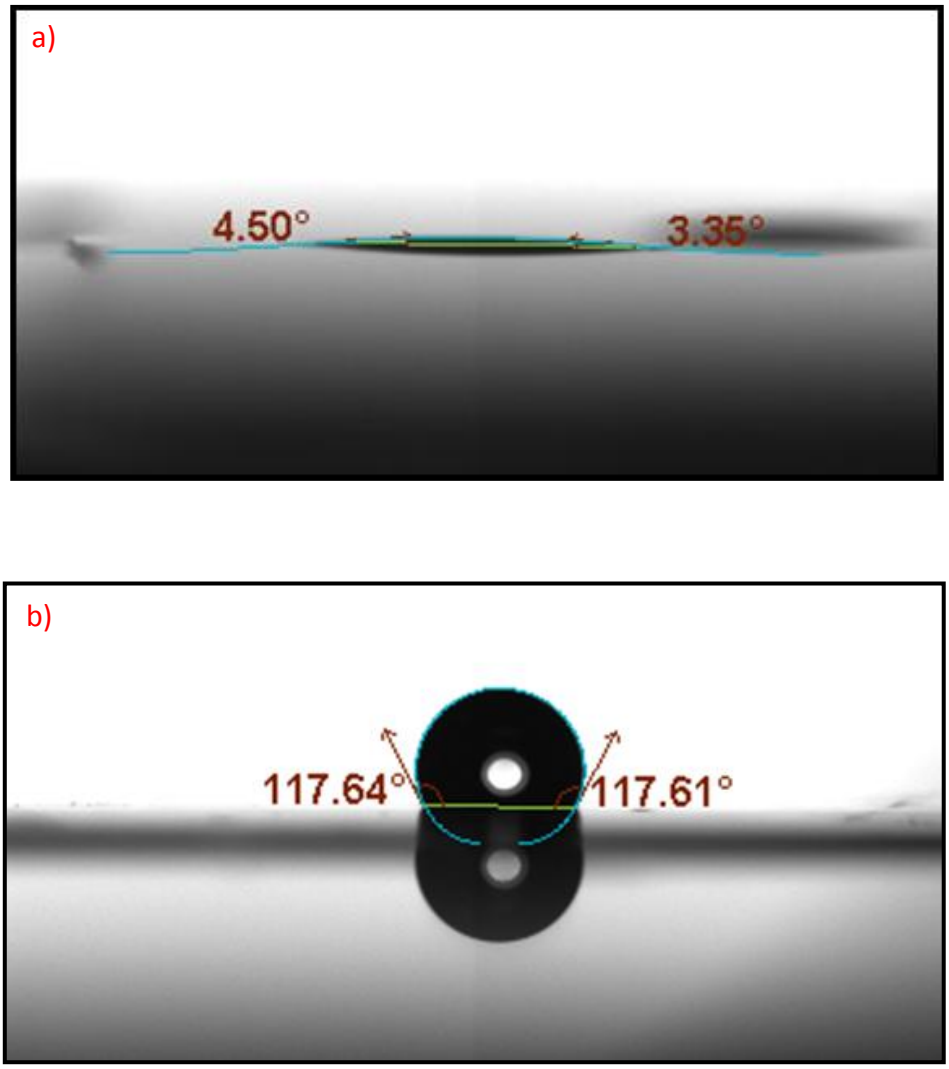

Figure 1-15 Contact angle measurements of few µl water droplet on two different substrates, (a). Surface modifying agent (by SOLVAY) treated PDMS surface, (b). Cured, untreated PDMS surface.

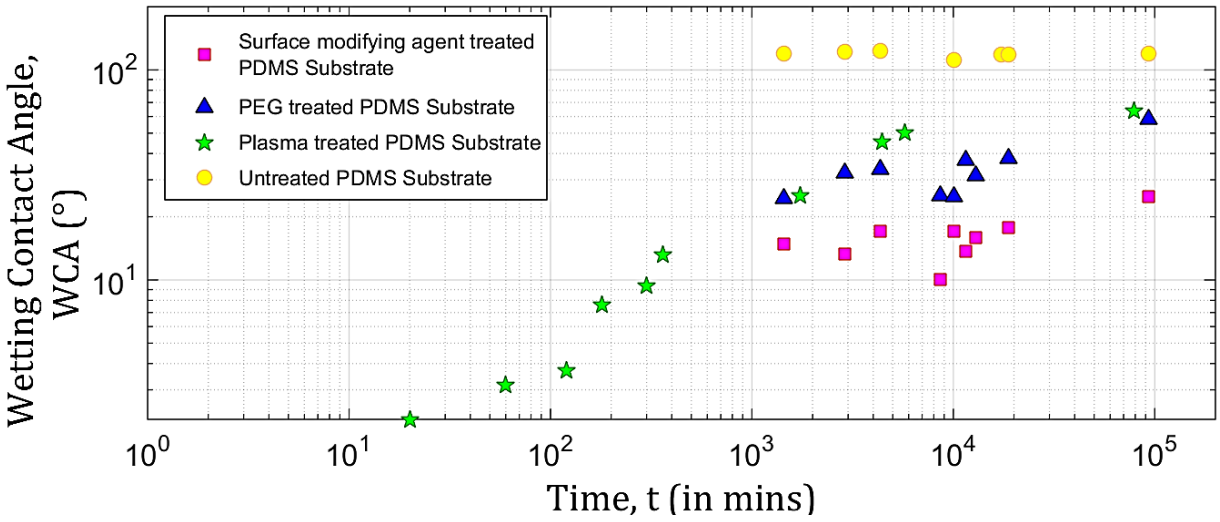

Figure 1-16 A plot of Wetting contact angle as function of time for four different PDMS surfaces namely untreated cured PDMS, surface modifying agent (by SOLVAY) treated PDMS surface, PEG treated PDMS surface and Plasma treated PDMS surface.

Figure 1-16 displays the temporal evolution of the wetting contact angles measured by the tensiometer for different substrates. It can be clearly seen that untreated PDMS is very hydrophobic with a wetting contact angle of around 120° while the plasma treated PDMS substrates lose their hydrophilic behaviour in few hours and the contact angle keeps increasing. However, for surface modifying agent treated PDMS substrate, it was difficult to measure the contact angle initially as the substrate was too hydrophilic. After 24 hr, it slowly increased to a value 15°. Again, the wetting contact angle of surface modifying agent treated PDMS agent increased but rather slowly i.e. 24° at 1552 hrs as opposed to plasma treated substrate which attains a wetting contact angle of 64° at 1320 hrs. Thus, surface modifying agent by SOLVAY works effectively to maintain the hydrophilicity of the highly hydrophobic PDMS substrates.

1.3.7 Pressure Measurements

I. Differential Pressure

Pressure measurements in the microchannels were done using a home-made setup with Arduino Uno and MATLAB Data acquisition tool. The pressure drop is measured using a commercial

pressure sensor, 1 bar and 7 bar both digital (ASDX series, Honeywell) connected to an Arduino data acquisition card to measure the pressure. MATLAB data acquisition tool is used to handle all the operations, it helps the acquisition card to communicate with the computer. The card reads the voltage of the pressure sensor which is converted to pressure data through the computer.

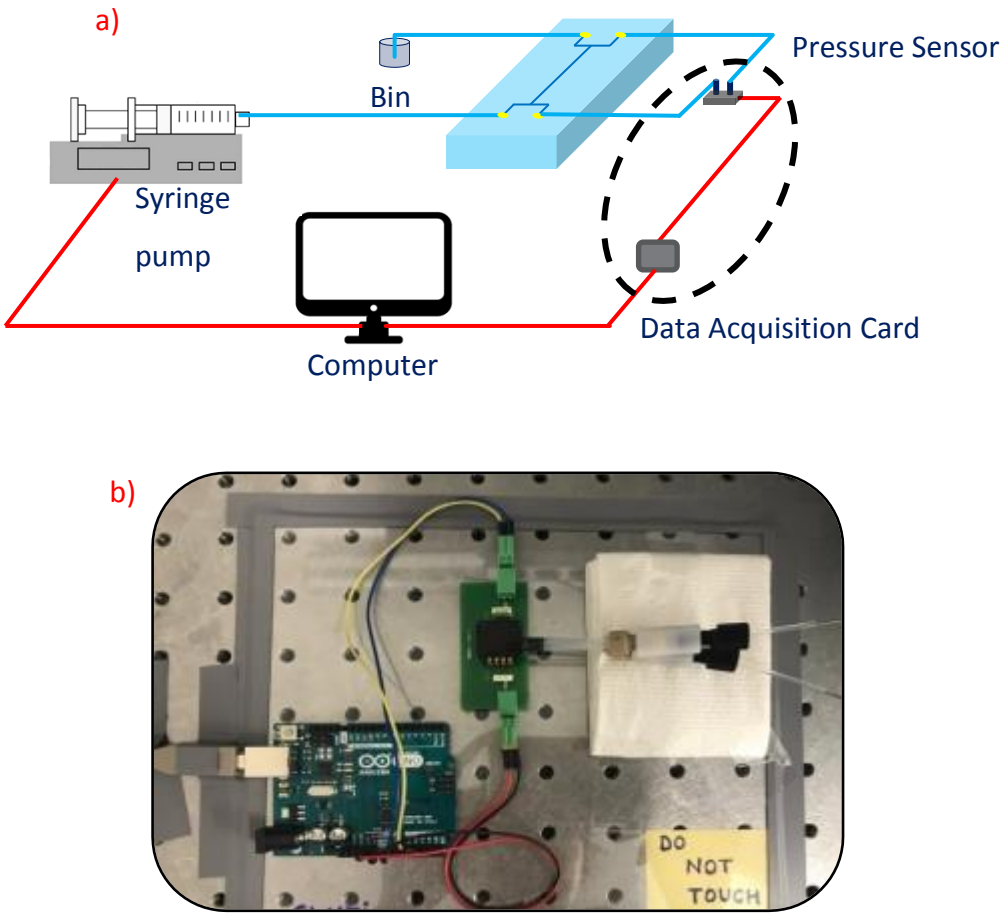

Figure 1-17 (a) shows the schematic of the pressure measurement set-up used, (b) photograph of the actual setup used.

1.4 Thesis Structure

This thesis is comprised of 5 chapters which are presented in the following order:

Chapter 1 introduces an explanation to the main problem of jamming in porous media by dilute microgel suspensions. The significance and its potential applications in industrial processes are discussed. An explanation of the different techniques used for size characterization, rheological characterization, imaging, microfluidic fabrication, pressure measurements are also discussed.

Chapter 2 reviews the different techniques used to have a control over the particle size of the microgel suspensions and discusses a method to achieve higher concentration without changing the inherent properties of the suspension. An investigation on the rheological behaviour of the suspension as a function of concentration is done and the effective particle volume fraction is estimated.

Chapter 3 explains a simple experimental setup to study the drying dynamics of the microgel suspensions in a confined geometry. The effect of the confinement on the drying is explained.

Chapter 4 presents the results of filtration experiments in porous media for frontal filtration and demonstrates how the jamming is affected by parameters like particle size, pore size, flowrates and pressure gradients. A demonstration of fluid loss control through a porous media-lateral filtration is shown. Results from a flow experiment in a simple linear channel are also presented to check the effect of high shear on the suspensions.

Chapter 5 presents an appropriate experimental set up and methodology to estimate the permeability of the filter cake of the microgel suspension. A method to form the filter cake on a supporting membrane filter is explained. Futhermore, a method to calculate the permeability of the filter cake formed for the flow of water is explained using Darcy's law. A rheological investigation on the filter cake was made to get the rheological parameters like yield stress, shear viscosity and the constitutive laws that best suit the filter cake.

Chapter 2

Particle Size & Rheological Characterization of Microgel Suspensions

Table of Contents

Chapter 2 Particle Size & Rheological Characterization of Microgel Suspensions

2.1 Research Objectives

In this chapter, we address two major properties of the microgel suspensions. First, the particle size, where we discuss how ultra-turraxing and centrifugation helps control the size and polydispersity of the inhomogeneous microgel (Microgel-IN). Later in this chapter, we examine the rheological properties as a function of Microgel concentration (% wt.). We show that the power law model and the Herschel-Bulkley model best describe the microgel suspensions. We obtain parameters like the yield stress, power law index (n) and consistency factor (k) using curve fitting on the experimental shear stress versus shear rate data. We use the analytical model by Krieger-Dougherty to describe the relative viscosity as a function of particle volume fraction and predict the maximum volume fraction, φ_m, which we will later see (in chapter 4) as an important parameter to understand the jamming mechanism.

2.2 Particle Size Measurement of Microgel Suspensions

Characterization of the size of the particles in suspensions is important to understand the physical properties of the suspensions. Particle aggregates size in suspensions are known to change during the aggregation process, during dispersion, fragmentation among others. It is one of the most fundamental parameters in characterizing suspensions be it colloidal or microgel. The term particle size describes a variety of measurable quantities which are linked to the outer dimensions of the particles. The property measured by the instruments is usually the diameter of the sphere whose volume is equivalent to the volume of the particle. This property is represented in terms of either a frequency distribution curve or a cumulative distribution curve. There are several ways to present the size distribution curves such as number-weighted distribution, volume-weighted distributions and intensity-weighted distributions which give statistical parameters like Mean (Average size of the population), Median (size where 50% of the population is below or above) and Mode (size with highest frequency) (see Figure 2-1).

The weighted means can be represented in terms of the weighting of each individual particles. The classification of the weighting means is based on the measuring principle used. The most commonly used weighted distributions are as follows:

- Number-weighted distributions : Counting techniques like image analysis gives the number weighted distribution. Here, particle contribution is given in terms of the number of the particles rather than the size of the particle. This means all the particles are given equal weightage.
- Volume-weighted distributions : Here the contribution of each particle in the distribution is related to the volume of that particle. The relative contribution is proportional to $(size)^3$. Static light scattering techniques like laser diffraction is one example which gives volume-weighted distribution.
- Intensity-weighted distributions : Here, the contribution of each particle in the distribution is proportional to the intensity scattered by it. According to the Rayleigh approximation, the relative contribution is proportional to $(size)^6$.

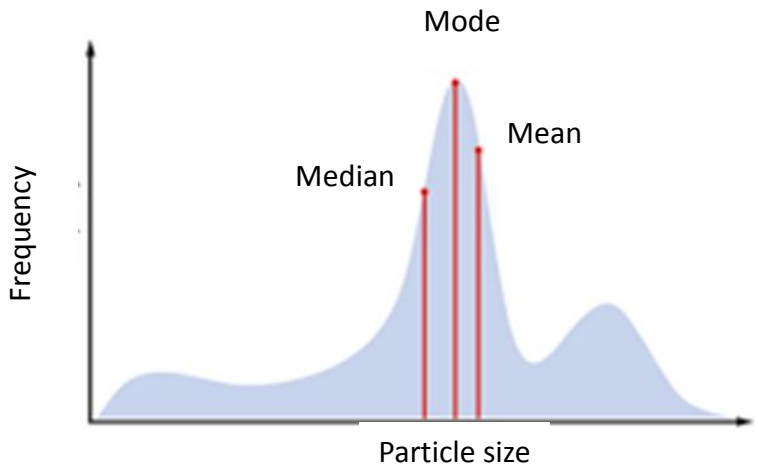

Figure 2-1 Illustration of the mean, median and mode of the particle size distribution. (Reproduced from: A basic guide to particle characterization, Whitepaper, Malvern Instruments Ltd, https://www.cif.iastate.edu/sites/default/files/uploads/Other_Inst/Particle%20Size/Particle%20Characterization%20Guide.pdf)

Particle size data of the same sample measured by different techniques will often produce different results. However, it is possible to convert particle size data from one technique to another assuming some parameters regarding the form of the particle and its physical properties. Among the major statistical parameters used, mean is the most important one and is actually a

calculated value similar to average. The three most commonly used statistical parameters in terms of mean size of particles are given below:

- Number weighted mean $d_{1,0}$: Commonly known as the arithmetic mean and is mostly common to applications where the number of particles are of interest like particle counting applications.
- Surface weighted mean $d_{3,2}$: Commonly known as Sauter mean diameter. It is relevant to applications where surface area is importnat e.g reactivity, dissolution. It is very sensitive to the presence of fine particles in the sample
- Volume weighted mean $d_{4,3}$: Also known as the De Brouckere mean diameter. It reflects the size of the particles that makes the bulk of the sample volume.

The other most widely used values to describe the particle size are the d-values. $d_{0.1}$, $d_{0.9}$ and $d_{0.5}$ represent the range of the particle sizes and mid-point in the given sample. $d_{0.5}$ is the diameter at which 50% of the population lie below it. Similarly, 90% of the population lies below the value $d_{0.9}$ and 10% below the value at $d_{0.1}$.

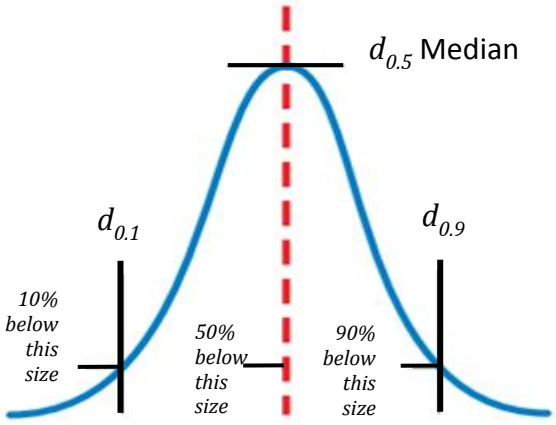

Figure 2-2 Illustration of the mean, median and mode of the particle size distribution (Reproduced from: https://www.horiba.com/fileadmin/uploads/Scientific/eMag/PSA/Guidebook/pdf/PSA_Guidebook.pdf).

The width of the distribution is given by '$Span$' which is given as

$$Span = \frac{d_{0.9} - d_{0.1}}{d_{0.5}}$$

Many techniques have been proposed by scientists to determine the size of particles. These techniques can be broadly classified into two categories, (1). Intrusive, and (2). Non-Intrusive. In intrusive techniques, probes are used to get the particle size data from a flowing sample of solid or liquid particles. Most commonly known intrusive techniques include sieving or sedimentation analysis. On the other hand, non-intrusive techniques are often optical techniques that helps in determining the particles properties like size, shape. The advantage of the non-intrusive technique is that it does not interfere with the particle suspension. These techniques are also capable of measuring the size in different solvents. These include light scattering (Laser diffraction and Photon correlation spectroscopy) and image analysis. The choice of the technique to be used largely depends on the parameters required, particles size range, resolution needed etc. In this chapter, we have used laser diffraction to analyse the size of the particles and volume weighted distributions as they are thought to be more relevant for accounting for the impact of the various particle sizes to the suspension rheology.

2.3 Rheology of Microgel Suspensions

Rheology is the study of deformation of matter under the application of force. This deformation often refers to how two layers of the material move against each other during the application of stress. The word 'rheo' come from greek and it means 'to flow'. Solids deform when a force is applied and liquids and gases flow under the application of the force. The beginning of the study of rheology can be traced back to the 17th century with the works of Newton and Hooke on viscous and elastic materials respectively. Robert Hooke in 1678, came up with the ''True theory of elasticity'' in which he proposed that the extension in any spring is proportional to the tension applied. Sir Isaac Newton developed a similar theory in case of liquids and the work was published in ''Principia" (Newton, 1687). He suggested that on application of a steady shear for the case of

liquid, there arise a resistance which is due to the layers of the liquid moving relative to one another (see Figure 2-2).

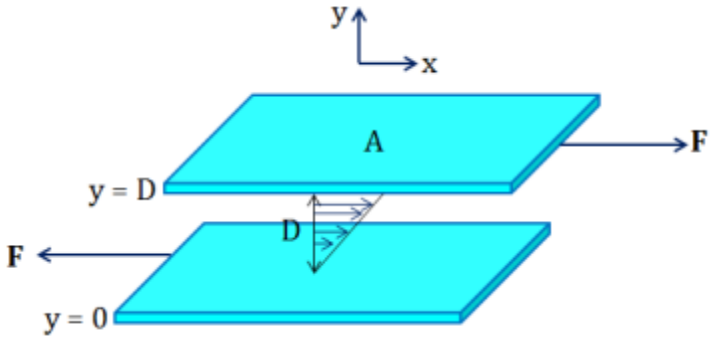

Figure 2-3 Schematic of two parallel planes. Each of area, A and at a distance of D from each other. The space between the planes is filled with a liquid which is sheared with a tangential force, F. The layers of liquid move relative to each other with velocity gradient.

The resultant a shear rate is also called the deformation velocity which is given as

$$\frac{dv}{dy} = \frac{d}{dy}\left(\frac{dx}{dy}\right) = \frac{d\gamma}{dt} = \dot{\gamma}$$

$$\uparrow \qquad\qquad\qquad \uparrow$$

$$velocity\ gradient \qquad shear\ rate$$

Deformation: $$\gamma = \frac{dx}{dy} = \tan\alpha \qquad [-]$$

Deformation velocity: $$\dot{\gamma} = \frac{d\gamma}{dt} \qquad [1/s]$$

When a force F is applied to the plate of area A in a rheology experiment (see Figure 2-2) , the resulting shear stress is obtained which is dependant on the shear rate and the shear viscosity, η. This shear viscosity (η) is the resistance to flow.

Shear stress: $$\sigma = \frac{F}{A} = \eta\dot{\gamma} \qquad [Pa]$$

Shear viscosity: $\eta = \frac{\sigma}{\dot{\gamma}}$ $[Pa\ s]$

Based on the dependence of shear viscosity on the shear rate, the fluids are generally classified into three categories.

Newtonian fluids

If the shear viscosity is independent of the the shear rate

Shear thinning fluids

If the shear viscosity decreases with increasing shear rate

Shear thickening fluids

If the shear viscosity increases with increasing shear rate

Microgel suspensions often belong to the class of non-Newtonian fluids i.e. their viscosity may depend on the shear rate or the shear rate history. This different response of the non-Newtonian fluids on the application of stress arises as a result of deformation and rearrangement of the macroscopic elements constituting the fluid. Microgel suspension rheology is not as well studied as compared to the suspensions of hard spherical particles (Mewis & Wagner, 2009). The complexity in the rheology of microgel suspensions (soft particle) arises due to changes in the volume, deformation of the particles and porosity owing to physiochemical changes and mechanical forces. It has been shown that it is relatively easy to define volume fractions of hard spherical particles with error as small as 3% (Poon, Weeks, & Royall, 2012). However, it is this complexity which has attracted great interest in understanding the rheology of soft particles. One interesting property of microgels is their responsiveness to the external environment. And therefore, it is relatively easy to change the rheology of microgel suspensions as required by altering parameters like solvent quality, size of the particle, density of cross linking and surface properties etc. Their effective volume fraction can also be easily altered by changing the temperature, pH, addition of ions to the solvent (Cloitre, 2011; Cloitre, Borrega, Monti, & Leibler,

2003). At lower concentrations, particles of the suspensions stay dispersed in the solvent and show Brownian motion (depending on the size). Above a critical concentration, microgel suspensions behave like a soft glass (glassy regime) at high volume fractions as the particles are in close contact with each other and their movement is hindered sterically ; they exhibit amorphous structure. At the jamming concentration, microgel suspensions exhibit a very high packing fraction (similar to hard spheres) or even more since the particles are deformable (Stokes & Frith, 2008).

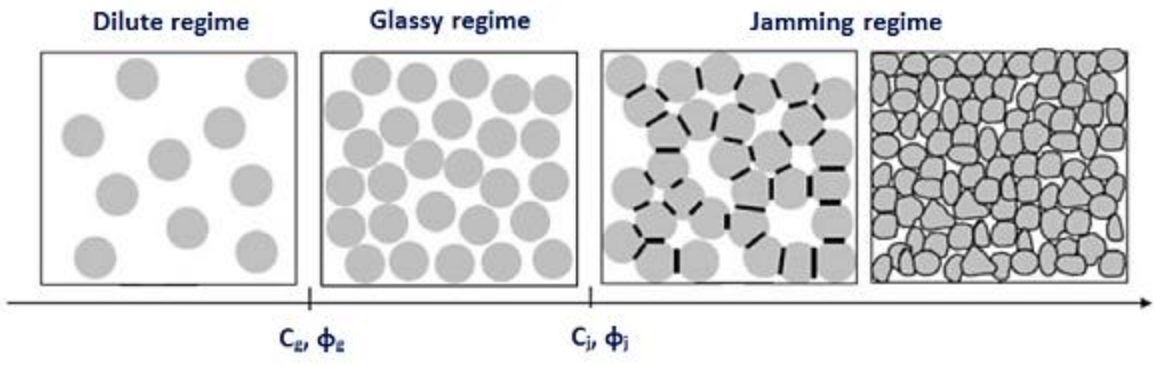

Figure 2-4 Pictorial sketch of the three different regimes namely a). Dilute regime, b). Glassy regime, c). Jamming regime the microgel undergoes as the concentration c increases. (Reproduction: Fabrice Monti. Microrhéologie de suspensions colloïdales non ergodiques)

Microgel suspensions at high solid content show high shear viscosities and shear thinning behaviour both in soft glassy and jamming regimes. We now will briefly describe the important non-Newtonian rheological properties.

2.3.1 Flow Behaviour

Microgel suspensions belong to a category of non-Newtonian fluids where the viscosity decreases as the shear rate applied is increased, giving rise to what is popularly known as shear thinning behavior/pseudoplasticity (Barnes, Hutton, & Walters, 1989). A good understanding of the rheology of microgel suspensions is usefull in exploiting their applications such as oil and gas processes (Rousseau et al., 2005), in consumer personal care products where microgel like Carbopol are used to make the product viscous and helps in improving the texture (Ketz, Prud'homme, & Graessley, 1988), bio encapsulations, inks, biomaterials, lubricants, controlled

drug delivery (like topical drug delivery systems like nasal, dermal applications) where it is important to understand the rheology as it helps in optimizing the spreadibility and the adhesion on application (Duchěne, Touchard, & Peppas, 1988; Jean, Emanuel, Nicolas, & Jérôme, 2004; Tamburic & Craig, 1995). Microgel suspensions as explained before can be tailor made as per the desired applications by varying polymer concentration, pH, crosslinking density, size of the particles, surface charge, and the type of solvent. Depending on the solvent properties, microgel particles can be made to swell or deswell (Borrega, Cloitre, Betremieux, Ernst, & Leibler, 1999; Senff & Richtering, 1999). Several models have been proposed to describe this flow behaviour, for example, the Bingham model, the power law model and power law with yield stress (Herschel-Bulkley model). In context to the work presented in this thesis we will only require the power law and Herschel-Bulkley models, the description of which are briefly given below:

I. Oswald/Power law

The power law model has been the most widely used model to describe the behaviour of non-Newtonian fluids (Barnes et al., 1989). The most general form for steady simple shear is given as

$$\sigma = k\,\dot{\gamma}^{n} \qquad \text{or} \qquad \eta = k\,\dot{\gamma}^{n-1}$$

where, η is the shear viscosity (Pa s), $\dot{\gamma}$ is the shear rate (s^{-1}) and σ is the shear stress (Pa), k is the consistency index (Pa s^n) and n is the power law index (unitless). k gives the value of the apparent viscosity of the fluid at 1 s^{-1}. One well known disadvantage of the power law model is that it cannot be used to describe the fluid behaviour in the low shear regime. As n<1, η tends to infinity which is not the case practically. Most fluids exhibit a Newtonian viscosity at low shear rates.

II. Herschel- Bulkley Model

Another generalized model used to describe non-Newtonian fluids. It was first introduced by Winslow Herchel and Ronald Bulkley (Bulkley, 1926). The constitutive equation is given as

$$\sigma = \sigma_y + k\,\dot{\gamma}^n$$

Here, σ is the shear stress, k is consistency index and n is the power law index, $\dot{\gamma}$ is the shear rate and σ_y is the yield stress. According to Pevere et al., this model is considered precise due to three parameters which can be adjusted and gives a lot of information about the fluid (Seyssiecq, Ferrasse, & Roche, 2003) .

$\sigma_y = 0$ and $n > 1$ means **dilatant behaviour**

$\sigma_y = 0$ and $n < 1$ means **pseudoplastic behaviour**

$\sigma_y > 0$ and $n = 1$ means **Bingham plastic behaviour**

$\sigma_y = 0$ and $n = 1$ means **Newtonian behaviour**

2.3.2 Particle Volume Fraction

Most of the major work done on the rheology of suspensions has been performed for the hard-sphere particle suspensions, which are defined as non-deformable and non-interacting particles (van der Werff & de Kruif, 1989). These investigations on hard-sphere particles include both experiments and simulations and therefore there is a very good understanding of their flow behaviour (Mewis & Wagner, 2009). As a result, various accurate models have been proposed for hard-sphere particle suspensions that predict suspension viscosity as a function of particle volume fraction. On the other hand, the rheological properties of soft particles are less well understood. The pivotal parameters that control the rheology of soft particle suspensions are: particle size, particle volume fraction, particle surface charge and the internal structure e.g cross- linking density.

The rheology of the suspension is found to be strongly dependent on the particle volume fraction of the particles and the viscosity of the continuous phase. The difficulty in predicting the microgel viscosity arises due to the volume of these soft particles that changes as the fluids from the

particle moves (swelling and de-swelling) as a result of changes in the pH, temperature, solvent etc (Senff & Richtering, 1999; Tan, Pelton, & Tam, 2010; Tan, Tam, Lam, & Tan, 2005). A very common approach for dealing with this difficulty is to define the effective volume fraction as proportional to concentration, c i.e.

$$\phi = k_0 c$$

It is seen that the concentration of particles has a direct effect on the suspension viscosity which can be helpful in understanding the non-Newtonian behaviour of the microgel suspensions. Particles flowing in a solvent tend to disturb the flow of the fluid leading to dissipation of energy. Several phenomenological models have been proposed that predict the viscosity of the microgel suspension as function of normalized particle volume fraction. Some of them are briefly explained below:

I. Einstein Equation
II. Mooney's Equation
III. Batchelor's Equation
IV. Krieger Dougherty's Equation

The experimental data can be modelled using the above equations to get a clear understanding of the viscosity as a function of concentration. Of course, these models have to be used for a certain range of concentrations.

I. Einstein's Equation

Albert Einstein, in 1906, in his Ph.D. thesis, worked on the molecular kinetic theory of liquids. In this classical model, he considered the assumption that particles are hard spheres, non-interacting and infinitely diluted. He showed how the size of the particles in the dilute suspension can be evaluated from viscosity of the solution and the solvent (Einstein, 1906). It was shown that the spheres suspended in the fluid actually effect the motion of the fluid. Einstein came up with the following equation:

$$\eta_r = 1 + \xi\phi$$

where $\eta_r = \frac{\eta_o}{\eta_s}$ is the relative viscosity, η_o is the viscosity of the suspension and η_s is the viscosity of the pure solvent, ϕ is the volume fraction of the spheres, and ξ is the free parameter or Einstein's coefficient or the 'intrinsic viscosity' that needs to be determined. Coefficient ξ takes the value of 2.5 for a system consisting of small hard spherical particles. Several extensive experimental efforts have been made to validate ξ. It was shown that the favorable value should lie in the range $1.5 < \xi < 2.5$ (Happel, 1957; Jeffrey & Acrivos, 1976; Pabst, Gregorová, & Berthold, 2006). This classical equation by Einstein simply implies that single particles can increase the viscosity of the suspension linearly as a function of the volume fraction. This value of $\xi = 2.5$ is universally accepted for concentrations, $\phi < 0.05$ assuring that the flow of one particle does not affect the flow field of other particles.

II. Batchelor's Equation

As the particle concentration increases, the interaction between the particles becomes crucial and the system becomes difficult to analyse (Batchelor, 2006). Batchelor's equation takes into account the effects of the two particle hydrodynamic interaction on the suspensions viscosity added as a second order term to Einstein's Equation.

$$\eta_r = 1 + 2.5\,\phi + \mathrm{C}\,\phi^2$$

The value of the constant, C can have value ranging from 4.2 to 6.2. The value is derived to be C= 6.2 when considering the case of Brownian spheres by Batchelor. The same constant C is derived to be as C=5.2 for non-colloidal systems (Ball & Richmond, 1980). This equation is valid for volume fractions $\phi < 0.15$.

III. Mooney's Equation

Mooney in his work in 1951 extended Einstein's equation for only infinitely dilute suspensions to suspensions of higher concentrations. It was seen that in suspensions of higher concentrations,

the relative viscosity follows an exponential variation with concentration. Mooney derived the following equation taking into account the particle size variations and the particle interactions (Mooney, 1951).

$$\eta_r = \exp\left[\frac{\xi\phi}{1-\varepsilon\phi}\right]$$

where, η_r is the relative viscosity, ϕ is the volume fraction of the particles, ξ is chosen to be 2.5 same as for Einstein's equation and ε is the self-crowding factor. As one can see, the viscosity goes to infinity when it reaches the maximum concentration. At maximum concentration, the suspension becomes more solid-like and there is absolutely no movement of the neighboring particles. For the determination of the self-crowding factor, ε, Mooney considered a two-component system with two different size particle, a_1 and a_2. The partial volume concentration of particles of size a_1 is ϕ_1 hence, for a_2, the particle will suspend in the remaining available volume, $1 - \alpha_{12}\,\phi_1$. Based on the packing densities, it was observed that ε assumes a minimum value for least dense packing which is $\varepsilon \sim 1.35$ and a maximum value of ~ 1.91. The value of ε was not affected by any change in temperature. The range of the self-crowding factor, ε, as determined by Mooney is

$$1.35 < \varepsilon < 1.91$$

and

$$0.52 < \phi_m < 0.74$$

IV. Krieger- Dougherty's Equation

For higher concentration close to maximum packing fraction, it is imperative to use other phenomenological models to describe the concentration dependence of the viscosities to account for experimental results. In a paper published in 1959, Krieger and Dougherty proposed a semi-empirical equation that showed how the particles interact with the neighbouring particles (Krieger & Dougherty, 1959). Krieger- Dougherty Equation is written as:

$$\eta_r = \frac{\eta_o}{\eta_s} = \left(1 - \frac{\phi}{\phi_m}\right)^{-[\eta]\phi_m}$$

where parameters η_o, η_s, ϕ and $[\eta]$are the viscosity of the suspension at zero shear rate, viscosity of the solvent, volume fraction and intrinsic viscosity of the particles respectively. ϕ_m is the maximum packing fraction i .e. the volume fraction at which the viscosity diverges and is often taken as 0.64 for monodisperse hard-spheres. Krieger-Dougherty equation reduces to Einstein's equation at low concentration. Krieger Dougherty equation is the most used model for fitting the experimental data.

2.3.3 Linear Viscoelasticity

The word 'viscoelasticity' means the existence of elastic and viscous properties simultaneously in a material even though elastic and viscous are two extreme material properties in themselves. In the case of a purely (linear) elastic solid, when a deformation of γ is applied, the stress response σ is proportional to the deformation i.e.

$$\sigma = G\gamma$$

where G is the elastic modulus of the material.

When the low deformation γ is removed, the material returns back to its original configuration and the stress is released. For purely (linear) viscous fluids, the application of a small shear rate, $\dot{\gamma}$, leads to a stress response σ which is proportional to the rate of deformation i.e.

$$\sigma = \eta\,\dot{\gamma}$$

where η the viscosity of the fluid. Purely viscous fluids undergo an irreversible change in their configuration. Viscoelastic materials show an intermediate behaviour between elastic solids and viscous fluids when submitted to deformation. This response is typically common to many polymeric materials. In the case of solid-like viscoelastic material, the material returns back to its

original state when the deformation is removed and is not permanently damaged. These materials show time dependence which means that the transition from elastic behaviour to viscous can be observed over a course of time, τ commonly known as the relaxation time.

$$\tau = \frac{\eta}{G}$$

The linear viscoelasticity is measured with the help of oscillatory experiments where the sample is subjected to a periodic deformation $\gamma(t)$ which results in a periodic stress responce $\sigma(t)$.

$$\underset{Preset\ Deformation}{\gamma = \gamma_0 \cos(\omega t)} \xrightarrow{Results\ in} \underset{Response\ of\ the\ system}{\sigma = \sigma_0 \cos(\omega t + \delta)}$$

ω is the frequency of oscillation , σ_0 is the stress amplitude, γ_0 is the deformation amplitude and δ is the phase displacement relative to the preset deformation. Depending on the displacement of the phase δ, the material behaviour can be classified as

$$\boldsymbol{Elastic\ behaviour}\ for\ \delta = 0$$
$$\boldsymbol{Viscous\ behaviour}\ for\ \delta = \frac{\pi}{2}$$
$$\boldsymbol{Viscoelastic\ behaviour}\ for\ 0 < \delta < \frac{\pi}{2}$$

Viscoelastic behaviour is better described by the use of the complex modulus, G^* which can be written in terms of the complex shear strain deformation, γ^* and the complex shear stress, σ^*. The complex part is introduced to get rid of the trigonometric identities and to simplify the rheological calculations.

complex shear strain deformation:

$$\gamma^* = \gamma_0 \left[\cos(\omega t) + i \cdot \sin(\omega t) \right] = \gamma_0 \cdot \exp(i\omega t)$$

complex shear stress:

$$\sigma^* = \sigma_0 [\cos(\omega t + \delta) + i \cdot \sin(\omega t + \delta)] = \sigma_0 \cdot \exp[i \cdot (\omega t + \delta)]$$

complex modulus:

$$G^* = \frac{\sigma^*}{\gamma^*} = \frac{\sigma_0}{\gamma_0} \exp(i \cdot \delta) = G' + i \cdot G''$$

here, G' is the storage modulus which represents the degree of elastic behaviour and G'' is the loss modulus which corresponds to viscous behaviour.

Storage/ Elastic Modulus:

$$G' = \frac{\sigma_0}{\gamma_0} \cdot \cos\delta \qquad [Pa]$$

Loss/ Viscous Modulus:

$$G'' = \frac{\sigma_0}{\gamma_0} \cdot \sin\delta \qquad [Pa]$$

The absolute value of the complex modulus is given as:

$$|G^*| = \sqrt{G'^2 + G''^2} = \frac{\sigma_0}{\gamma_0}$$

The ratio of G'' and G' gives the dissipation factor $\tan\delta$, which is an estimate of whether the elastic or viscous behaviour is dominating.

$$\tan\delta < 1 : \textit{Elastic behaviour dominates}$$
$$\tan\delta > 1 : \textit{Viscous behaviour dominates}$$

2.4 Experimental Procedure

The microgel suspension for different concentrations of each type i.e. Microgel-IN, Microgel2000-10 and Microgel4000-10 were observed optically using phase contrast microscopy (see section 1.3.5). The size distribution of the microgel suspensions was measured using a Malvern Mastersizer3000 (refer section 1.3.2). The rheological measurements were performed using a stress-controlled Malvern Ultra+ rotational rheometer. Three different geometries were used for different suspension concentrations. For the double gap and parallel plate geometries, a same test gap of 1 mm was used while for the cone and plate geometry, a default gap of 0.14 mm (corresponding to the cone truncature) was used. For higher concentrations, roughened surfaces were used to avoid any slippage. The sample temperature was kept of 25°C using a Peltier plate. Extreme care was taken to avoid any air bubbles while loading the sample in the geometry. All experiments were performed using a solvent trap to minimize evaporation of the solvent.

An oscillatory amplitude sweep at a constant frequency of 1 Hz and a varying strain signal was performed to determine the viscoelastic properties. Storage (G') and loss (G'') moduli were measured in the linear regime at 1% strain for all the concentrations. The flow behaviour was measured by applying increasing values of constant shear stress and then decreasing the stress. Figure 2-5a illustrates the rheological actions/steps used to measure the flow curve. The mean shear rates and viscosities in steady state for each stress value were determined (Figure 2-5b&c). To study the aging of the suspension, the same flow measurements were carried out on dilute suspensions at different times ranging from 1 – 17 days.

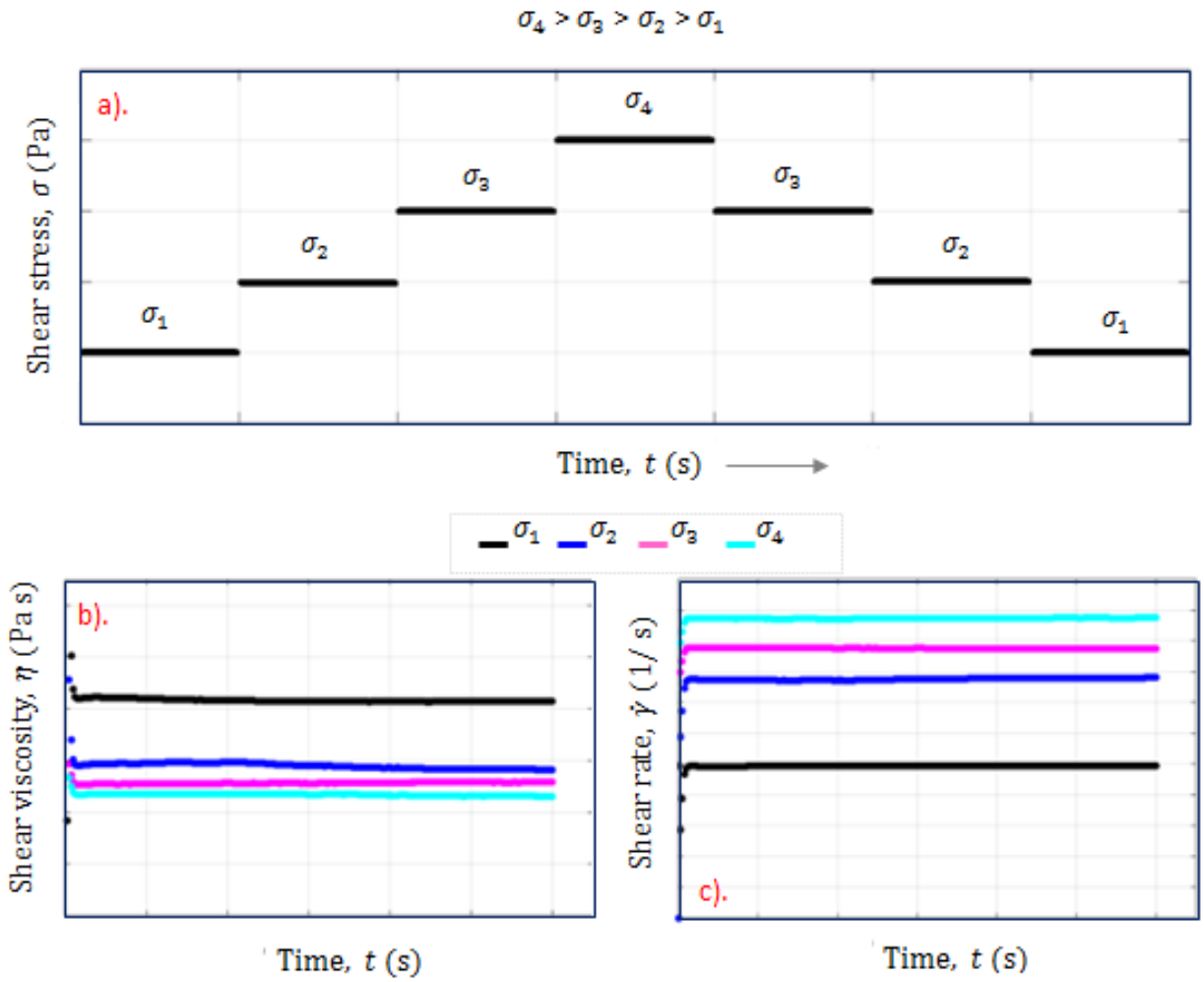

Figure 2-5 (a) Step shear stress experiments performed on the microgel suspension. The stress imposed is first increased and then decreased. The duration of each step varied from 240s to 6000s, (b,c) shows typical plots for shear viscosity and shear rates at different imposed shear stress as a function of time

The rheological data is analysed using rSpace software and the models such as power law and Herschel-Bulkley for the flow curves and Krieger Dougherty were fitted to the experimental data points using MATLAB curve fitting tool using the method of least squares fitting. For the estimation of the particle volume fraction, we fitted the low shear viscosity data (as the zero shear viscosity plateaus was inaccessible for the range of shear stresses used in this work) to Krieger Dougherty's equation.

The MATLAB curve fitting toolbox provides goodness-of-fit statistics that indicates the goodness of the model fit to the experimental data like the sum of squares due to error (SSE) and R-square (R^2).

Sum of squares due to error (SSE) actually is a measure of the deviation of the experimental data from the fit of the experimental data. It is sometimes also referred as the summed square of residuals. A value closer to 0 indicates that the fit will more accurately predict the data and that the data possess a smaller random error component.

$$SSE = \sum_{i=1}^{n} (y_i - \hat{y}_i)^2$$

where, y_i is the experimental value and $\hat{y}_i$ is the calculated valued for each data point and n denotes the number of observation.

R-Squared (R^2) also known as square of the multiple correlation coefficients and the coefficient of multiple determinations. It explains how successful the fit explains the variation of the experimental data. It is defined as the ratio of sum of squares of regression (SSR) to the total sum of squares (SST).

SSR is given as

$$SSR = \sum_{i=1}^{n} (\hat{y}_i - \overline{y})^2$$

Here, $\overline{y}$ is the mean of the observed data

$$\overline{y} = \frac{1}{n} \sum_{i=1}^{n} y_i$$

SST is given by:

$$SST = \sum_{i=1}^{n}(y_i - \overline{y})^2$$

$$STT= SSR+SSE$$

which gives R-square as

$$\text{R-square} = 1- \frac{SSE}{SST}$$

R-square (R^2) can take values between 0 and 1. Any value closer to 1 indicates that the model accounts for a larger fraction of the variance.

2.5 Results

2.5.1 Particle Size Measurements

The particle size measurements were performed using low angle laser scattering with Malvern Mastersizer 3000 Granulometer. The particles of microgel were considered as spheres and the refractive index is taken to be 1.5. For each sample, three consecutive runs at an obscuration of 13-16% were performed. The measurements provided numerical values of the median ($d_{0.5}$), the surface weighted mean ($d_{3,2}$) and the volume weighted mean ($d_{4,3}$). We used ultra-turraxed microgel suspensions and centrifuged microgel suspensions (the protocol of which is mentioned in section 1.3.1) for the measurements of the size distribution.

We first look into the particle size distribution curves obtained by laser diffraction for ultra-turraxed microgels in comparison with Microgel-IN (see Figure 2-6) while the numerical parameters obtained from the distribution are summarized in Table 2-2.

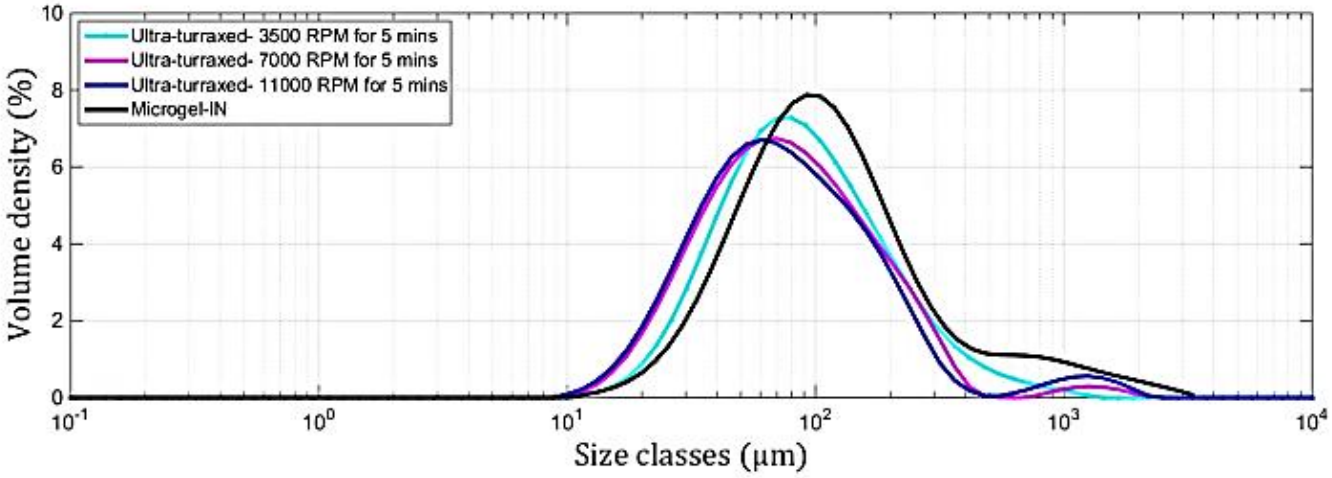

Figure 2-6 Particle size distribution of Ultra-turraxed Microgel suspension shown along with Microgel-IN

Table 2-1 Values measured for the surface weighted mean, volume weighted mean ,Average particle size and log normal particle size distribution for Ultra-turraxed Microgel and Microgel-IN.

	$(d_{4,3})$	$(d_{3,2})$	$(d_{0.5})$	***Span***
Microgel-IN	209	82.5	105	3.7
Ultra-turraxed-3500 RPM for 5 mins	116	64	79	2.5
Ultra-turraxed-7000 RPM for 5 mins	108	54	70	2.5

It can be clearly seen that the distribution is primarily monomodal with only a small peak appearing around 1000 µm. This small peak is believed to be due to the relatively short time used for the mechanical cutting which apparently are not long enough to break the large particles. It can be seen that the $d_{4,3}$ decreases as the cutting speed is increased which is expected as more particles are transported to the inside of the rotor of the mechanical cutter (refer to section 1.3.1 for more details). If the duration of the cutting is increased, there will enough time to break the bigger particles and we can expect to get rid of the small peak in the distribution curve for the ultra-turraxed microgel. The $d_{0.5}$ value shifts from 80µm to 70µm when the cutting speed is doubled but the width of the distribution remains the same (=2.5) for the two samples. But this width is decreased by a factor of 32% when compared to Microgel-IN indicating a slight decrease in the polydispersity resulting in a relatively narrower distribution due to the mechanical cutting. This $d_{0.5}$, although smaller than that of Microgel-IN, is still too large for the applications in flow experiments in model porous media used in this work.

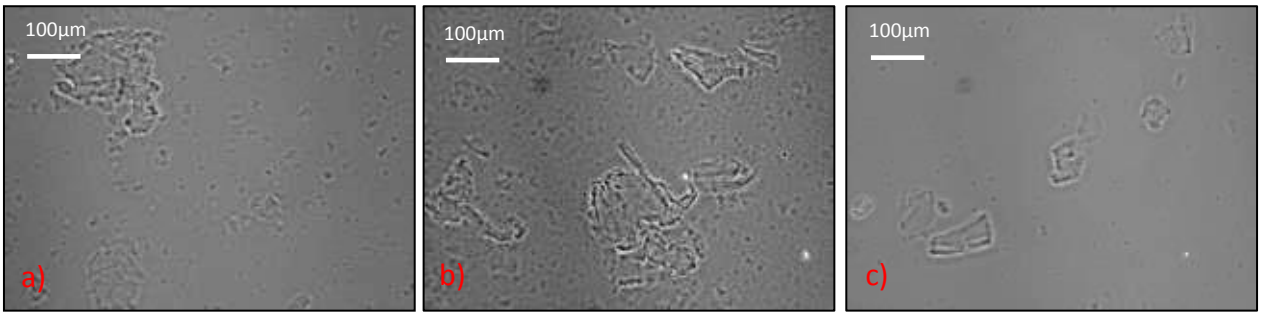

Figure 2-7 Phase contrast images of a). Microgel-IN, b). Ultra-turraxed-3500 RPM for 5 mins and c). Ultra-turraxed-7000 RPM for 5 mins.

As for the shape of the particles, it can be clearly seen in Figure 2-7, the particles are of random shapes as the mechanical cutting only rips apart the bigger non spherical particles resulting in arbitrary shapes of the microgel suspensions.

We now consider the case of centrifuged microgel suspensions, the yield based on the dry mass of the supernatant and sediment for different centrifugation conditions (the protocol for preparation is mentioned in section 1.3.1) are summarized in Table 2-2 and their particle size distribution as displayed in Figure 2-7.

Table 2-2 Table showing the average concentration (% wt.) of the supernatants and the sediments obtained after the centrifugation of 0.9% wt. of Microgel-IN ($\pm$ **is the population standard deviation**) (* Dry mass measurements).

	Concentration (% wt)*
Microgel-IN	0.90 ± 0.03
Microgel1000-10	0.76 ± 0.07
Microgel1000-10-Sediment	1.02 ± 0.07
Microgel2000-10	0.72 ± 0.05
Microgel2000-10-Sediment	1.06 ± 0.09
Microgel3000-10	0.66 ± 0.06
Microgel3000-10-Sediment	1.10 ± 0.04
Microgel4000-10	0.64 ± 0.05
Microgel4000-10-Sediment	1.12 ± 0.04

The supernatants of microgel suspensions obtained at different centrifugation speeds demonstrates the same trend as that of ultra-turraxed microgel. The De Broukere diameter

decreases on increasing the centrifugation speed. The $d_{0.5}$ of the supernatants reduces considerably from a value 105 µm (for **Microgel-IN**) to 25, 18 and 13 µm for centrifugation speeds 2000, 3000 and 4000 RPM respectively. The distribution is clearly monomodal with a second shoulder seen in some distribution curves. This is due to a small proportion of the bigger particles from the stock suspension in the supernatants. For the rest of the work shown in this thesis, we will be using only the supernatants of Microgel2000-10 and Microgel4000-10 which are named as **Microgel2000-10** and **Microgel4000-10**. The particle size distribution for Microgel2000-10 and Microgel4000-10 display a narrower monomodal distribution with the width of the distribution reduced by 62% and 48% respectively as compared to Microgel-IN (see Figure 2-8). The narrowing of the width implies that the suspensions are relatively more homogenous and less polydispersed. This can also be seen in the phase contrast micrographs shown in Figure 2-9**.** The mean particle size is almost halved as the centrifugation speed is doubled (refer to Table 2-3).

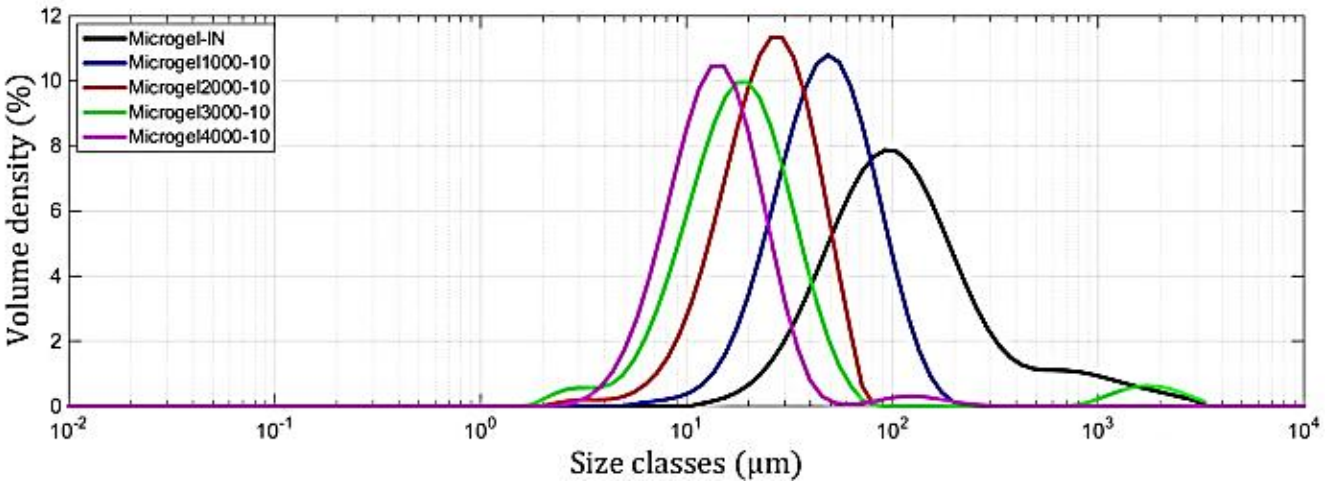

Figure 2-8 Particle size distribution of centrifuged Microgel (Microgel1000-10; Microgel2000-10; Microgel3000-10 and Microgel4000-10) shown in comparison with Microgel-IN.

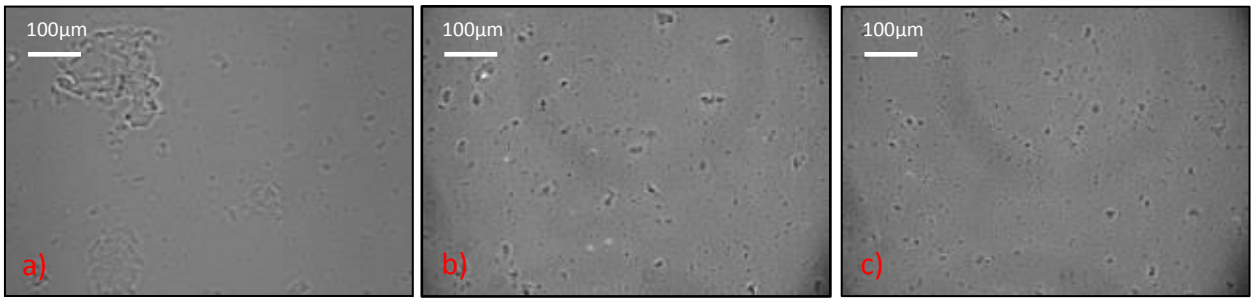

Figure 2-9 Phase contrast images of (a) Microgel-IN, (b) Microgel2000-10 and, (c) Microgel4000-10

Table 2-3 Value measured for the surface weighted mean, volume weighted mean ,average particle size and span of the distribution for centrifuged supernatants of microgel suspension at different speeds and their sediment along with and Microgel-IN.

	$d_{4,3}$	$d_{3,2}$	$d_{0.5}$	***Span***
Microgel-IN	209	82	105	3.7
Microgel1000-10	53	39	47	1.5
Microgel1000-10-Sediment	322	104	125	7.2
Microgel2000-10	27	20	25	1.4
Microgel2000-10-Sediment	137	79	97	2.3
Microgel3000-10	88	14	18	1.8
Microgel3000-10-Sediment	156	82	101	2.8
Microgel4000-10	21	11	13	1.9
Microgel4000-10-Sediment	141	78	97	2.4

To understand the role of the bigger particles removed by centrifugation, we compare the particle size distribution of the sediments, supernatants (obtained after centrifugation of the microgel suspensions at different speeds) and 0.9% wt. Microgel-IN (stock suspension). From Figure 2-10, we see that the sediments and Microgel-IN have almost the same $d_{0.5}$ ranging from 97-125 µm with some big particles. These big particles can either be formed due to the aggregation of particles or they are big lumps of cross-linked microgel.

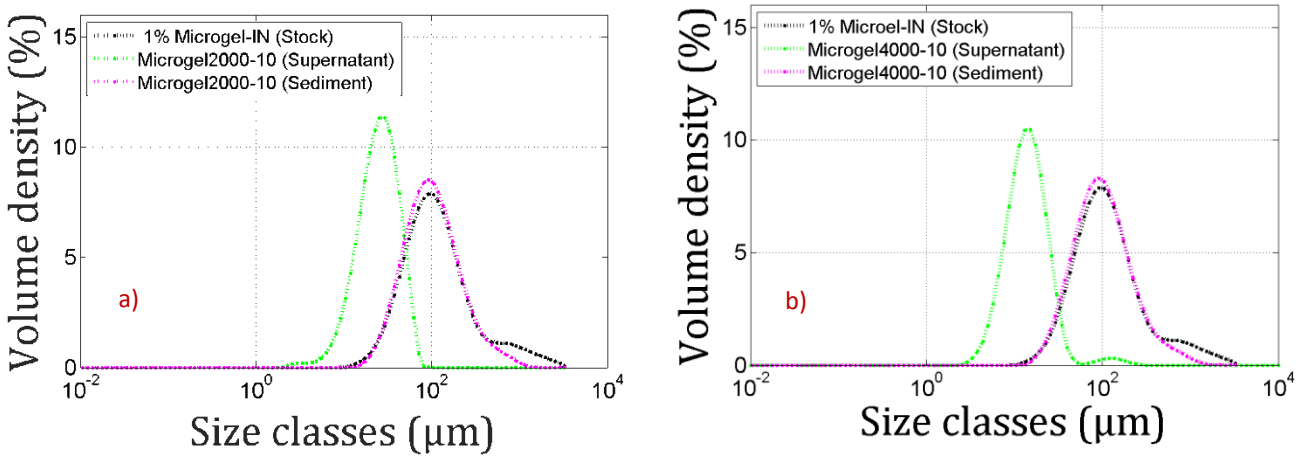

Figure 2-10 Particle size distribution of Microgel-IN in comparison with the supernatant and sediment of, (a) Microgel2000-10, and (b) Microgel4000-10 respectively.

I. High Concentrations of centrifuged microgel suspension

The objective here is to get some idea about the critical concentration at which the particles in the suspension start to form aggregates. This critical concentration will allow us to understand the nature of interactions, its significance in the jamming mechanism and the rheology of the suspensions. Figure 2-11 and 2-12 show the particle size distribution curves of various concentration of Microgel2000-10 and Microgel4000-10 respectively. The curves clearly depict the variation of the particle size with concentration. In Microgel2000-10, the distribution stays monomodal for concentration 1.34% wt. with $d_{0.5}$ changing slightly from 27 µm to 31 µm compared to 0.8%wt. implying marginal increase in size of the particles with concentration. A similar trend is observed for 1.2% wt. and 1.6%wt. of Microgel4000-10, where the $d_{0.5}$ is seen to increase to 12.7 µm and 15.6 µm as compared to 0.7% wt. The monomodal characteristic of the distribution curve is lost with further increase in the concentration for both Microgel2000-10 and Microgel4000-10. This increase is due to the aggregation of the particles. As the solvent is removed from the suspension, the particle due to their sticky amphiphilic nature come closer and form aggregates. A progressive change is observed where there are less small particles and more big particles above concentration, c = 2% wt. Microgel4000-10 and Microgel2000-10. We will see in later sections, the effect of concentration above 2% wt. on the rheology of the suspensions.

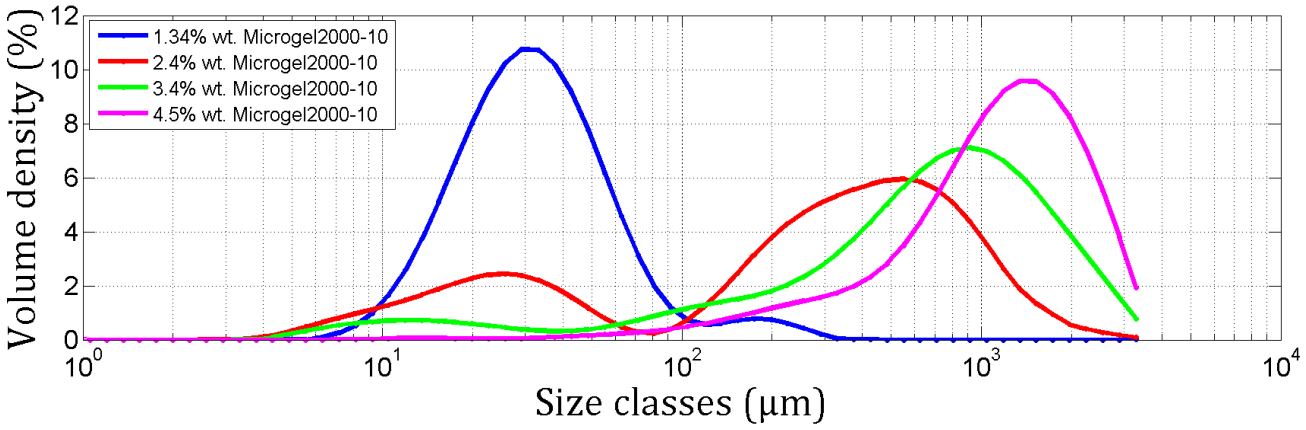

Figure 2-11 Particle size distribution curves for varied concentration of Microgel2000-10

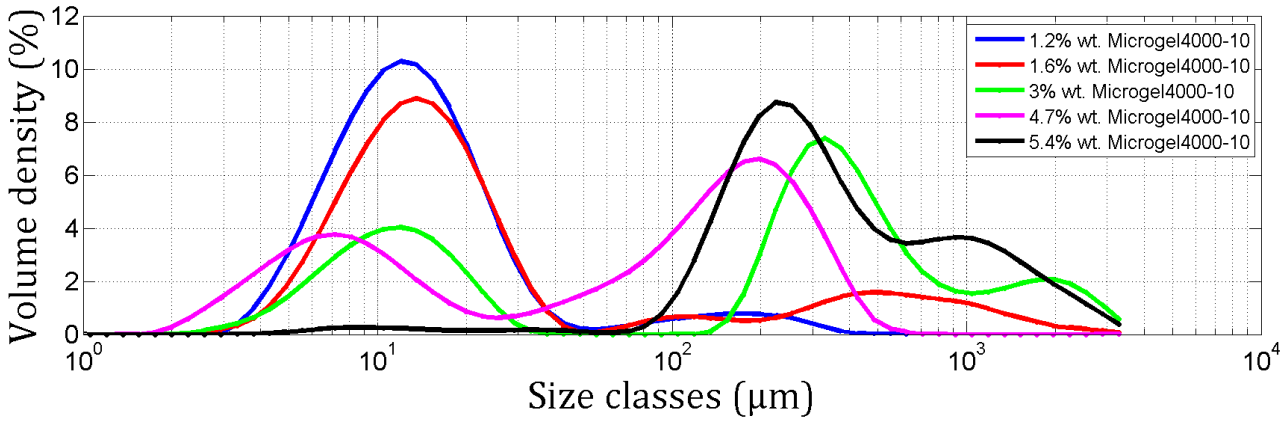

Figure 2-12 Particle size distribution curves for varied concentration of Microgel4000-10

Table 2-4 Value measured for the surface weighted mean, volume weighted mean, average particle size for different concentration of Microgel4000-10 and Microgel2000-10.

Microgel4000-10				**Microgel2000-10**			
Concentration, *c* (% wt.)	$d_{4,3}$	$d_{3,2}$	$d_{0.5}$	**Concentration, *c* (% wt.)**	$d_{4,3}$	$d_{3,2}$	$d_{0.5}$
1.2	24.2	11.2	12.7	1.34	40.2	27.2	31.2
1.6	147	14.1	15.6	2.4	427	56.3	319
3	458	25.2	282	3.4	1250	250	1160
4.7	117	15.4	93.9	4.5	1270	566	1180
5.4	554	171	309				

2.5.2 Flow Behaviour

I. Reference fluid- Water

As there can be errors in rheological testing due to several factors, it is important to do measurements with a reference fluid to examine the validity of the experiments. In this case, we used de-ionized water as a reference fluid and measure its viscosity to determine the accuracy of the rheometer for the low viscosity microgel suspensions where the torque is low (the error will be much less for more viscous samples). The experimental finding in terms of viscosity of water (at 25°C) was found to be 0.99 $\pm$ 0.00009 mPa s which is in agreement with the literature value (= 0.9 mPa s) with an error of 10%.

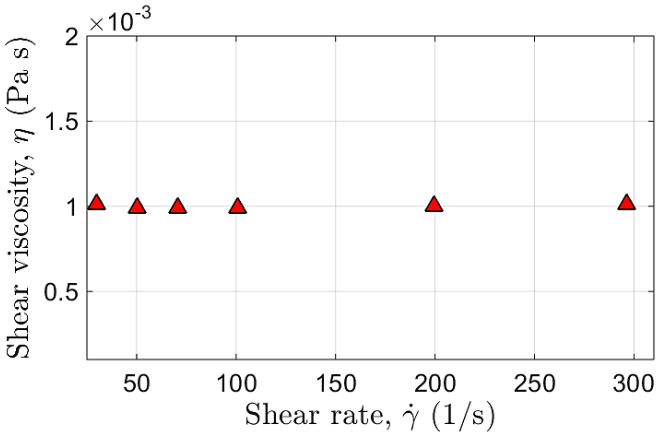

Figure 2-13 Shear viscosity as a function of shear rate for water using double gap geometry.

II. Microgel Suspensions

In this section, we will study the flow behaviour of the suspensions of Microgel4000-10, Microgel2000-10 and Microgel-IN under steady shear stress (for both incrementing and decrementing shear stress steps) for different concentrations and determine the appropriate constitutive flow models that the different microgel suspensions follow.

It is evident from the flow curves in Figure 2-14, 2-15 and 2-16 that the suspensions characteristically exhibits a non-Newtonian behaviour. It can be seen that the suspension has shear thinning behaviour for both incrementing and decrementing stress steps. As the concentration, *c*, increases the system becomes highly shear thinning. In fact, the curves indicate a strong shear stress dependency on shear rate which very well described by power law model

for a certain range of concentrations and by the Herschel-Bulkley model with yield stress, σ_y beyond the aforementioned concentration range. We obtained the parameters for the power law model for all concentrations from 0.3% wt. to 6% wt. of Microgel4000-10, from 0.3% wt. to 5% wt. of Microgel2000-10 and 0.4% wt. to 3.3% wt. of Microgel-IN and they are summarized in Table 2-5, Table 2-7 & Table 2-9. It was observed that the concentrations beyond 6% wt., 5% wt. and 3.3% wt. of Microgel4000-10, Microgel2000-10 and Microgel-IN respectively are not homogenous and are quite lumpy. They are very well described by the Herchel-Bulkey model which yields the parameters σ_y , n and k and they are shown Table 2-6, 2-8 and 2-10.

From the fitting, it was seen that R^2 of all the fits values for all concentrations are found to be near 0.99, which clearly suggests a good fit of the model. The SSE is also evaluated for the fits, the value is seen to be very small and close to zero suggesting that there is a minimum random error component and that the fit is useful and good for predictions.

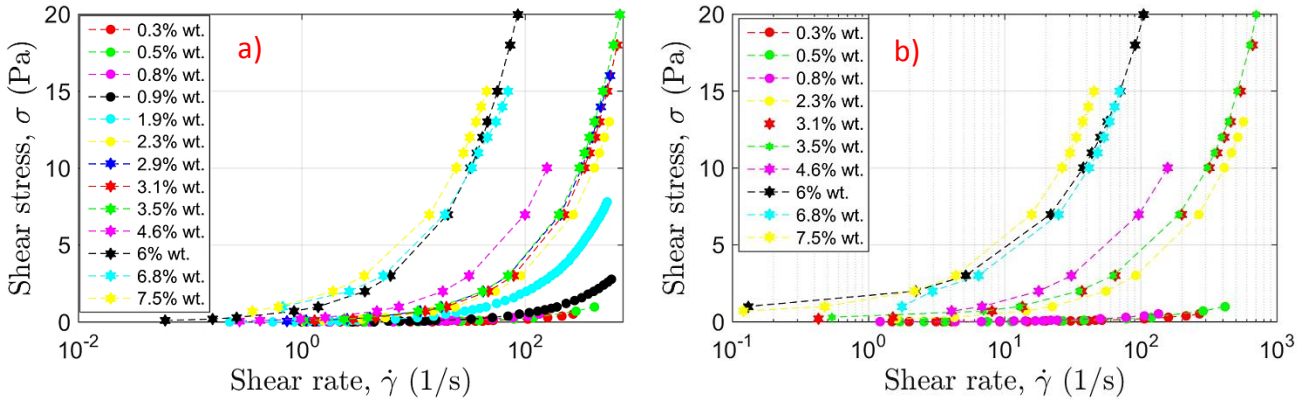

Figure 2-14 Steady shear flow curve for concentrations ranging from 0.3% wt to 7.5% wt for Microgel4000-10 for both incrementing (a), and decrementing (b) shear stress steps.

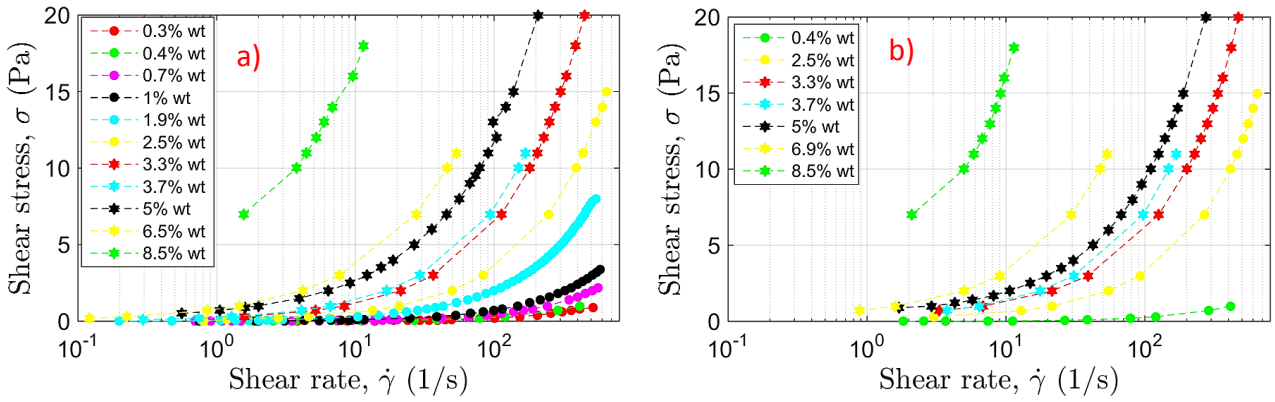

Figure 2-15 Steady shear flow curves for concentrations ranging from 0.3% wt to 8.5% wt for Microgel2000-10 for both incrementing (a), and decrementing (b) shear stress steps.

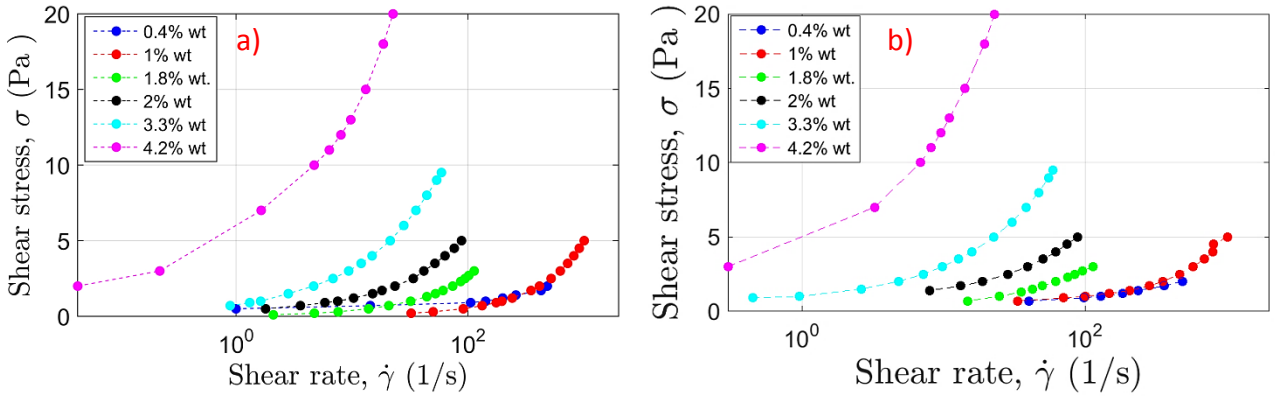

Figure 2-16 Steady shear flow curves for concentrations ranging from 0.4% wt to 4.2% wt for Microgel-IN for both incrementing (a), and decrementing (b) shear stress steps.

For more quantitative understanding, it is useful to evaluate the consistency factor, k (Pa s^n) and the power law index (n) for the three different microgels. Understandably, concentrations below 0.8% wt. for Microgel4000-10 and 0.7% wt. for Microgel2000-10 display a near Newtonian behaviour with n > 0.97. The consistency factor increases with concentration of the microgel suspensions for both incrementing and decrementing shear stress steps. This is quite obvious as with increase in the particle concentration, the viscosity increases which in reflected in the consistency factor.

Table 2-5 Power Law parameters for different concentration of Microgel4000-10 for both incrementing and decrementing shear stress steps along with R^2 values and the standard error (SSE).

Microgel4000-10								
Incrementing shear stress					Decrementing shear stress			
Concentration (% wt.)	k (Pa s^n)	n (-)	SSE	R^2	k (Pa s^n)	n (-)	SSE	R^2
0.3	0.002	0.976	16×10^{-5}	1	0.002	0.975	2.3×10^{-5}	0.99
0.5	0.003	0.969	7×10^{-6}	1	0.003	0.971	9.8×10^{-6}	1
0.8	0.005	0.940	2×10^{-6}	1	0.005	0.942	4.6×10^{-6}	1
2.3	0.076	0.811	26×10^{-3}	0.99	0.078	0.806	21×10^{-3}	0.99
3.1	0.073	0.847	88×10^{-3}	0.99	0.113	0.777	0.3	0.99
3.5	0.090	0.824	33×10^{-3}	0.99	0.1	0.805	0.66	0.99
4.6	0.221	0.753	6×10^{-3}	0.99	0.240	0.737	1.1×10^{-3}	1
6	0.973	0.677	1.948	0.99	0.65	0.74	4.5	0.99
6.8	1.229	0.592	0.430	0.99	0.736	0.705	0.553	0.99

Table 2-6 Herschel-Bulkley parameters for lumpy Microgel4000-10 of concentration, c = 7.5% wt. for both incrementing and decrementing shear stress steps along with R^2 values and the standard error (SSE).

Microgel4000-10										
Incrementing shear stress						Decrementing shear stress				
Concentration (% wt.)	σ_y (Pa)	k (Pa s^n)	n (-)	SSE	R^2	σ_y (Pa)	k (Pa s^n)	n (-)	SSE	R^2
7.5	0.1	1.248	0.651	0.0025	1	0.6	0.758	0.772	25×10^{-3}	0.999

Table 2-7 Power Law parameters for different concentration of Microgel2000-10 for both incrementing and decrementing shear stress steps along with R^2 values and the standard error (SSE).

Microgel2000-10								
Incrementing shear stress					Decrementing shear stress			
Concentration (% wt.)	k (Pa s^n)	n (-)	SSE	R^2	k (Pa s^n)	n (-)	SSE	R^2
0.4	0.003	0.969	1.2×10^{-6}	1	0.002922	0.968	0.000015	1
2.5	0.092	0.786	0.014	1	0.006627	0.835	0.1717	0.99
3.3	0.201	0.753	0.084	0.99	0.131	0.817	0.8229	0.99
3.7	0.241	0.745	0.013	0.99	0.2185	0.763	0.06909	0.99
4.1	0.292	0.749	0.053	0.99	0.3122	0.732	0.02328	0.99
4.3	0.339	0.777	0.068	0.99	0.2818	0.849	0.3227	0.99
4.5	0.386	0.724	0.050	0.99	0.3667	0.710	0.3756	0.98
5	0.475	0.702	1.611	0.99	0.1921	0.738	14.02	0.99

Table 2-8 Herschel-Bulkley parameters for lumpy Microgel2000-10 of concentration, c = 6.5% wt. and 8.5% wt. for both incrementing and decrementing shear stress steps along with R^2 values and the standard error (SSE).

Microgel2000-10										
Incrementing shear stress						Decrementing shear stress				
Concentration (% wt.)	σ_y (Pa)	k (Pa s^n)	n (-)	SSE	R^2	σ_y (Pa)	k (Pa s^n)	n (-)	SSE	R^2
6.9	0.027	0.749	0.675	0.0015	1	0.287	0.488	0.775	0.01028	0.99
8.5	2.077	3.719	0.593	0.2858	0.99	5.487	0.609	1.24	0.08427	0.99

Table 2-9 Power Law parameters for concentration ranging from 0.8% wt. to 3.3% wt. of Microgel-IN for both incrementing and decrementing shear stress steps along with R^2 values and the standard error (SSE).

Microgel-IN								
Incrementing shear stress					Decrementing shear stress			
Concentration (% wt.)	k (Pa s^n)	n (-)	SSE	R^2	k (Pa s^n)	n (-)	SSE	R^2
0.8	0.005	0.996	0.03085	0.99	0.023	0.773	0.545	0.98
1.8	0.053	0.848	0.01139	0.99	0.102	0.718	5.8×10^{-3}	0.99
2.2	0.235	0.682	0.03223	0.99	0.375	0.575	0.055	0.99
3.3	0.755	0.622	0.02008	0.99	0.737	0.621	0.419	0.99

Table 2-10 Herschel-Bulkley parameters for concentration, c = 4.2% wt. of Microgel-IN for both incrementing and decrementing shear stress steps along with R^2 values and the standard error (SSE).

Microgel-IN										
Incrementing shear stress						Decrementing shear stress				
Concentration (% wt.)	σ_y (Pa)	k (Pa s^n)	n (-)	SSE	R^2	σ_y (Pa)	k (Pa s^n)	n (-)	SSE	R^2
4.2	2.2	1.297	0.775	0.425	0.99	2.1	2.161	0.674	0.069	0.99

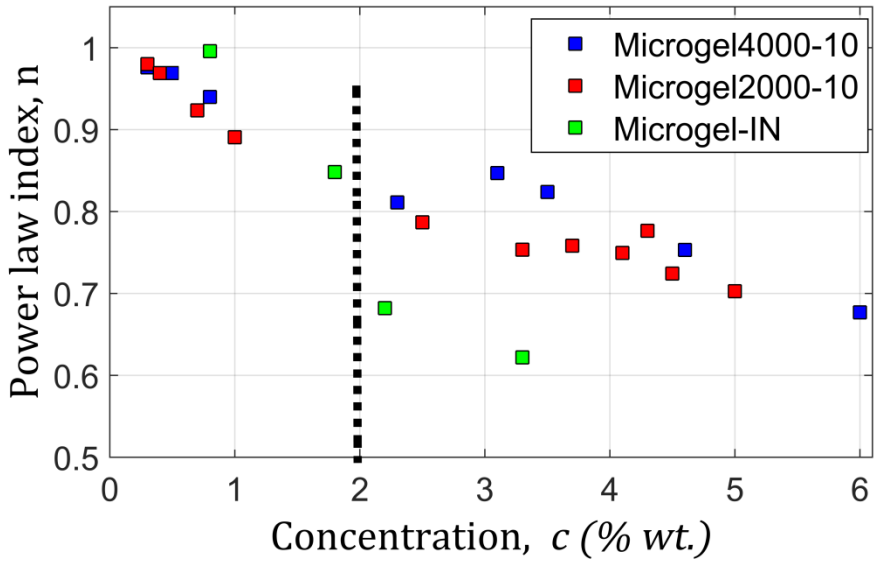

Figure 2-17 Plot of power law index, n as a function of concentration, c (% wt) for Microgel4000-10, Microgel2000-10 and Microgel-IN for incrementing shear stress steps.

The power law index, n, is always less than unity for all concentrations of Microgel4000-10, Microgel2000-10 and Microgel-IN. However, the value of the power law index is seen to be different for each concentration in the incrementing and decrementing shear stress steps. This unusual behaviour is explained in detail in section2.5.6. For now, we will only describe the microgel suspension behaviour in the incrementing shear stress step. From Figure 2-17, it can be seen that the values of n decreases more rapidly for Microgel-IN (much stronger dependence on concentration) than for Microgel2000-10 and then Microgel4000-10 implying that the non-Newtonian behaviour is more noticeable at lower concentrations for Microgel-IN. The value of n changes from 0.98 to 0.68 for a concentration change from 0.3% to 6% wt. for Microgel4000-10 and from 0.98 to 0.70 for a concentration change from 0.4% to 5% wt. for Microgel2000-10. Till a critical concentration of 2% wt., the value of n is more or less same for Microgel4000-10 and Microgel2000-10. This result lies in agreement with the results of particle size distribution of different concentrations of the suspension which clearly shows the onset of particle aggregation beyond a concentration, c = 2% wt. This aggregation has an major impact on the shear thinning behaviour of the suspension beyong 2% wt.

Beyond, 6% and 5% wt., for Microgel4000-10 and Microgel2000-10, the lumpiness and inhomogeneity in the suspension is a clear indication of the transition from a homogenous suspension. Nevertheless we performed the rheology on these suspensions (and measured the dry mass from the recuperated sample). This concentration at which this transition takes place corresponds to jamming concentration, c_j , which starts when the suspension becomes a yield stress gel. Clearly, we find a measurable yield stress for concentration 6.8% < c_j < 7.5% for Microgel4000-10 and 6.9% < c_j < 8.5% for Microgel2000-10. Similarly, the yield stress is found to be 2.2 Pa for 4.2% wt. of Microgel-IN (see Figure 2-18).

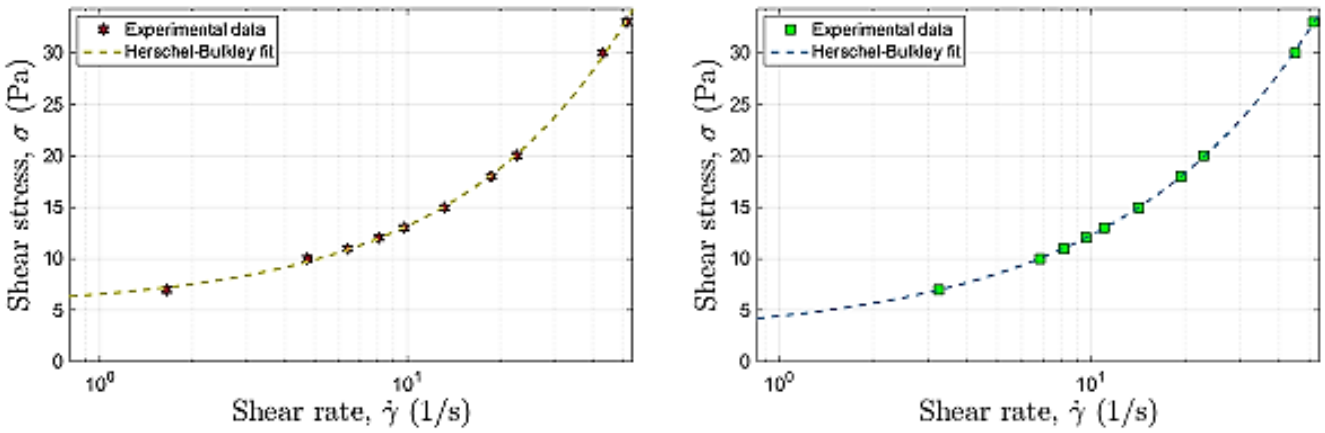

Figure 2-18 Typical plot of shear stress (Pa) as a function of shear rate (1/s) for 4.2% of Microgel-IN for both incrementing (a), and decrementing (b) shear stress steps.

2.5.3 Aging of Suspensions

To study the aging phenomenon i.e how the dilute microgel suspensions evolve with time, we performed the flow measurements on 0.7% of Microgel4000-10 and 0.8% of Microgel2000-10 (prepared by centrifugation) over a course of 17 days. The motivation behind this test is to determine how significantly the dilute microgel suspensions change between the time of preparation and the filtration experiments. As mentioned in section 2.5.2, the power law curve fitting is done on each experimental data set and the power law parameters were calculated.

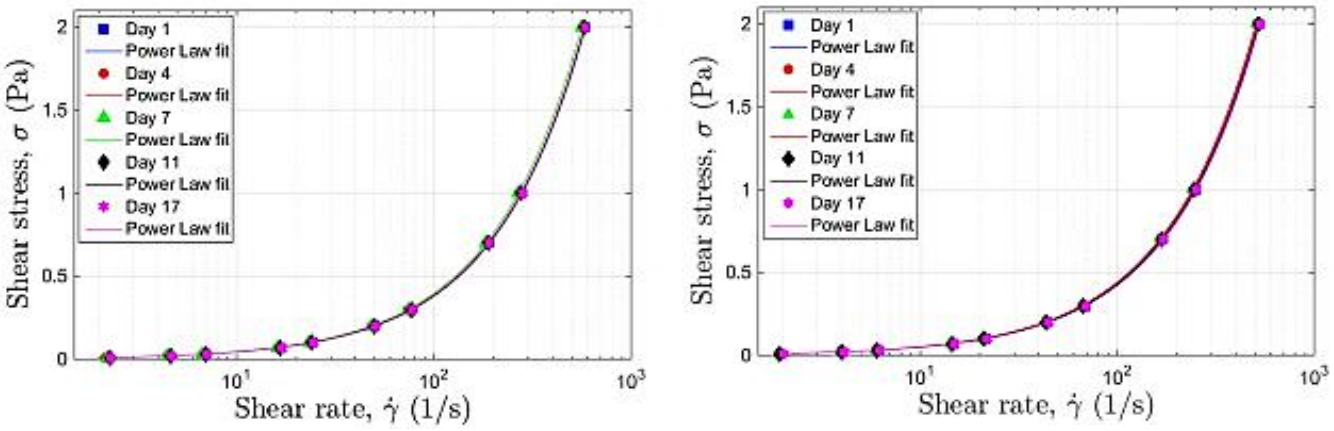

Figure 2-19 Flow curves for Microgel4000-10 and Microgel2000-10 at different times.

The average of the power law parameters for all the experimental data taken over a course of 17 days are found to be

Microgel4000-10 : $k = 0.0051 \pm 0.0001$ Pa s^n

$n = 0.9381 \pm 0.0008$

Microgel2000-10 : $k = 0.0059 \pm 0.0001$ Pa s^n

$n = 0.9300 \pm 0.0003$

The small value of standard deviation signifies that the rheological properties are only marginally changed over the course of 17 days indicating that the dilute suspension doesn't age. (± denotes the standard deviation)

2.5.4 Particle Volume Fraction

Figure 2-20, 2-21 and 2-22 display the shear viscosity as a function of shear rate for incrementing shear stress steps for Microgel4000-10, Microgel2000-10 and Microgel-IN of different concentrations respectively.

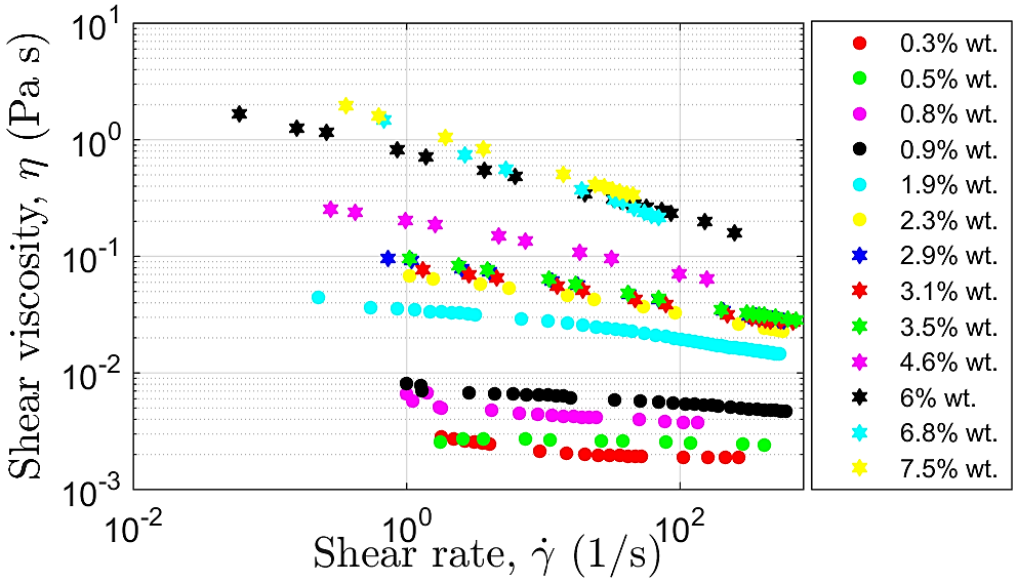

Figure 2-20 Shear viscosity as a function of shear rate for incrementing shear stress steps for concentrations ranging from 0.1 to 7.5% wt. of Microgel4000-10.

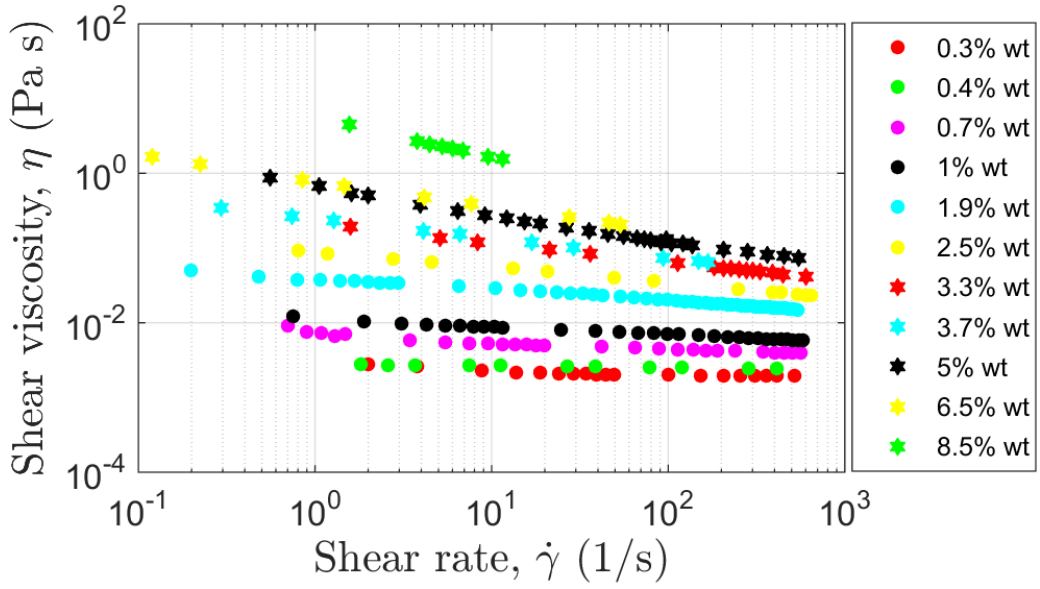

Figure 2-21 Shear viscosity as a function of shear rate for incrementing shear stress steps for concentrations ranging from 0.3 to 8.5% wt. of Microgel2000-10.

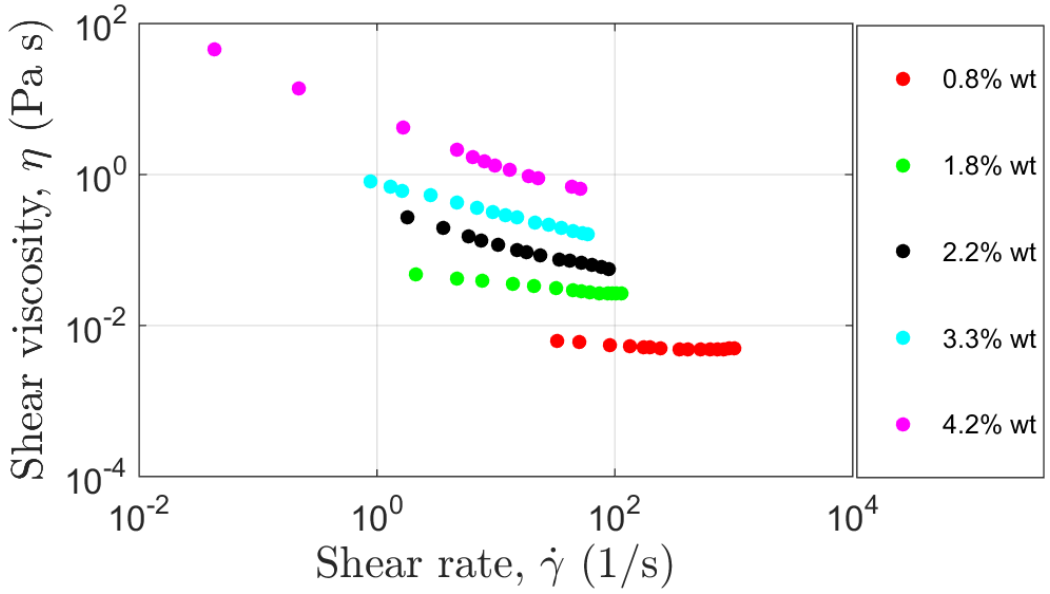

Figure 2-22 Shear viscosity as a function of shear rate for incrementing shear stress steps for concentrations ranging from 0.8 to 4.2% wt. of Microgel-IN.

We now plot the relative viscosity, η_r as a function of concentration, c (% wt.) for the microgels where, $\eta_r = \frac{\eta_o}{\eta_s}$, where and η_s is the solvent viscosity (which in this case is water) for all the

concentrations. First, we show the relative viscosity, η_r evaluated at 0.1 s^{-1} plotted as a function of concentration, c (% wt.) in Figure 2-23.

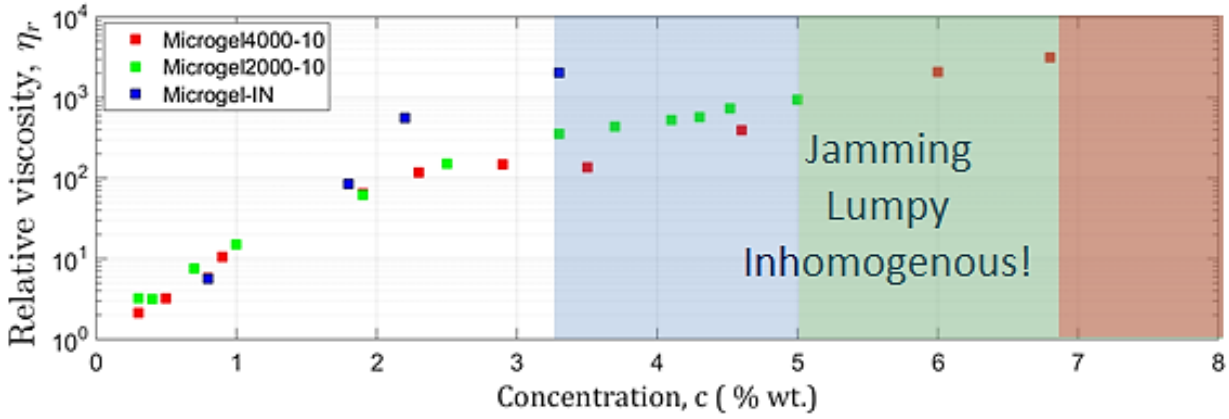

Figure 2-23 Plot of relative viscosity (calculated at 0.1 s^{-1} using power law coefficients) as a function of concentration (% wt.) for Microgel4000-10, Microgel2000-10 and Microgel-IN.

From experiments, it is well known that at low concentrations, microgels are purely viscous (Borrega et al., 1999; Cloitre et al., 2003). The viscosity first increases slowly with increase in the concentration and then it increase sharply. This divergence of the viscosity at c_m (% wt.) is one of the distinguishing characteristic of soft particles like microgel suspensions. As can be noticed, Microgel-IN reaches a higher viscosity at a lower concentration than Microgel2000-10 and Microgel4000-10. As the concentration rises, the particles come closer, they become more densely packed and the fluid resistance against its moving layers increases resulting in increase in viscosity.

Now we will only consider the case of Microgel4000-10. In Figure 2-24, We used extrapolated values of apparent viscosity, $\eta(\dot{\gamma})$ at four different shear rate, $\dot{\gamma}$, of 0.1, 1, 10 and 100 s^{-1} using the power law coefficients (k and n) for the model fitting since we cannot access zero shear Newtonian viscosity due to sensitivity limitations of the rheometer in measuring viscosities at extremely low shear rates. In the same graph, we also plot viscous modulus of the suspension measured in the LVR for various concentrations and normalized by the viscous modulus obtained for water i.e G''(microgel)/G''(water)= η_r. Clearly, the experimental curves is not described by

Krieger-Dougherty even considering ϕ_m = 0.64. This indicates to the importance of using zero shear Newtonian viscosity, unfortunately unavailable here and also the fact that Krieger-Dougherty is valid for the case of hard-spheres.

The graph can be classified into in three regimes: Regime 1 where the relative viscosity, η_r is seen to increase rapidly with the concentration. This regime lasts till concentration 2%wt. Beyond this concentration, the relative viscosity is seen to increase only slightly with the concentration and remains more or less the same. This is Regime 2 which lasts till 7% wt. Beyond this, the suspension acts like a yield stress fluid finally turning into a gel with ϕ_m = 1. This is also the regime where a strong thinning (small n values) has been observed.

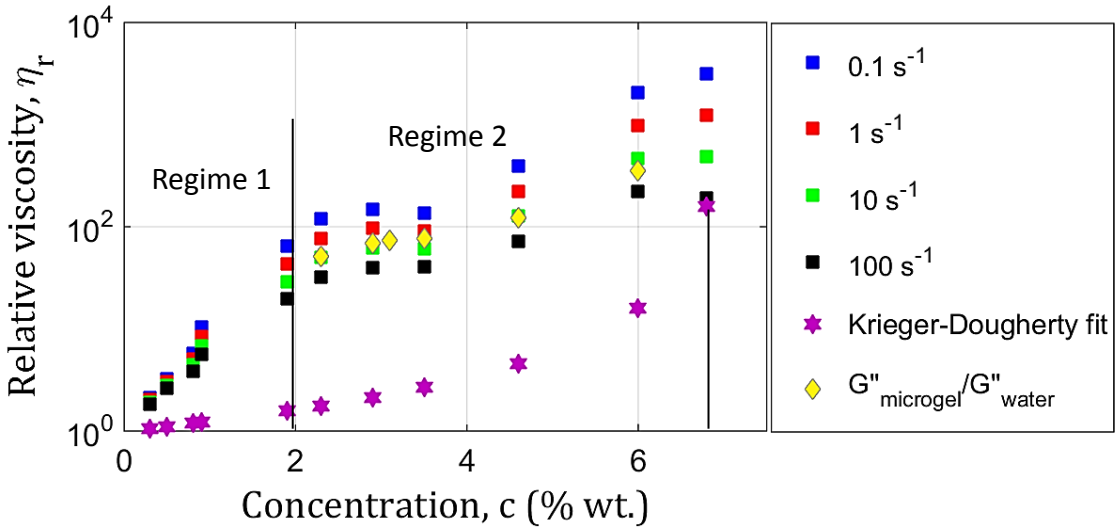

Figure 2-24 Typical relative viscosity calculated by extrapolation using power law parameters at shear rates 0.1,1, 10 and 100 s^{-1} as a function of different concentration of Microgel4000-10 along with the Krieger-dougherty fit evaluated with $\boldsymbol{\phi_m}$ = 0.64 and ratio of the loss modulus, G'' evaluated for microgel and water at 1%.

We speculate that our suspensions are not made of perfectly spherical particles instead they are more elongated particles with dimension L and l such that α = L/l. Also, from light diffraction we know that the size of the particles measured is the size of the sphere which occupies the exact same volume as the particle given as $r^3 = L*l^2$. In the Regime 2, we observe a strong thinning and a smooth variation of the relative viscosity with concentration, which can be assumed due to the ordering/alignment of the non spherical particles.

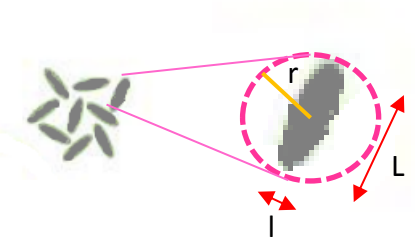

Assuming, r_h to be the hydrodynamic radius of the particles when they interact hydrodynamically with each other with no alignment, $(r_h)^3 \approx L^3$. So, $(r_h/r)^3 = (L/l)^2 = \alpha^2$. To evaluate the value of α, we postulate that the viscosity of the suspension of particles of volume r_h^3 would diverge at a concentration of order 2%, whereas the viscosity of the suspension of the actual particles of volume $r^3=Ll^2$ diverge at a concentration of order 7%. This gives α=1.87, indicating at the fact that the particles are more elongated than they are spherical (consistent with Figure 2.9). This might explain the observations of Regime 2, where the particles are more orderly and their viscosity does not increase up until the last particle which is added then leads the suspension to a jammed state characterized by a yield stress. Hence, Krieger-Dougherty is clearly not a model of choice for our system to determine the particle volume fraction.

We now try to estimate roughly the jamming fraction of the Microgel4000-10 and Microgel2000-10 using the results from the bulk rheology and maximum concentration as obtained in chapter 5. Typically, ϕ_m represents the maximum packing fraction when the particles are closely packed. In ideal situations, ϕ_m= 1. This ϕ_m corresponds to c_m (% wt.) . The jamming concentration, c_j corresponds to ϕ_j the jamming fraction. For non-frictional hard spheres, ϕ_j= 0.64 but for soft particles ϕ_j can be written in terms of c_j and c_m.

$$\phi_j = \frac{c_j}{c_m}$$

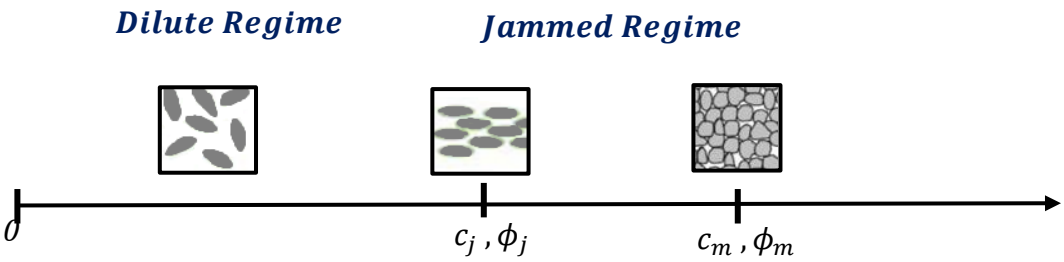

Microgel4000-10	$c_j = 7.5\ \%\ wt.$, $\phi_j = 0.62$	$c_m = 12.1\ \%\ wt.$
Microgel2000-10	$c_j = 7\%\ wt.$, $\phi_j = 0.57$	$c_m = 12.3\ \%\ wt.$

Figure 2-25 Schematic illustration depicting the packing of the microgel suspension in the jammed regime for Microgel4000-10, Microgel2000-10 and Microgel-IN with the calculated jamming fraction, $\boldsymbol{\phi_j}$

Using the equation, we estimated ϕ_j to 0.62 and 0.57 for Microgel4000-10 and Microgel2000-10 respectively, which is close to the value one get for hard spheres.

2.5.5 Linear Viscoelasticity

We carried out dynamic strain sweep tests on the sample at strain amplitudes ranging from 0.1 % to 1000 % at a constant frequency of 1 Hz. The linear viscoelastic region (LVR) is described by the storage modulus (G') and the loss modulus (G''), both of which remain constant in LVR. The concentration dependence of the elastic and loss modulus is depicted in Figure 2-26 for Microgel4000-10, Microgel2000-10 and Microgel-IN. The data shown here depicts all G' values taken from LVR while the G'' for all concentrations are taken at a constant shear strain, γ= 1%. We will first consider the case of Microgel4000-10 and Microgel2000-10 where it is seen that in the linear viscoelastic region, G'' is higher than G' for all concentrations implying that the suspension behaves more liquid-like and below close packing. G' and G'' show an increase by 20 and 7 times larger respectively as the concentration increases from 2.3 to 6 % wt. for Microgel4000-10 signifying that the suspension is approaching the close packing limit as the concentration increases. It is worth noting that the G'' increase with concentration is consistent with the steady shear viscosity increase (Figure 2.24). This increase is 8 and 5 times larger respectively for 2.5 to 5 % wt. concentration increase in Microgel2000-10. The particles are not fully swollen and likely to be deformed. As the concentration increases, they become

progressively deformed and G'> G'', the data for those concentrations is not considered in this work. However, in the case of Microgel-IN, for concentrations < 2.2% wt., G'' was found to be greater than G'. One can easily say that in Microgel-IN, even at lower concentration the particles are tightly packed and significantly deformed. Increasing the strain causes G' and G'' to decrease signifying the end of the linear viscoelastic regime.

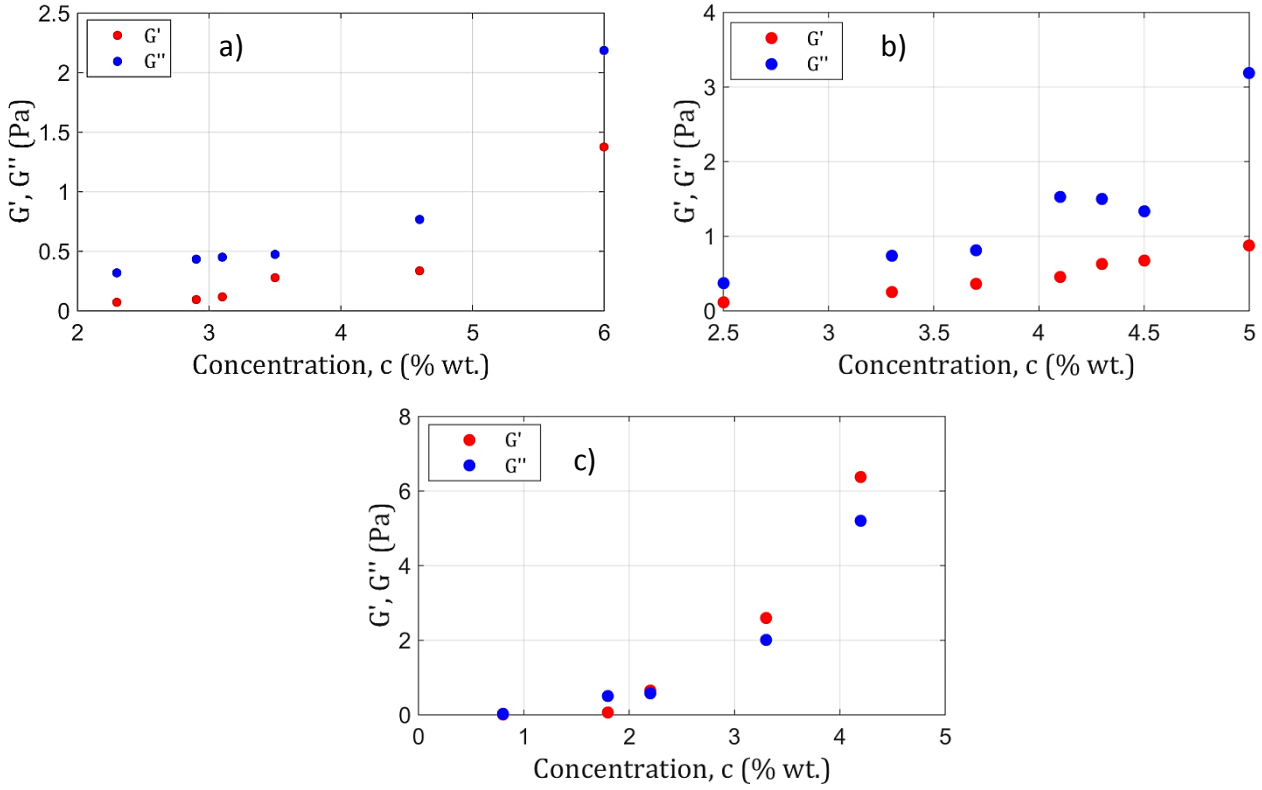

Figure 2-26 Plots of Storage Modulus, G' (Pa) and Loss Modulus, G'' (Pa) as a function of concentration, c (% wt.) for (a) Microgel4000-10, (b) Microgel2000-10, (c). Microgel-IN

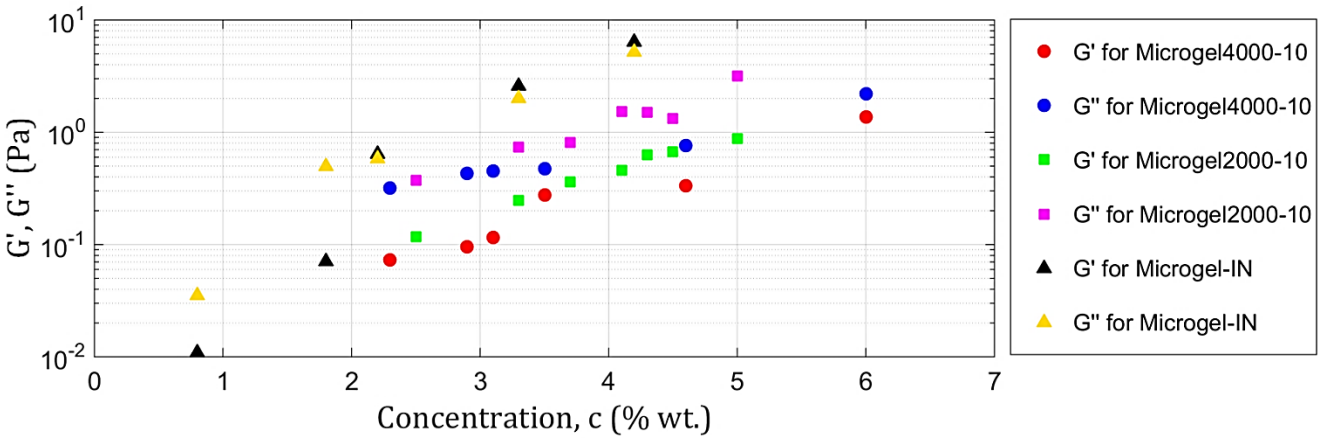

Figure 2-27 Plots of Storage Modulus, G' (Pa) and Loss Modulus, G'' (Pa) as a function of concentration, c (% wt.) represent a comparison of how G' and G'' for the three different microgel suspensions.

2.5.6 Shear-induced Aggregation

In this section, we show the case of shear induced aggregation taking place as evidenced from the bulk rheological results in incrementing and decrementing shear stress steps and the oscillatory measurements done before and after the flow measurements. We first show this with one example of 2.5% wt. Microgel2000-10 although it is observed for all the microgel suspensions beyond a certain concentration. This concentration was found to be greater than 2% wt. for Microgel2000-10 and Microgel4000-10, which makes complete sense as this is the concentration where aggregates starts to form (see section 2.5.1). In Figure 2-28, we see the evolution of the shear viscosity at a constant stress, σ = 0.2 Pa in both incrementing and decrementing stress. We clearly see the viscosity diverging in the decrementing step. It is reminiscent of slow creep flows in yield stress fluids, and it is a clear indication of the power law fluid turning into an yield stress fluid after an application of shear as high as 650 s^{-1}. This is also evidenced from the increase in G' value of the suspension after the flow measurements (Figure 2-29). We noticed that the suspension which was initially dominated by viscous behaviour (G''> G') turned into a suspension with a dominating elastic behaviour (G'> G''). Similarly, we extrapolated the values of apparent shear viscosities at a shear rate, 1 s^{-1} using the power law and Herschel-Bulkley parameters at the incrementing and decrementing steps. The % increase in the apparent shear viscosity was found to be 238% for 2.5 % wt. Microgel2000-10.

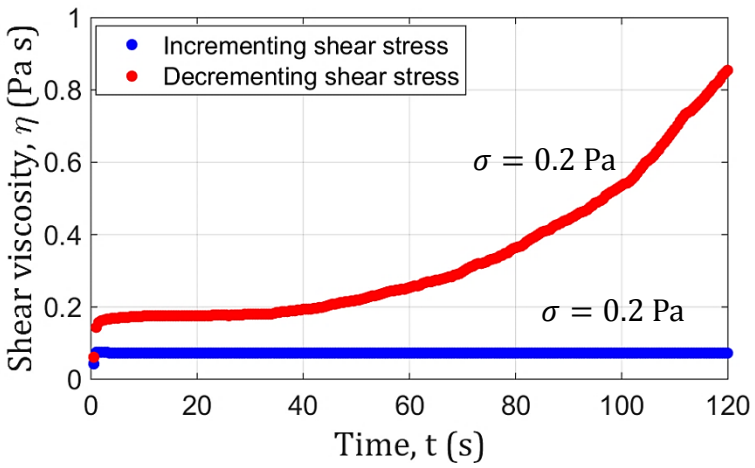

Figure 2-28 Plot showing the evolution of shear viscosity with time for the same shear stress, $\boldsymbol{\sigma}$ =0.2 Pa in the incrementing (blue) and decrementing (red) shear stress steps for 2.5% wt. Microgel2000-10.

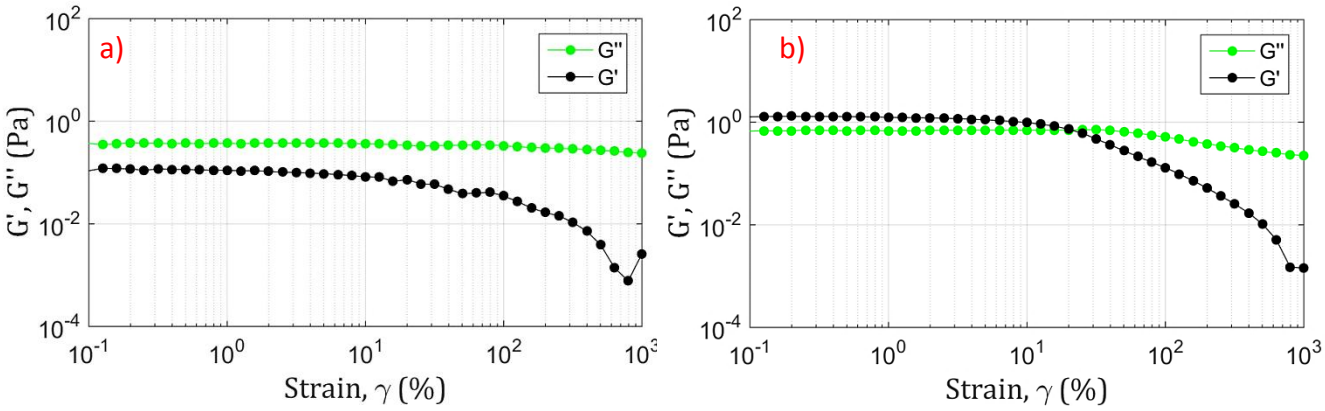

Figure 2-29 Elastic modulus,G' (Pa) and viscous modulus, G'' (Pa) plotted against strain, $\boldsymbol{\gamma}$ (%) (a) before and (b) the flow measurements for 2.5% wt. Microgel2000-10.

Similarly, in Figure 2-30, we plot the extrapolated apparent shear viscosity at shear rate= 1 s^{-1} for various concentrations of Microgel2000-10. We clealy see that in all the concentrations, the viscosity increases in the decrementing steps (refer to Table 2-11). A similar trend is observed for the G' values of all concentrations (Figure 2-31). This change/increase is due to the state of the suspension being changed as a results of the formation of the aggregates on application of high shear. We speculate that these aggregates can evolve into larger clusters eventually forming a gelled mass provided the shear rates and time of action is sufficient enough and will be reflected in the macroscopic flow behaviour.

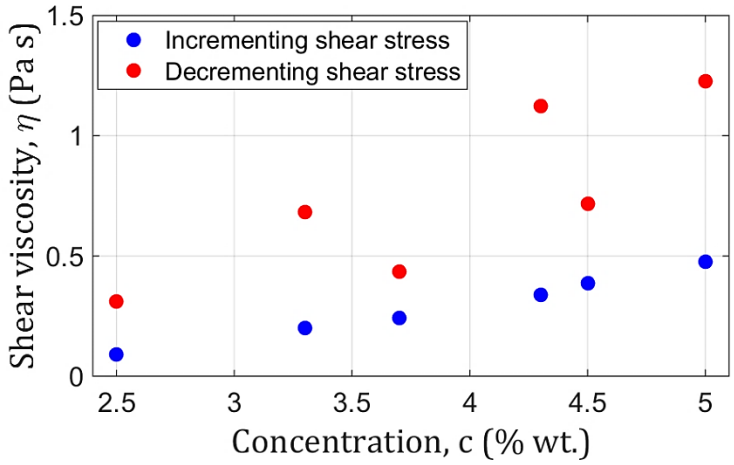

Figure 2-30 Plot showing the change in apparent shear viscosity calculated using the power law and Herschel-Bulkley coefficients at 1 s^{-1} shear rate for incrementing and decrementing shear stress steps for various concentrations of Microgel2000-10.

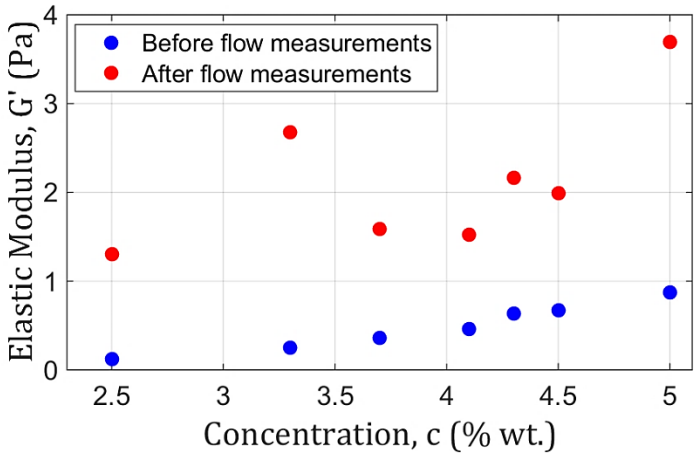

Figure 2-31 Plot of the values of elastic modulus, G' (Pa) measured from the linear viscoelastic regime (LVR) before and after the flow measurements for various concentrations of Microgel2000-10.

Table 2-11 Table summarizing the percentage increase in the values of elastic modulus as measured after the flow measurements and in the apparent shear viscosity calculated at shear rate 1 s^{-1} using power law parameters in both incrementing and decrementing shear stress steps along with the maximum shear rates applied in each flow measurements.

Concentration, c (% wt.)	Maximum shear applied (s^{-1})	$\Delta G'$	$\Delta \eta$
2.5	647	1008.7 ↑	237.6 ↑
3.3	606	974.6 ↑	240 ↑
3.7	168	336.2 ↑	79.8 ↑
4.1	114	232.6 ↑	17 ↑
4.3	76	242.4 ↑	231.2 ↑
4.5	77	195.9 ↑	85.4 ↑
5	542	321.5 ↑	158.5 ↑

2.6 Conclusions and Perspectives

In this chapter, we investigated the particle size distribution and the rheology of the microgel suspensions of various concentrations. In terms of the particle size, our results show that the centrifugation technique works relatively better than ultra-turraxing, in controlling the size of the particles and it yields a narrower particle size distribution as compared to the highly polydispersed Microgel-IN. Centrifugation worked best by getting rid of the bigger particles without destroying them. We then show a method to successfully prepare higher concentrations of the centrifuged suspensions without damaging their structure. The particle size distribution results of higher concentrations of the centrifuged microgel suspensions revealed that the suspensions start forming aggregates at concentrations, >2 % wt. The concentration dependency of the rheological behaviour of the microgel suspensions was investigated. The suspensions were found to be shear thinning which become more prominent at higher concentration. We find that the Microgel4000-10, Microgel2000-10 and Microgel-IN are very well described by power law model for concentration 0.3% to 6% wt., 0.4% to 5% wt. and 0.8% to 3.3% wt. respectively. However, the suspension deviates from the power law behaviour and starts to show a yield stress at higher concentrations. The presence of yield stress in the suspension indicates that the suspension is transitioning towards the jamming regime. The results of the particle size distribution for higher concentration were found to be consistent with the flow behaviour of the suspensions. We showed the invalidity of the Krieger-Dougherty fit for the relative viscosity versus concentration

in our system and explained it in terms of the shape of the particle which is not perfectly spherical. It is this elongated shape of the particles which is likely to be responsible for the viscosity plateau between 2-7% wt. that was observed in the relative viscosity versus concentration curve. We roughly estimated the particle volume fraction for Microgel4000-10 and Microgel2000-10 using the jamming concentration and maximum concentration. The value at the transition to a yield stress fluid behaviour was estimated to be 0.62 and 0.57 for Microgel4000-10 and Microgel2000-10 respectively. The oscillatory measurements showed that the centrifuged suspensions were predominantly viscous with $G'' > G'$ for most concentrations. However, Microgel-IN becomes more elastic (i.e. $G' > G''$) at a lower concentration of 3.3% wt. mainly due to the tightly packed and deformed particles. We show the interesting phenomenon of shear induced aggregation in Microgel2000-10, with the help of oscillatory and flow measurements performed before and after the application of very high shear. We observed a rise in the shear viscosity and an increased shear modulus after applyling high shear rates. The increase in the values depends on the concentration used and the value of the shear rate applied. We need to investigate this phenomenon further in a more systematic manner to fully understand this.

Chapter 3

Drying of Microgel suspensions

Table of Contents

Chapter 3 Drying of Microgel suspensions

3.1 Research Objectives

The goal of this chapter is to characterize the particle-surface interaction and to determine the best suited surface (in terms of hydrophobicity or hydrophilicity) for good adhesion of Microgel suspensions and to see whether one can get an estimate of the jamming volume fraction by simply sucking water out from the microgel. We perform drying experiments in a confined cell to investigate how Microgel4000-10 and Microgel2000-10 of initial concentrations, c_i = 1.2% wt. interact with hydrophobic and hydrophilic surface respectively. We also estimate the c_j (% wt.) by observing the intensity drop within the droplet due to air invasion between the particles as the solvent escapes the droplet. The effect of confinement on the jamming concentration of the suspension is also studied.

3.2 Background

The drying of a liquid droplet with solute on a substrate is a most challenging and intricate phenomenon on account of the natural morphologies it takes. It has important applications ranging from ink-jet printing, medical diagnostics, coating to food engineering etc. (Alexander, 2013; Tirumkudulu & Russel, 2005). The most basic case is the drying of sessile droplets in air at room temperature which has been studied extensively by researchers and has given a wealth of information about the drying phenomenon. Deegan et al., using a simple experiment extensively studied the complex mechanism for the deposition of the solute near the contact line (Deegan et al., 1997). Despite this, the problem still is largely unexplored and needs further studies because of complexities such as pinning of the contact line, out-of-equilibrium processes, divergence of the evaporation flux, convection/diffusion, thermally induced Marangoni flows (Cazabat & Guéna, 2010). On top of this, it is a pretty difficult task to tune the drying kinetics, hard to control the boundary conditions and difficult to observe. The solution to these problems can be solved by using a drying setup that provides well defined boundary conditions: confined geometries. Confined drying provides an axial symmetry that allows a neat removal of the vapours from the droplet towards the edge of the wafer (Clément & Leng, 2004). The drying kinetics can also be tuned by changing the size of the substrate as the confinement controls the evaporation process. This quasi- 2D geometry also allows easy observation of the drying process over a course of time and the effect of the surface properties can also be studied quite easily by monitoring the

evolution of the droplet area, A(t), temporally. The average concentration, $\langle c(t) \rangle$ of the suspension at any time during the course of drying can also be easily evaluated.

$$\langle c(t) \rangle = \frac{c_i A_0}{A(t)} \quad \text{(3-a)}$$

Where, c_i is the initial concentration of the suspension at time, t=0, A_0 is the initial area of the confined droplet at time, t=0 and $A(t)$ is the area of the confined droplet at any time, t. The diffusion coefficient of the gas as it escapes the droplet is given as

$$\widetilde{D} = \frac{A_s}{4\pi \tau_e} \quad \text{(3-b)}$$

This equation takes into account the density balance beween the solvent and the vapour. Here, $A_s$is the are of the substrate and τ_e is the evaporation time (Leng, 2010).

3.3 Experimental Procedure

3.3.1 Set up for confined drying

In the experiments, we used droplets of microgel suspension (volume 0.2-0.7µl) of initial concentration, c_i = 0.7% -0.73% wt. and 1.2% - 1.34 % wt. These droplets are squeezed between two circular glass wafers of radii R_w= 3.8 cm (Figure 3-1). The inner facing side of the glass wafers were spin coated with poly (dimethylsiloxane) (PDMS, Sylgard 184, The Dow Chemicals) of thickness ~30 µm. This thin layer of PDMS offers a hydrophobic environment to the droplet and avoids any unnecessary line pinning and other complex phenomenon. The distance between the glass wafers is controlled by using two different PDMS spacers of thickness, h= 70µm and 250 µm. These spacers are placed at the edge of the glass wafers. The experiments were performed at room temperature (T= 21°C). The external humidity is measured using a hygrometer. The value was measured to be in the range of 45-47%.

Figure 3-1 Schematic view of the confined cell for drying of the droplet

The images to see the course of drying were taken using standard bright field and phase contrast microscopy (Olympus IX 51). For bright field microscopy, we used a 2X objective and for phase contrast we used a 4X PhC (refer to section 1.3.5). The images were collected using a CCD camera (Hamamatsu, OrcaFlash2.8). The framerate was set differently for different experiments (usually 0.1-1 fps).

3.4 Image Processing

The image processing is done to extract the basic parameter i.e. the area of the droplet, $A(t)$, as a function of time was performed using MATLAB. The MATLAB function for thresholding was exploited to detect the meniscus which is comparatively darker than the rest. Bright field images were used as they have a sharp contrast for the meniscus and the individual particles are not seen, hence they get ignored in thresholding.

3.5 Results and Discussion

3.5.1 Inhomogeneous Drying: Confined droplet

I. Particle-Surface Interaction

We perfomed confined drying experiments with dilute suspensions of Microgel-IN, Microgel2000-10 and Microgel4000-10 on PDMS coated substrates with different wettabilities. We used cured PDMS coated glass slides (thickness = 1mm) with a wetting contact angle of 118° and chemically

treated PDMS surfaces with a wetting contact angle less than 4°. The chemical treatment is done using a surface modifying agent (refer to section 1.3.6).

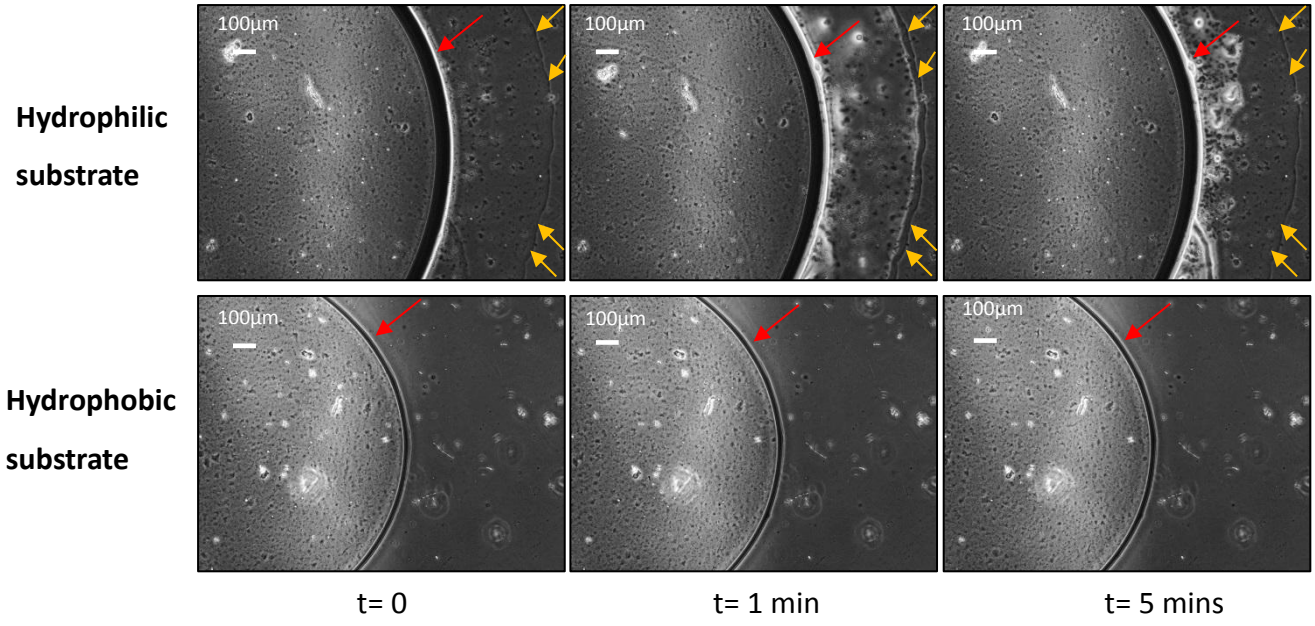

Figure 3-2 Phase contrast imagess of 0.7% of Microgel4000-10 on hydrohillic and hydrophobic surface at different times. The red arrow shows the receding meniscus and the yellow arrow shows the surface wetting by the receding meniscus of the microgel suspension.

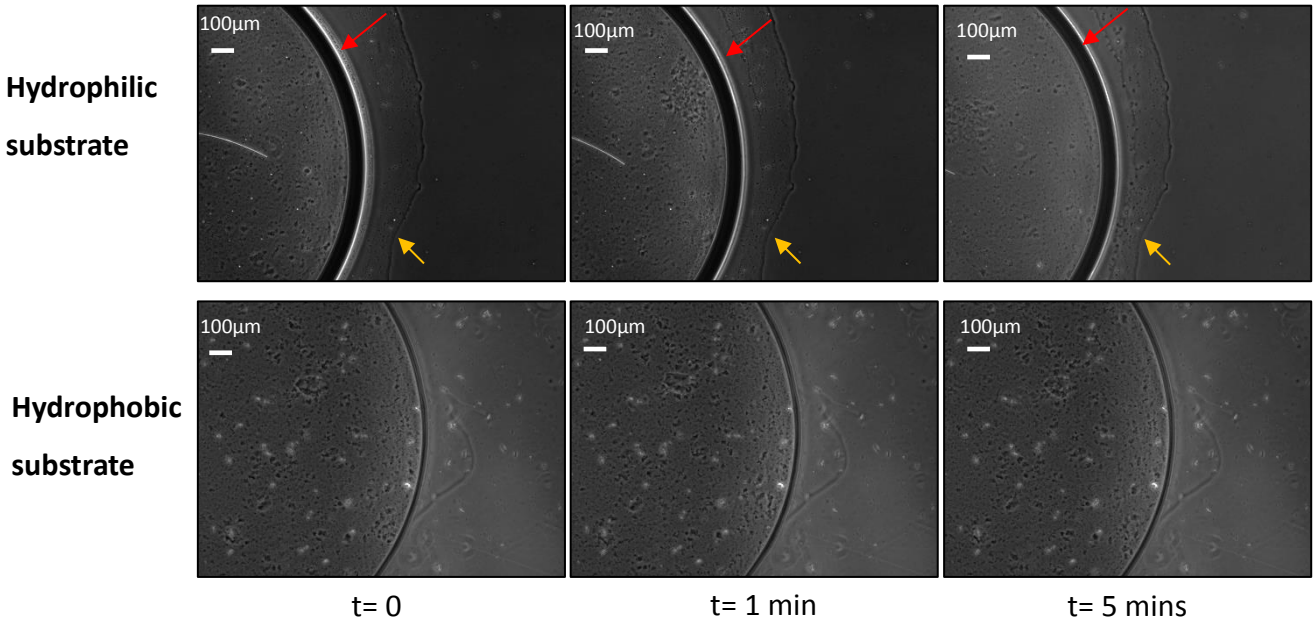

Figure 3-3 Phase contrast images of 0.7% of Microgel2000-10 on hydrohillic and hydrophobic surface at different times. The red arrow shows the receding meniscus and the yellow arrow shows the surface wetting by the suspension.

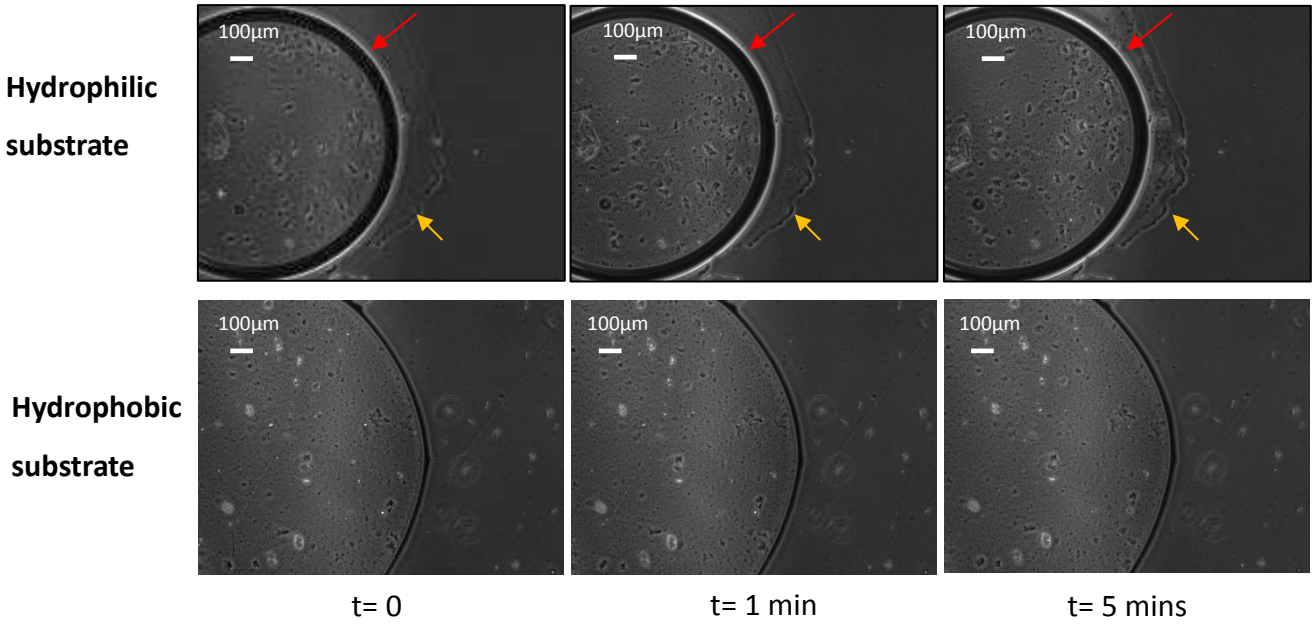

Figure 3-4 Phase contrast images of 0.72% of Microgel-IN on hydrohillic and hydrophobic surface at different times. The red arrow shows the receding meniscus and the yellow arrow shows the surface wetting by the suspension.

It can be clearly seen from Figure 3-2, 3-3 & 3-4, the thin layer (near the yellow arrows) of suspension as soon as the droplet rests on the hydrophilic surface while no such layer is seen on the hydrophobic surface. This thin layer stays and eventually dries up as the experiment proceeds. Moreover, particles are deposited on the surface as the meniscus is receding, which tell that the microgels have great affinity for hydrophilic surfaces. Even for concentrations as low as 0.7% wt., the suspension sticks to hydrophilic surface. This behaviour is not observed for the same concentration on hydrophobic surface. For hydrophobic surfaces, we observe that the meniscus is well defined and recedes without leaving any traces of particles on the surface

II. Jamming concentration

The experiments were performed using a hydrophobic PDMS (Sylgard 184, WCA= 120°) in order to avoid particle loss during the drying. We use initial concentration, c_i= 0.7-0.73% wt. and 1.2-1.3 % wt. of Microgel2000-10 and Microgel4000-10 with PDMS spacer thickness 70 µm and 250

μm. The bright field snapshots show that the temporal evolution of drying of a droplet of microgel suspension in the cell are shown below.

A. h=70 μm

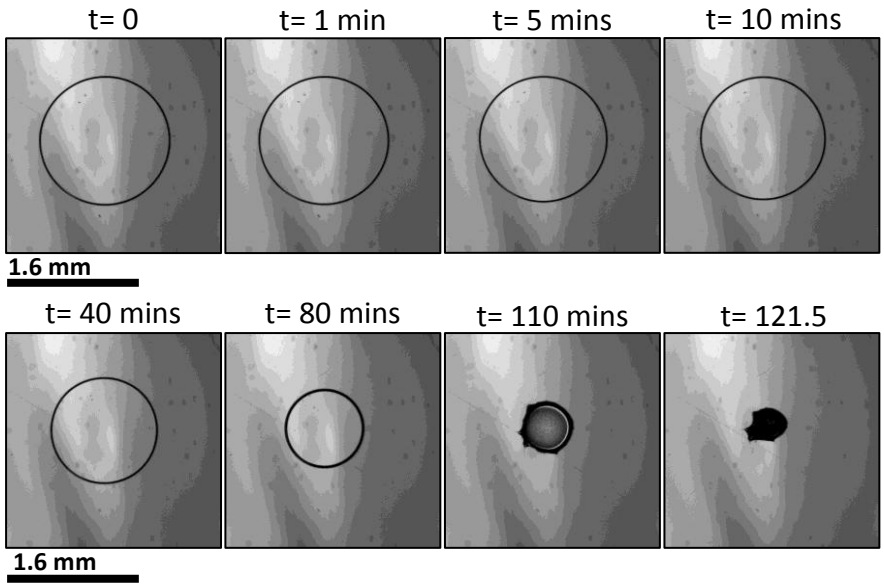

Figure 3-5 Series of bright field images demonstrating the confined drying of a droplet (~μl) of Microgel4000-10 of initial concentration, c_i = 1.2% wt. squeezed between two hydrophobic circular glass wafers (R_w= 3.8 cms) with a 70μm thick PDMS spacer.

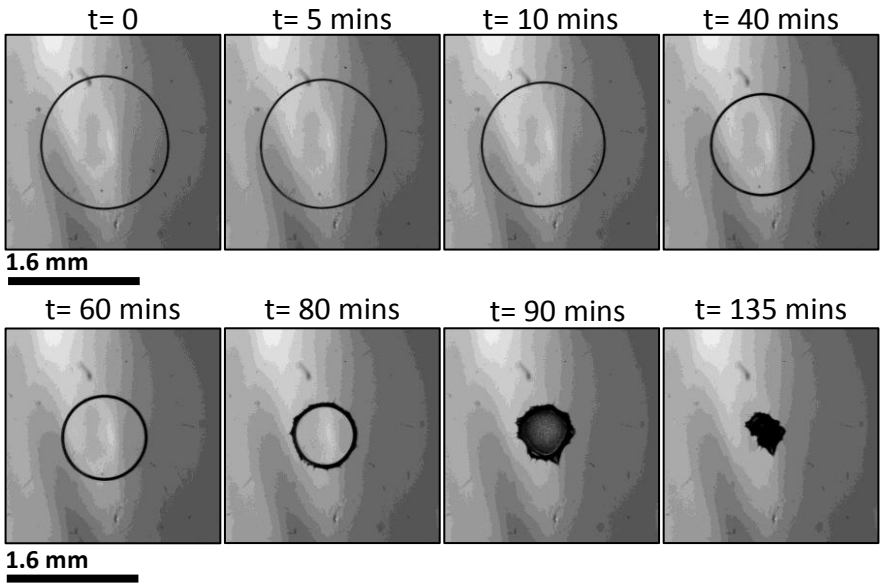

Figure 3-6 Bright field images depicting the confined drying of a droplet of Microgel2000-10 of initial concentration, c_i = 1.34% wt. squeezed between two hydrophobic PDMS coated glass wafers (R_w= 3.8 cms) separated by a 70µm thick glass wafer.

B. h=250 µm

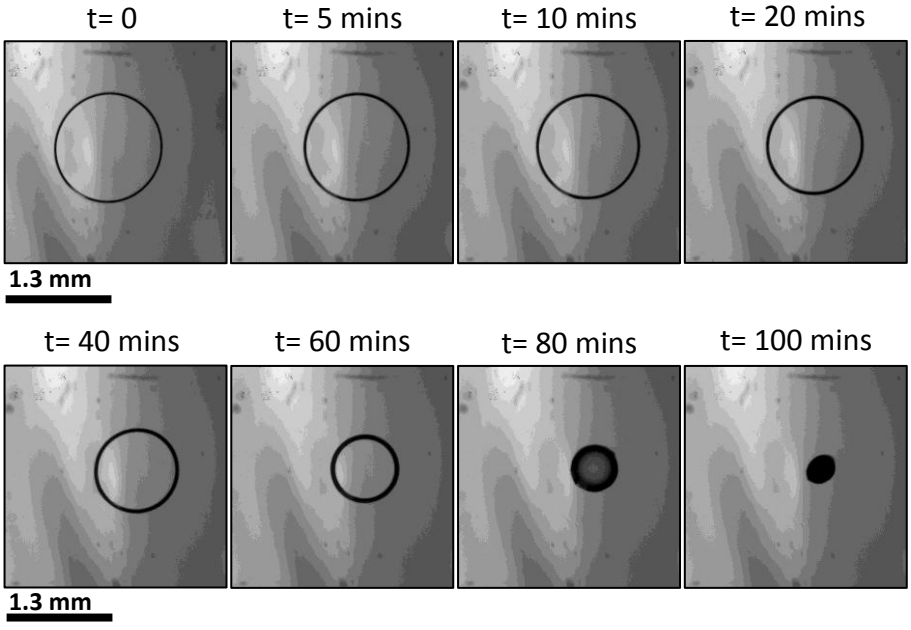

Figure 3-7 Bright field images depicting the confined drying of a droplet of Microgel4000-10 of initial concentration, c_i = 1.34% wt. squeezed between two hydrophobic PDMS coated glass wafers separated by a 250µm thick glass wafer.

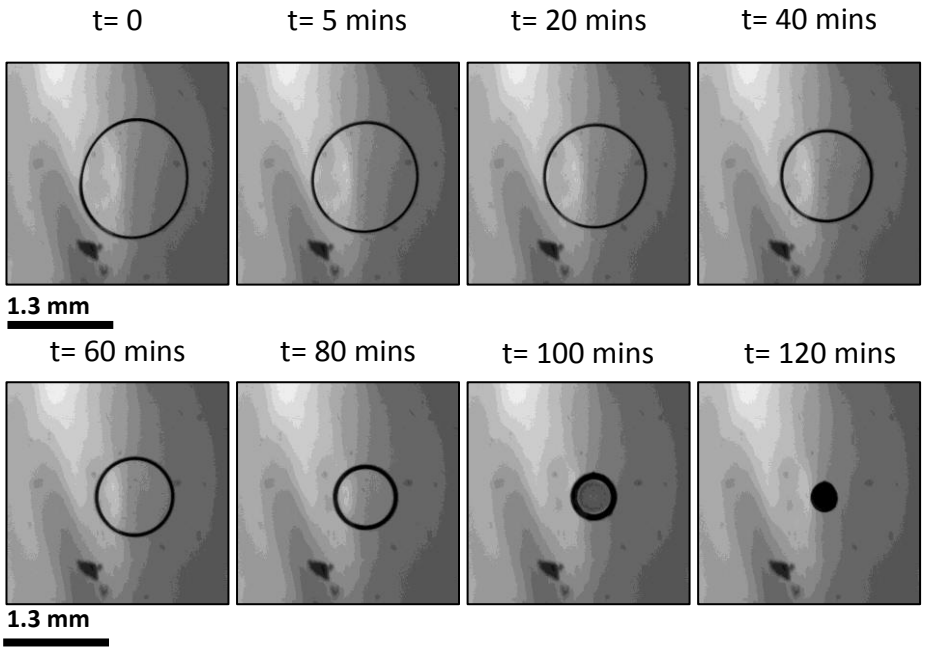

Figure 3-8 Bright field images depicting the confined drying of a droplet of Microgel2000-10 of initial concentration, c_i= 1.34% wt. squeezed between two hydrophobic PDMS coated glass wafers separated by a 250µm thick glass wafer.

Figure 3-5, 3-6, 3-7 and 3-8 above display the detailed brightfield snapshots of the temporal evolution of the microgel suspension undergoing confined drying in the cell with 2 different gaps, h= 70 & 250 µm. By just looking at the snapshots, we can say that the droplet (with initial concentration, c_i) assumes a perfectly cylindrical geometry inside the cell. As the solvent evaporates from the droplet edges with time, it is observed that the droplet is no longer perfectly circular due to the pinning of the meniscus. Another interesting effect observed in the drying experiments is the marked change in the intensity or rather a drop in the intensity locally within the drop at one point during the drying process and it seen to continue decreasing till the end of drying.

We try to further exploit this visible change in the intensity using MATLAB image acquisition tool. This intensity is the mean value of all the intensity values of the pixels in a defined region of interest in the grayscale image. We plotted the temporal evolution of the change in the intensity distribution in a well defined region of interest inside the droplet. First, consider the case of 1.34% wt. Microgel2000-10 where we see that the intensity before 5170 s remains almost constant with time. However after 5170s, a sudden drop in intensity is observed. We speculate that this time at

which the intensity drops is the jamming time, t_j which corresponds to jamming concentration, cj. The change in the intensity becomes more and more pronounced after t_j (see images on right in Figure 3-9, the whole process can be better seen in a videograph). This change happens due to the invasion of the air between the microgel particles as the solvent escapes out. As this invasion takes place, the region turns more and more dark and eventually it becomes black due to the mismatch in the refractive index between the very closely packed microgel particles. The intensity drop is a sign that the suspension is approaching the jamming transition as the particles are close to each other. At this jamming concentration (c_j), the rheology changes drastically from the dilute regime, the suspension turns predominantly elastic and starts yielding which explains the departure from the circular shape. We determine the jamming concentration, c_j (% wt.) from the average concentration versus time plot at t_j.

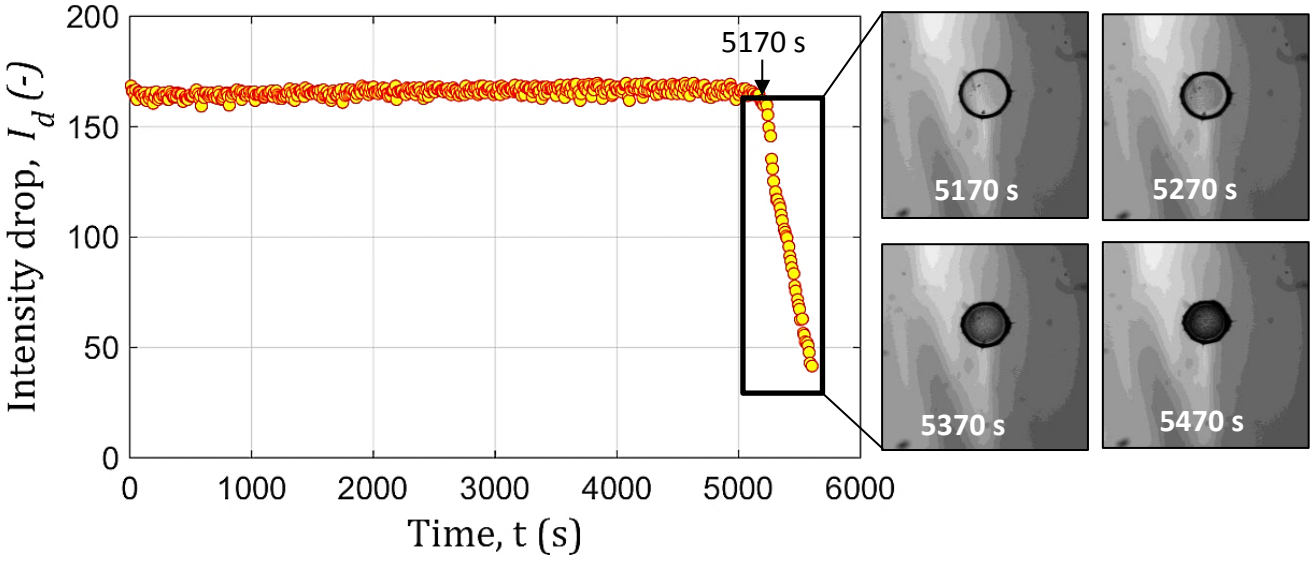

Figure 3-9 Plot of the drop in intensity inside the droplet as a function of time during the drying of Microgel2000-10 of initial concentration, c_i= 1.34% wt.

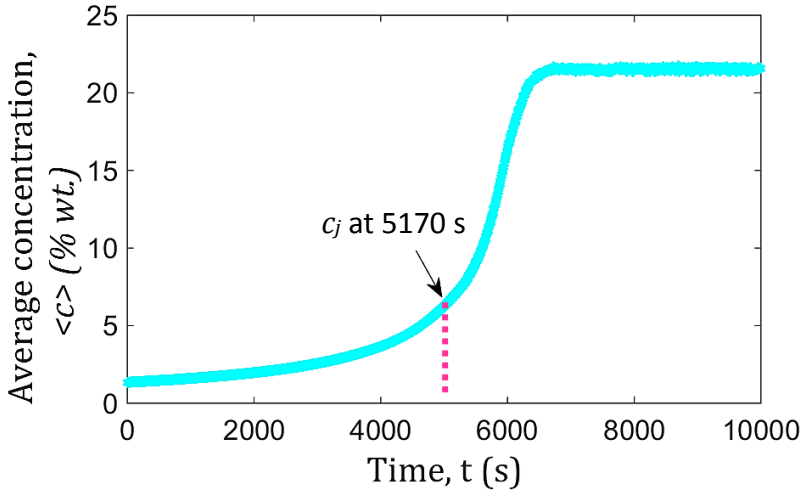

Figure 3-10 Evolution of average concentration of the drop of Microgel2000-10 of initial concentration, c_i= 1.34% wt. confned in a cell with a gap= 70 µm.

The jamming concentration (which is an average concentration at that time) comes out to be 6.78 ± 0.17 % wt. for Microgel2000-10 (see Figure 3-10). Similarly, for Microgel4000-10, we observed the intensity drop within the droplet to happen at c_j = 6.86 ± 0.22 % wt. Note: the values of c are not accurate since there is a stronger departure from circularity of the drop as the concentration increases, which makes the surface measurement difficult. Nevertheless, the values of c_j are rather well characterized and appear to be in reasonable agreement with the values obtained from bulk rheology (see Figure 3-11).

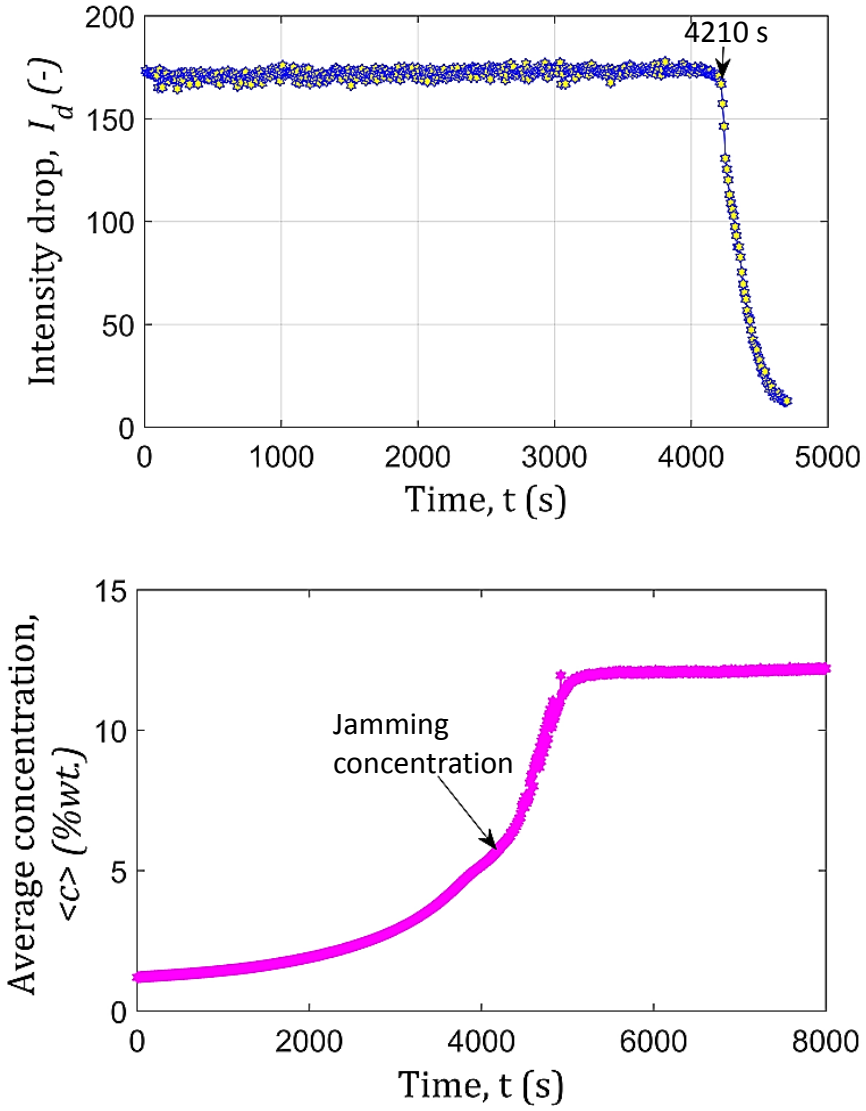

Figure 3-11 Intensity drop and evolution of average concentration of the drop of Microgel4000-10 of initial concentration, c_i= 1.34% wt. confined in a cell with a gap= 70 µm.

We tried further drying experiments to get an estimate of the jamming concentration by varying parameters like initial concentration and gap between the glass wafers. It was found that for a gap, h=70 µm, for 0.73% wt. of Microgel4000-10 and 0.72%wt. of Microgel2000-10, c_j was found to be 6.6 ± 0.12% wt. and 6.58 ± 0.03 % wt. respectively. Similarly, for initial concentration, c_i = 1.2-1.34% with gap, h= 250 µm, c_j was found to be 6.3 ± 0.1 % wt. and 6.2 ± 0.06 % wt. for Microgel2000-10 and Microgel4000-10. respectively. Clearly, jamming concentration seems to be affected only marginally by the initial concentration of the suspension used and by the gap between the wafer. This turns out to be a rather important result when considering the flow of

suspensions in micron sized channel and porous media. Here, one can easily say that confinement does not significantly affect the jamming concentration, at least for the range of sample thicknesses investigated.

3.6 Conclusions and Perspectives

In this chapter we show two important results in terms of the particle-surface interactions and the effect of confinement on the jamming concentration. We first discussed how the microgel suspension has more affinity for a hydrophilic surface as opposed to a hydrophobic surface. This result comes out to be a rather important one considering the use of microgel suspensions as a fluid loss control additive in rock formations (which are inherently hydrophilic) in a well bore. We then show an easy way to determine the jamming concentration of Microgel4000-10 and Microgel2000-10 with the help of confined drying experiments. We demonstrate with the aid of bright field microscopy, the invasion of air between the individual particles of the suspension as the solvent escapes the droplet and the suspension reaches the jamming limit and this is concomitant with the departure from the circular shape of the droplet as the suspension enters the yield stress fluid regime. The jamming concentration was found to be around 6.8% wt. for both Microgel2000-10 and Microgel4000-10 and it agrees to a certain limit with the results obtained from bulk rheology. However, the jamming seemed to be affected marginally when the gap between the wafers is increased. This marginal change is believed to be due to some confinement effects and needs further investigation.

Chapter 4

Flow through Porous Media

Table of Contents

Chapter 4 Flow through Porous Media

4.1 Research Objectives

The main objective of this chapter is to characterize and understand the jamming of soft dilute microgel suspensions (Microgel2000-10) whose rheology is very well described by the power law behaviour, in model porous media and to determine the parameters that significantly affect the jamming. We developed porous media made of PDMS elastomer that allows us to directly observe the jamming dynamics of the dilute suspensions in microchannels for frontal and lateral filtration with a well defined pore size (= 20 x 20 μm^2 and 40 x 40 μm^2). We also investigate how the rheology of the same particles changes when flowed through linear channels of varied dimensions. The critical conditions in terms of concentration, pore size and flowrates that affect jamming in porous media for frontal filtration have been identified in this chapter. We also demonstrate fluid loss control in porous media for lateral filtration in terms of building of the filter cake leading to a drop in flowrate in the porous material.

4.2 Background

A porous medium consists of solid materials permeated by a network of interconnected voids (Berejnov, Djilali, & Sinton, 2008). Filtration of microparticles in porous media is a challenging task and is relevant in a wide range of engineering applications. One of the most relevant applications is in oil extraction which involves the removal of the oil phase from the porous rock formations by the injection of an immiscible liquid. Among other important applications are geo-sequestration of CO_2, filtration of suspensions in polymer solutions and flows in soil. In context of non-Newtonian fluids, several studies have been done extensively over the past 50 years for the flow of viscoelastic fluids in packed beds. For viscoelastic fluids, it was observed that the experimentally measured pressure drop varied greatly from the predicted values in porous media (Marshall & Metzner, 1967; Sadowski & Bird, 1965; Savins, 1969). This led to futher investigations that revealed a marked increase in the resistance of the viscoelastic fluids due to the elongational flows in porous media (Bird, 2010; James & McLaren, 2006; Kulicke & Haas, 1984). However, the flow of non-Newtonian fluids through porous media is still far from being fully understood because each porous medium is itself unique owing to its morphology due to varied geometries which leads to several complex issues in defining the flow conditions inside the porous medium. Another complexity is in regards with the combination of shear and elongational flows with a very

strong shear flow near the walls and a strong elongational flow away from the walls as a result of the converging and diverging nature of the porous media. To tackle these issues, different porous media analogues have been used ranging from sand beds and packed sphere, alandrum plugs, sintered glasses to compressed glass wool to fully understand the flow dynamics in porous media but it again turned out to be a rather complex task. One being the direct visualization of the complex processes taking place inside the porous media due to the opacity of the solid matrix. Futhermore, numerical simulations too at the pore scale are expensive due to computational resources (Litster, Sinton, & Djilali, 2006). Later, experimentalists started employing more ordered porous media fabricated by glass micromachining (Ferer et al., 2004) or hydrophilic etching (Perrin, Tardy, Sorbie, & Crawshaw, 2006) or lyophilic lithography fabricated polymer structures. These ordered fluidic networks were found to have more advantages in terms of direct visualization of the complex processes taking place inside the porous media. These ordered fluidic networks made it far easier to distinguish between the two phases of the fluids used via bright field microscopy only. Early works by Wyss *et al*., showed that model microfluidic porous media provides a good way to study the flow of particles at micrometer scales. In their work, they demonstrated the phenomenon of clogging of aqueous suspensions of uniform polystyrene spheres at single pore level (Wyss, Blair, Morris, Stone, & Weitz, 2006). Another work by M D Haw published in 2004, focussed on both experimental and theoretical investigation of the flow of concentrated suspensions of polymethyl-methacrylate (PMMA) spheres through constrictions by pressure gradient which lead to what is called as “jamming” (D Haw, 2004). Jamming is described as the conversion of the liquid like system to a solid like system by the application of stress. The work demonstrates quantitatively, the jamming of concentrated suspensions in convergent flow leading to what they called “self filtration”. They thoroughly studied the effect of tapering on the volume fraction of the suspensions extracted through the taper and compared it with the volume fraction of the bulk sample.

The work done in this chapter is in light with the previous work on microfluidic porous media and exploiting the jamming property of dilute microgel suspensions in porous media in context with the applications related to the oil industry in the form of fluid loss additives. Each void in the porous media acts as a capillary or slit rheometer. These capillary rheometer provide very high

shear rates and the measuremnt is relatively easy. For the flow of Newtonian fluids through rectangular ducts, the typical Hagen Poisseille law describes the pressure drop versus flowrate relation (Equation 4-a) and the viscosity is easily calculated using the shear stress and shear rate dependence.

$$\Delta P = R_h\, Q \tag{4-a}$$

Here, Q is the volumetric flowrate, ΔP is the pressure drop along the channel and R_h is the hydrodynamic resistance (Fuerstman et al., 2007) given as

$$R_h = 12\left[1 - \frac{192\,H}{\pi^5\,W}\,\tanh\left(\frac{\pi\,W}{2H}\right)\right]^{-1}\;\frac{\eta L}{W\,H^3} \tag{4-b}$$

However, the flow of non-Newtonian fluid through ducts is more complex. It has already been investigated that for the case of slit die with H/W nearly zero (where H is the height and W is the width of the duct/die), it is easy to calculate shear rates and wall stresses as the theoretical calculations are based on the assumption that the velocity is independent of the lateral position. However, for a rectangular duct with H/W is nearly 1, estimating the exact values of the shear rate is not possible from the volumetric flowrate data and the pressure gradient. However, Son in 2006, proposed an explicit relationship to get the exact shear rate dependence on shear stress from the flow data in a rectangular duct. Hartnett and Kostic in their work on rectangular ducts, obtained an expression by numerical calculation for wall stresses for the flow of power law fluids with power law index (n) and consistency factor (k) (Hartnett & Kostic, 1989). The apparent shear rate and wall stress for rectangular ducts with H/W ranging from 0.1 to 1 is given as:

$$\dot{\gamma}_a = \left(\frac{6Q}{WH^2}\right)\left(1 + \frac{H}{W}\right) f^*\left(\frac{H}{W}\right) \tag{4-c}$$

$$\boldsymbol{\sigma_w = K\left[\dot{\gamma}_a\left(\frac{2}{3}\right)\left(\frac{b^*}{f^*} + \frac{a^*}{f^*}\,\frac{1}{n}\right)\right]^n} \tag{4-d}$$

And the wall shear rates (Son, 2007) in the rectangular ducts is given as

$$\dot{\gamma}_w = \dot{\gamma}_a \left(\frac{2}{3}\right)\left(\frac{b^*}{f^*} + \frac{a^*}{f^*}\frac{1}{n}\right) \tag{4-e}$$

where a*, b* and f* are functions that depend only on the duct aspect ratio (refer to Table 4-1)

Table 4-1 Geometric constants a*, b* and f* given for rectangular ducts (Hartnett & Kostic, 1989)

H/W	a^*	b^*	f^*
0.00	0.5000	1.0000	1.0000
0.05	0.4535	0.9513	0.9365
0.10	0.4132	0.9098	0.8820
0.15	0.3781	0.8745	0.8351
0.20	0.3475	0.8444	0.7946
0.25	0.3212	0.8183	0.7597
0.30	0.2991	0.7954	0.7297
0.35	0.2809	0.7750	0.7040
0.40	0.2659	0.7571	0.6820
0.45	0.2538	0.7414	0.6634
0.50	0.2439	0.7278	0.6478
0.55	0.2360	0.7163	0.6348
0.60	0.2297	0.7065	0.6242
0.65	0.2248	0.6985	0.6155
0.70	0.2208	0.6921	0.6085
0.75	0.2178	0.6870	0.6032
0.80	0.2155	0.6831	0.5991
0.85	0.2139	0.6803	0.5961
0.90	0.2129	0.6785	0.5942
0.95	0.2123	0.6774	0.5931
1.00	0.2121	0.6771	0.5928

While for a simple slit die with (W> H), the wall shear rate is expressed as follows:

$$\dot{\gamma}_w = \frac{2n+1}{3n}\dot{\gamma}_a \tag{4-f}$$

here, $\dot{\gamma}_a$ is the apparent shear for the slit die for volumetric flowrate, Q, and it is given as:

$$\dot{\gamma}_a = \frac{6Q}{WH^2} \tag{4-g}$$

4.3 Experimental Procedure

4.3.1 Material

We used a dilute 0.4% wt. Microgel2000-10 suspension for the flow experiments in linear rectangular channels and a 0.8% wt. Microgel2000-10 suspension for experiments in porous channel for frontal and lateral filtration. The preparation of this suspension from the stock Microgel-IN suspension is explained in section 1.3.1. Microgel2000-10 behaves as a power law fluid with the values of n = 0.97 and k= 2.9 x 10^{-3} Pa s^n for concentration 0.4% wt. and n=0.92 and k=6.33 x 10^{-3} Pa s^n for 0.8% wt. The light diffraction results of the particle size distribution gives a $d_{0.5}$= 27 µm (section 2.5.1).

4.3.2 Set up

The channels of various dimensions are fabricated using standard soft lithography of PDMS that involves casting and curing over Si master molds with the desired template design. The PDMS stamps and PDMS coated glass slides are oxidized in O_2 plasma and are sealed together irreversibly (Duffy et al., 1998). The Si master mold is fabricated by conventional photolithography using a negative photoresist (SU8 3050, 3035 Microchem). The standard procedures of the soft lithography and photolithography are explained in detail in section 1.3.6. All the oxidized PDMS channels are treated with the surface modifying agent to ensure that the surface wettability remains constant over a period of long period of time. The experiments in linear channels and porous media for frontal filtration were constant flow driven experiments while those in porous media for lateral filtration are driven at constant pressure. The differential pressure is measured along the channel for various flowrates using the setup explained in detail in section 1.3.7 while the flowrates are measured using a high precision Flow sensor (M-series, Fluigent).

I. Linear Channels

We used linear microfluidic channels (as shown in Figure 4-1) of total length, L_T = 2 cms with L= 1 cm (distance between the pressure probes) & L_1= L_2= 0.5 cm while the channel have different heights (H) and widths (W) (see Table 4-2 below). The experiments were constant flow driven

using a Harvard syringe pump (PHD2000, Harvard Instruments). We used 0.4% wt. Microgel2000-10 for the flow experiments. Two long tubings filled with water were connected to P_1 and P_2 each and the tubing's other ends were connected to the differential analog pressure transducer (100 Psi, Honeywell). Pressure drop, ΔP ($=P_2-P_1$) was measured across the channel using a pressure sensor (refer section 1.3.7 for details). The channel has a single outlet (Bin) which is maintained at atmospheric pressure (P_{atm}).

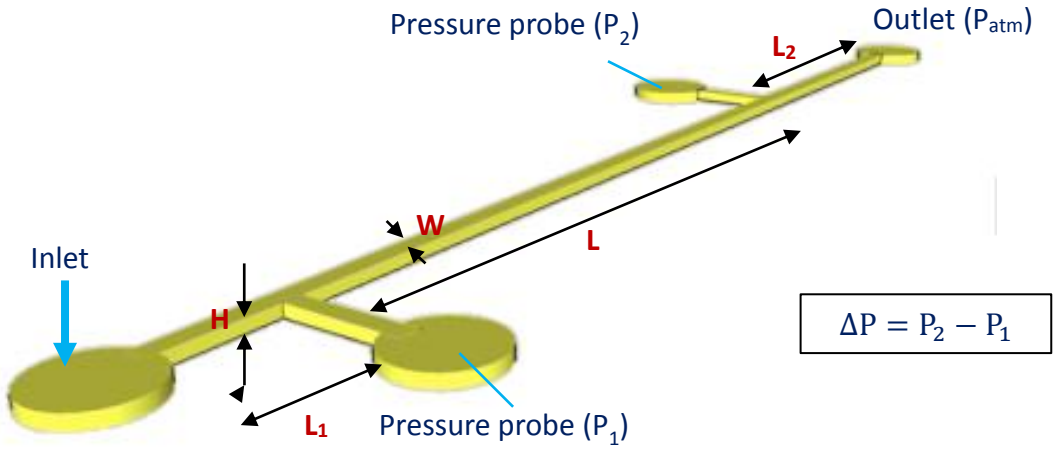

Figure 4-1 Schematic diagram of the Linear channel used in the study with Height (H), Width (W) and Length (L). Inlet on the left is for flow and outlet goes to bin maintained at atmospheric pressure. The pressure probe is connected at end P_1 and P_2.

Table 4-2 Table summarizing the dimensions and the aspect ratios of the Linear Microchannel A, B and C (*P is perimeter).

	Width, W (µm)	**Height, H** (µm)	**Aspect ratio (H/W)**	**Area of cross section, A** (μm^2)	**Characteristic length, 4A/P** (µm)
Channel A	20 µm	15 µm	0.75	300	17.15
Channel B	45 µm	30 µm	0.66	1350	36
Channel C	85 µm	60 µm	0.70	5100	70.35

II. Porous media- Frontal Filtration

The porous channels for frontal filtration consist of an array of elongated pillars of length, L= 200 µm (see Figure 4-2 and 4-3). These pillars are placed parallel to the direction of flow of the fluid (hence the name Frontal filtration) in the middle of a feed channel. We varied the width (w_p),

height (h) and the gap (w_g) between the elongated pillars forming the porous array (refer Table 4-3). The feed channel consists of two parts, Region A & B, situated before and after the porous array. The height and the width of the channel in Region A & B are kept at 120 and 470 µm respectively making the overall channel stepped. This is done to avoid any self filtration taking place before the suspension reaches the porous part. The same dimension of Region A and B was used for Frontal-20 and Frontal-40 channels. The pressure probes are connected at P_1 and P_2 and the flow is induced at the inlet. The outlet is connected to a bin which is kept at atmospheric pressure. All the experiments are performed at room temperature (21°C).

Table 4-3 Table showing the dimensions of the elongated pillars forming the porous array and the names given to the channels used for the flow experiments.

Width of the elongated pillar, w_p (µm)	**Gap between elongated pillars, w_g** (µm)	**Height of the elongated pillar, h** (µm)	**Name given**
20	20	20	Frontal-20
40	40	40	Frontal-40

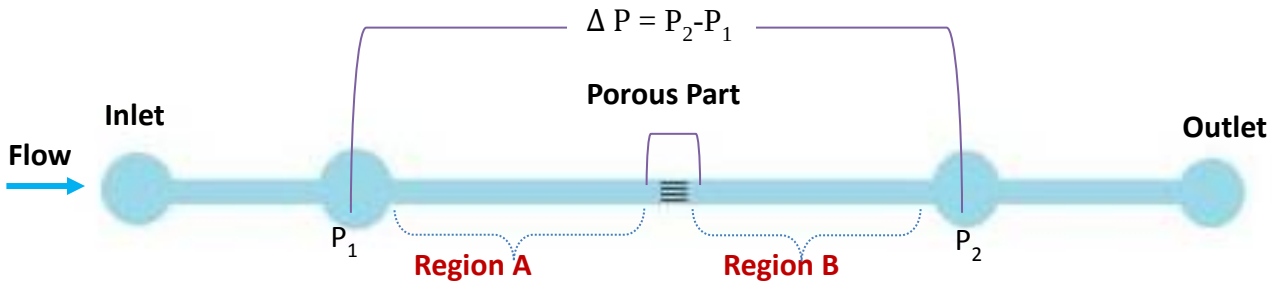

Figure 4-2 Diagram showing the top view of porous media for frontal filtration. The pressure probes are connected at P_1 and P_2. Fluid is flowed through the inlet. The outlet is connected to a bin maintained at atmospheric pressure.

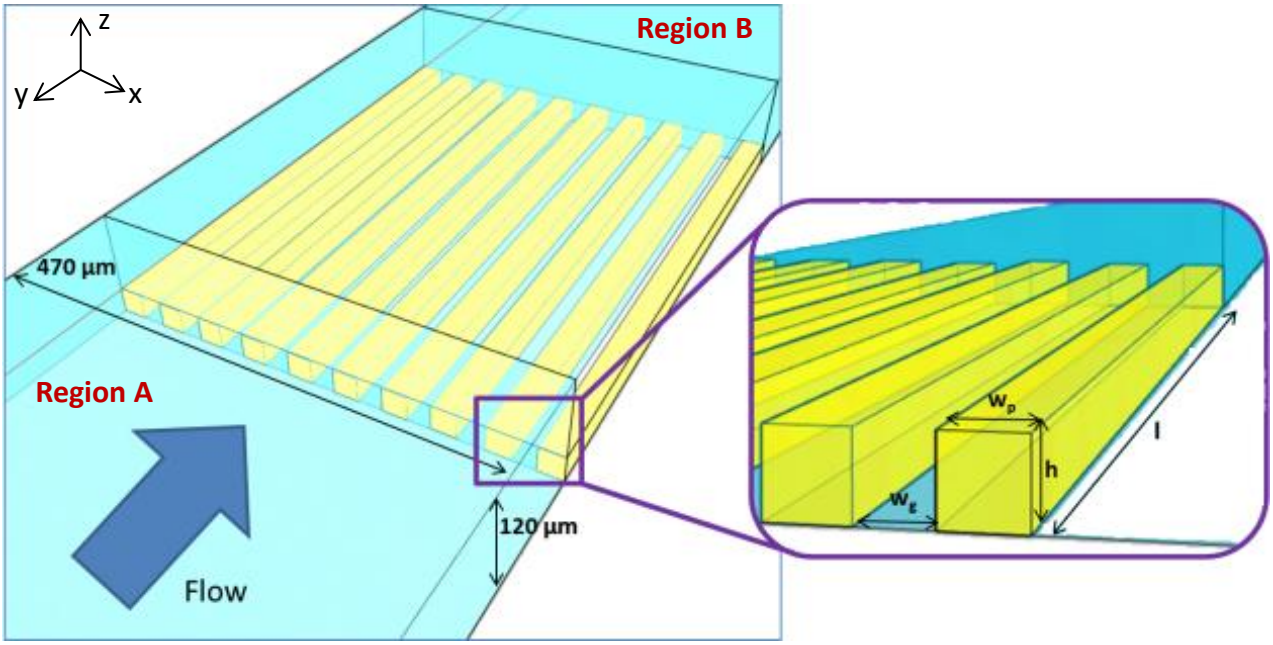

Figure 4-3 Pictorial representation of the porous channel for frontal filtration showing the porous array of elongated pillars forming the porous media for frontal filtration. The length of the pillar is 200µm. The height (h), width (w_p) and gap between the pillar (w_g).

III. Porous media- Lateral Filtration

The porous channels for lateral filtration are T shaped channels with the porous part situated at the junction of two arms. One arm constitutes the main feed channel of width = 470 µm and height = 180 µm and it connects the ends P_1 and P_2 (see Figure 4-4) . The porous part is made up of an array of elongated pillars that lie perpendicular to the feed channel. The pillars are followed by a lateral arm of width = 470 µm and height = 180 µm leading to an outlet P_3. The dimension of the elongated pillars are length, L =200 µm, height (h)= 20 µm, width (w_p)= 20 µm and gap between the pillars (w_g)= 20 µm (see Figure 4-5).

The experiments performed in porous channels for lateral filtration are constant pressure controlled experiments using Microfluidic Flow Control System (MFCS™, Fluigent) with a constant pressure ($P_1 > P_2 > P_3$) applied at all the three ends. The goal of using pressure control is to simulate fluid loss in the rock and to see if the flow towards the porous material can be stopped thanks to the microgel. We used pressurized air to control the pressure applied to the microgel

suspension. The pressurized air is sent to the fluid filled sample vial. As the pressure inside vial increases, it drives the fluid through the tubing into the microfluidic device. The values of the pressures used in the experiments are mentioned in Table 4-4.

Table 4-4 Table depicting the various values of pressure maintained at ends P_1, P_2 and P_3 with the help of MFCS in porous media for lateral filtration.

P_1 (mbar)	P_2 (mbar)	P_3 (mbar)
40	20	10
60	30	15
80	40	20
100	10	1

During the experiments, the flowrate is measured as a function of time in the lateral arm. A Flow sensor (M-series, Fluigent) is connected to end P_3 with the help of a long PFA tubing (~ 100 cms) with a water buffer column to avoid contamination of the flow sensor due to the microgel suspension. All the experiments were performed at room temperature (21°C). The experiments were done with de-ionised water first and then 0.8% wt. Microgel2000-10 to compare the measured flowrates in the lateral arm.

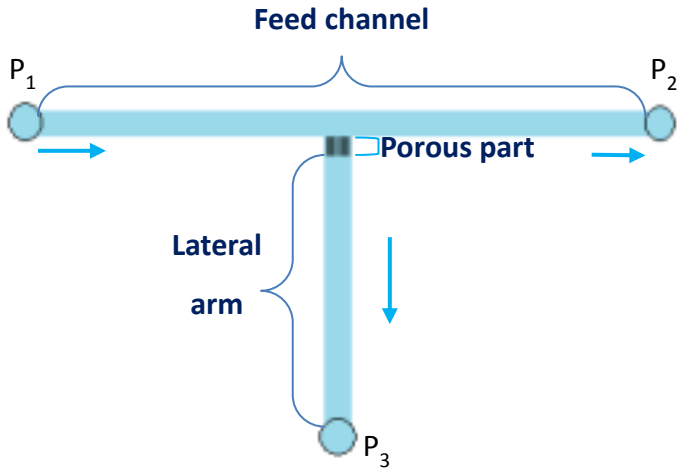

Figure 4-4 Diagramatic representation of the top view of the porous media for lateral filtration. The feed channel connects the ends P_1 and P_2. The lateral arm with end P_3 is joined to the feed channel via a porous array of elongated pillars (l x w_p x h) with gap (w_g).

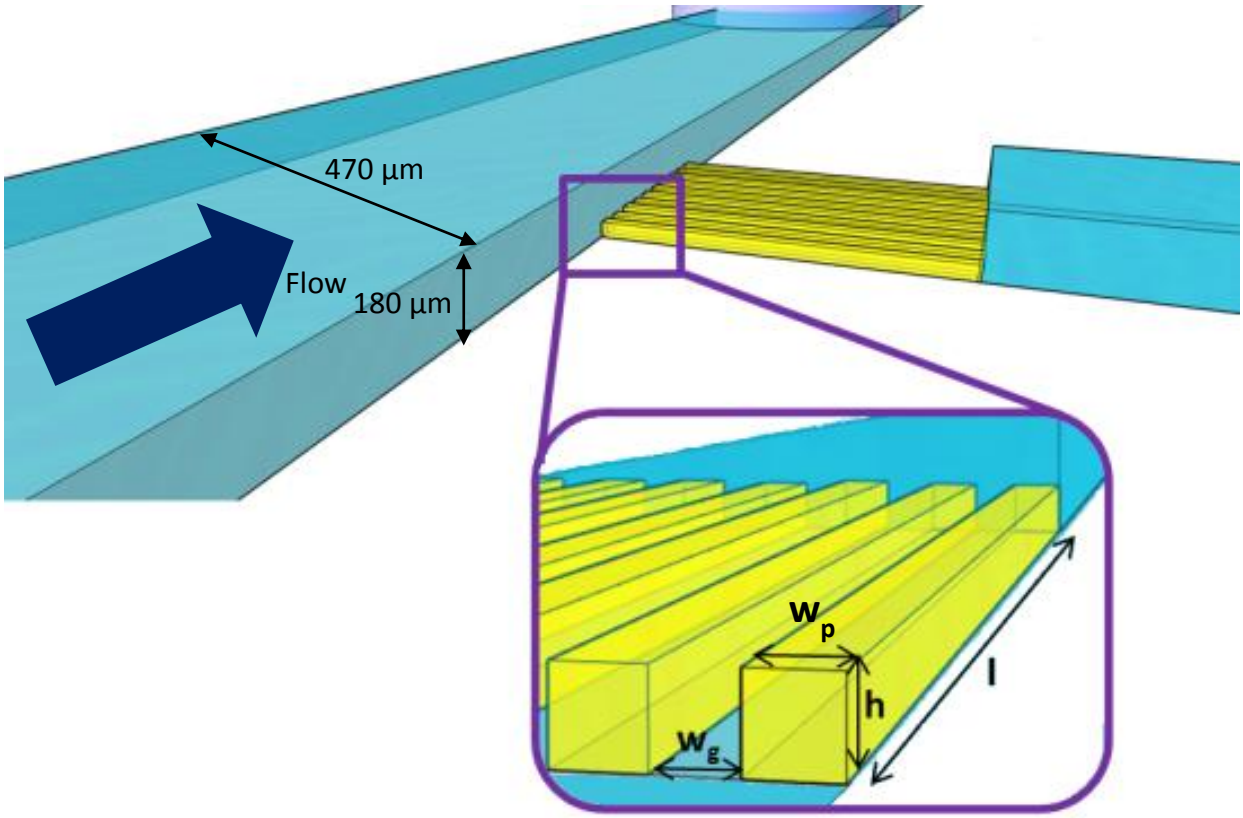

Figure 4-5 Pictorial representation of the side view of the porous media for lateral filtration with the dimensions of the porous elongated pillars, l x h x w_p and the gap between the pillar w_g. The feed channel connecting the end P_1 and P_2 have dimensions 470 µm x 180 µm.

4.3.3 Imaging

We used video phase contrast microscopy to record the images of the porous channels and observe the jamming dynamics of the microgel suspension. The optical setup consists of an inverted microscope (IX 51, Olympus) equipped with a CCD camera (Hamamatsu, OrcaFlash2.8). We also employed fluorescence microscopy with a light source (100W mercury lamp). For fluorescence visualizations, the suspensions were seeded with fluorescent tracers particles (Fluosphere®, Carboxylate 1µm, Life technologies). The seeded suspension flowing through the microfluidic porous media were illuminated by the UV light and the light reflected by the tracers was detected by the CCD camera. The exposure times were varied according to the flowrates used in the experiments.

4.4 Results and discussion

4.4.1 Flow through Linear Channels

We performed constant flowrate driven flow experiments in rectangular linear channels, namely Channel A, B & C (their dimensions are summarized in Table 4-2). In this section, we worked with different volumetric flowrates, Q= 100, 300, 500 and 800 µl/hr and measure the corresponding pressure drop across the channel.

For the case of Channel A, it was not possible to take multiple pressure data points for different volumetric flowrates for the flow of 0.4% wt. Microgel2000-10 as the pressure in the channel was high enough to saturate the pressure sensor owing the small dimensions of the channel. The $d_{0.5}$ =27 µm which is greater than the channel dimensions hence any particle that enter the channel must be deformed or in close contact with the walls. Hence, for Channel A, we only show the raw data of the temporal evolution of the pressure drop and the eventual steady state achieved for Q= 100µl/hr for the flow of 0.4% wt. Microgel2000-10 and water and compare the values to estimate the viscosity of the suspension while it is inside the channel.

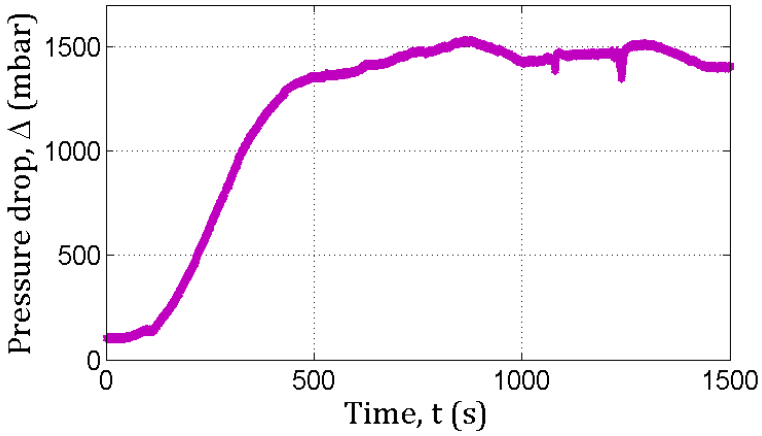

Figure 4-6 Raw data of the pressure drop across Channel A for the flow of 0.4% wt. Microgel2000-10 at a constant flowrate, Q=100 µl/hr.

The average pressure drop was found to be 1449 ± 45 mbars which gives the value of R_h as 14.49 mbar/(µl/hr) while for water, R_h was calculated as 1.78 mbar/(µl/hr). We estimate the viscosity of the suspension inside the channel using the fact that R_h is directly proportional to the viscosity (refer Equation 4-b). This gives the viscosity as 8.7mPa s which is more than triple the value we

get from bulk rheology i.e 2.42 mPa s for the same suspension. This high value of viscosity is a direct indication of the impact of finite size effects on the resistance. It might also be due to the aggregation of particles with each other because of their sticky nature. These results are of utmost relevance in filtration experiments with small channels where no jamming is expected to take place in the porous array. We now discuss the flow of 0.4% Microgel2000-10 in Channel B and Channel C. Figure 4-7 and 4-8 show the pressure drops inside Channel B and Channel C for corresponding flowrates respectively.

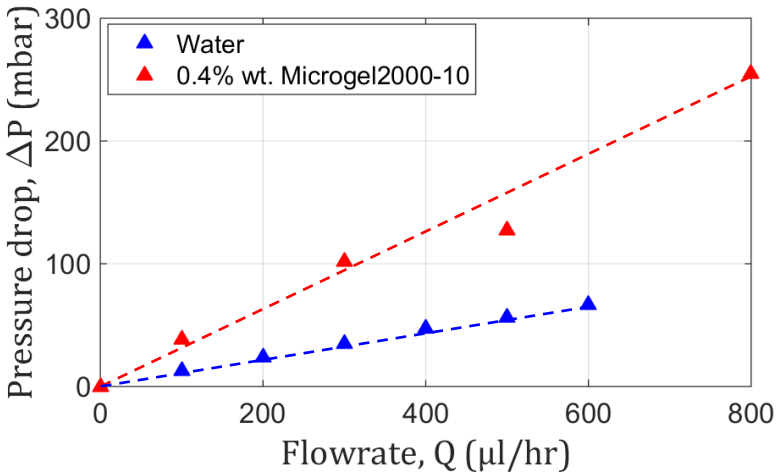

Figure 4-7 Pressure drop, ΔP as a function of flowrate, Q (µl/hr) for the flow of water and 0.4% wt. Microgel2000-10 through Channel B.

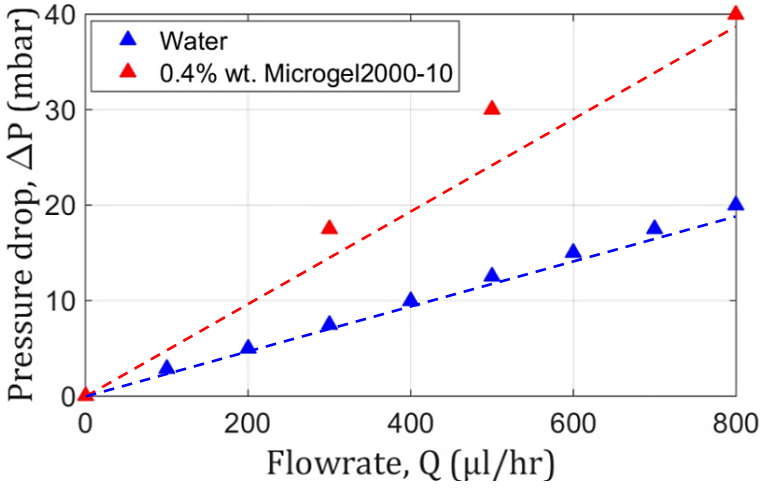

Figure 4-8 Pressure drop, ΔP as a function of flowrate, Q (µl/hr) for the flow of Water and 0.4% wt. Microgel2000-10 through Channel C.

The curves in Channel B and C look pretty linear indicating a pseudo-Newtonian behaviour of the suspension inside the channel. This linearity in the curve is also in agreement with the results

from the power law fit with coefficient, n > 0.9 for the concentration used in this experiment. For each channel, Height (H), Width (W) and Length (L) are constant so one can easily say from Equation 4-b that R_h (hydrodynamic resistance which is also the slope of the curve) is proportional to viscosity, η i.e.

$$\frac{R_h|_{Microgel}}{R_h|_{Water}} = \frac{Slope\,|_{Microgel}}{Slope\,|_{Water}} = \frac{\eta|_{Microgel}}{\eta|_{Water}} \tag{4-h}$$

The slopes of the curves for 0.4% wt. Microgel2000-10 in Channel B and C are 0.3052 mbar/(µl/hr) and 0.0533 mbar/(µl/hr) while for water, the values are found to be 0.1136 mbar/(µl/hr) and 0.025 mbar/(µl/hr). Using these values in Equation 4-h, we get the value of the viscosity of the microgel suspension in Channel B as 2.8 mPa s and 2.3 mPa s in Channel C. The values seem to be in agreement with the value we measured from bulk rheology i.e. 2.42 mPa s with an error of 15.7% and 5%. Also, the flow through the channel is quite laminar with R_e<< 2100 for all the flowrates used. We also calculated the wall shear rates and wall stresses in Channel B and C using equation 4-f and 4-g and plot a flow curve and compare it the with bulk rheological results (Figure 4-9).

Table 4-5 Table depicting the values of Reynold's number, Wall shear rates and wall stresses in Channel B and C considering them as a slit die where W>H.

Flowrates (µl/hr)	**Channel B**			**Channel C**		
	Reynold's number, R_e	**Wall shear**, $\dot{\gamma}_w$ (1/s)	**Wall stress**, σ_w (Pa)	**Reynold's number**, R_e	**Wall shear**, $\dot{\gamma}_w$ (1/s)	**Wall stress**, σ_w (Pa)
100	0.3	4×10^3	9	0.2	535	1.3
300	0.8	1.2×10^4	26.4	0.5	1.6×10^3	3.7
500	1.3	2×10^4	43.3	0.8	2.7×10^3	6.1
800	2.1	3.2×10^4	68.3	1.3	4.3×10^3	9.6

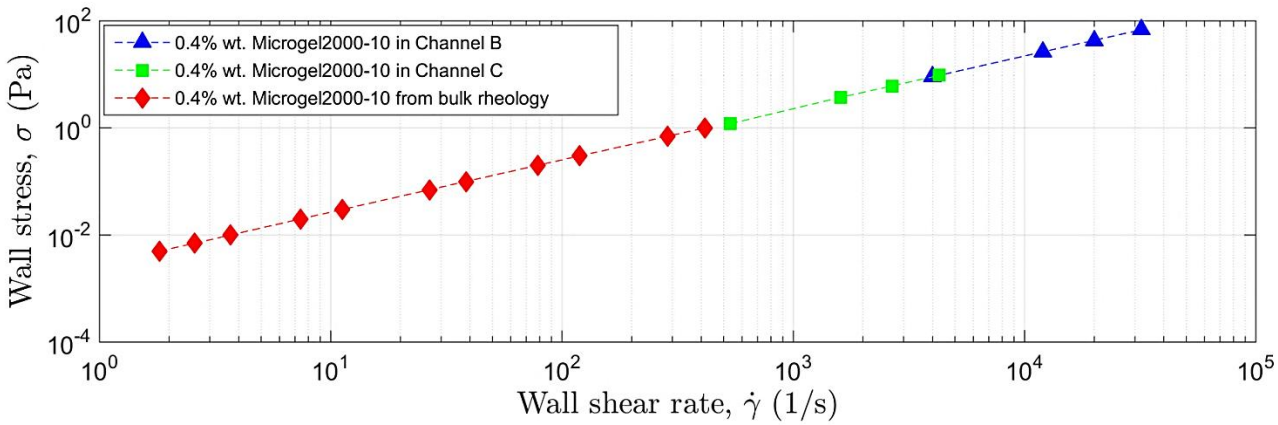

Figure 4-9 Plot of wall stress (Pa) and wall shear rate (1/s) calculated using the working equations for slit die (W>H) in Channel B and C and the shear stress vs shear rate plot for 0.4% wt. Microgel2000-10 as obtained from the bulk rheological measurements.

The above flow curve more or less shows the rheology of the suspension in Channel B and C together with the bulk rheological results at relatively lower shear rates. As we know, a slit die rheometer can be used to subject the fluid to higher shear rates, we conclude that the dilute Microgel2000-10 doesn't change its rheological behaviour even at higher shear rates in channels with dimensions higher than the average size of the particles in the suspension.

4.4.2 Flow through Porous Media- Frontal Filtration

We flow 0.8% wt. Microgel2000-10 through Frontal-20 and Frontal-40 porous channels. To comprehensively understand the mechanism of jamming inside the porous media, we first illustrate with the case of the flow of 0.8% wt. of Microgel2000-10 at a constant flowrate, Q= 100 µl/hr (direction of flow: Region A to Region B) through the Frontal-20 porous channel (see Figure 4-3). Figure 4-10 displays the phase contrast micrographs showing the dynamic jamming of the same. It can be clearly seen that as the particles pass through the porous array, they start aggregating at t= 20s. Meanwhile, the pressure inside the channel is observed to rise (see Figure 4-11). As the aggregation of the particles continues, it leads to the formation of a solid like gel that eventually jams in Region B at t= 32s. This jamming is better quantified in terms of jamming time (t_j) which is the total time the microgel suspension takes to jams the porous media. This jamming time t_j is defined as the difference between the times when the pressure starts rising

(see Figure 4-11) up due to jamming (t_p) and the time when the first particle reaches the porous part of the channel (t_0) .

$$t_j = t_p - t_0$$

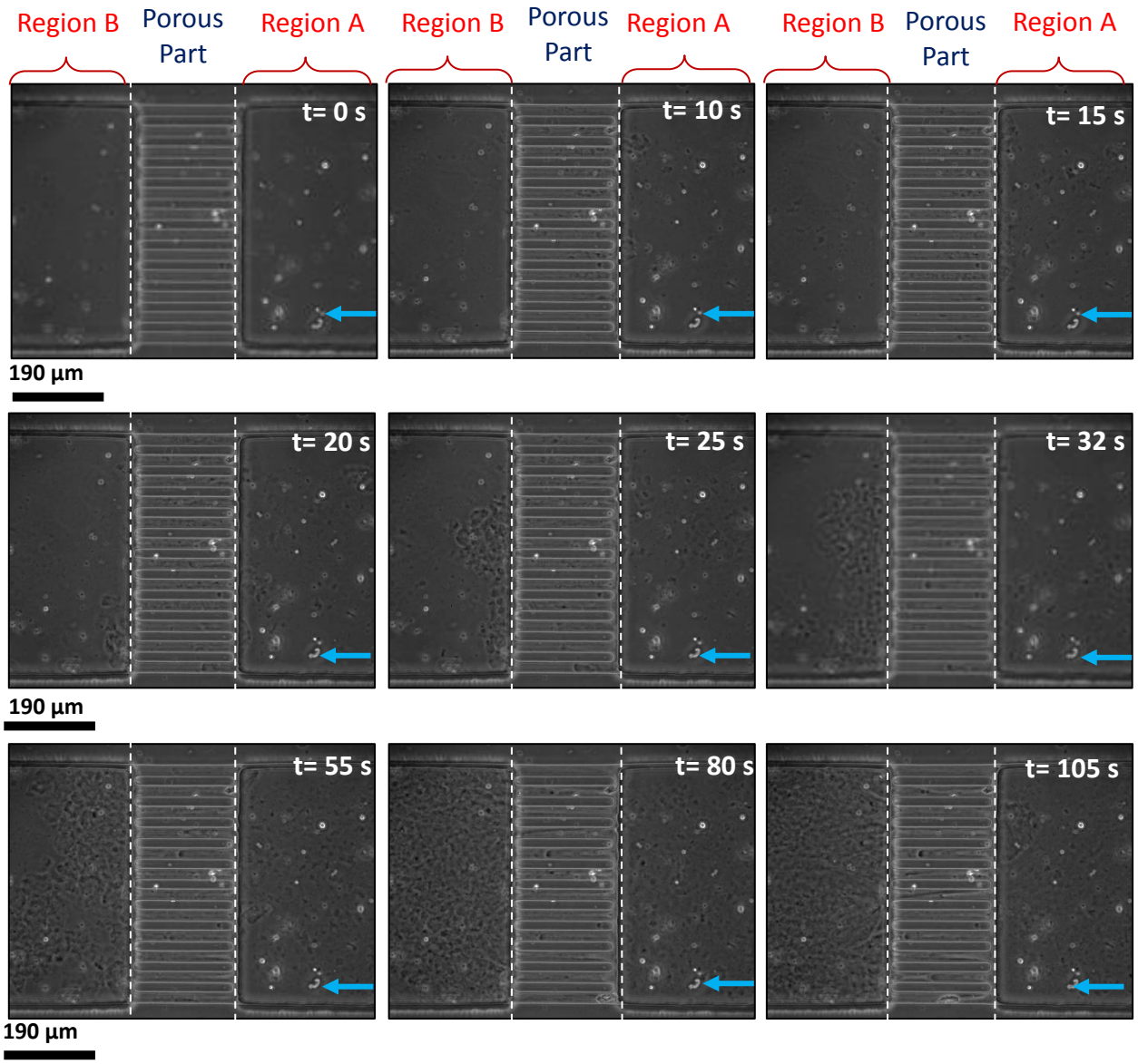

Figure 4-10 Phase contrast snapshots showing the jamming dynamics of porous media for frontal filtration (Width and hieght of the pillar =20µm, length L is 200 µm). The flow (from Right to Left) of 0.8% wt. Microgel2000-10 is depicted by the blue arrow .

In terms of jamming time, we see the first particle reaches the porous part at t= 0s and the pressure starts rising at t_p=32s which makes the jamming time, t_j=32s. The events that lead to jamming and afterwards are also depicted with black arrow in the Figure 4-11.

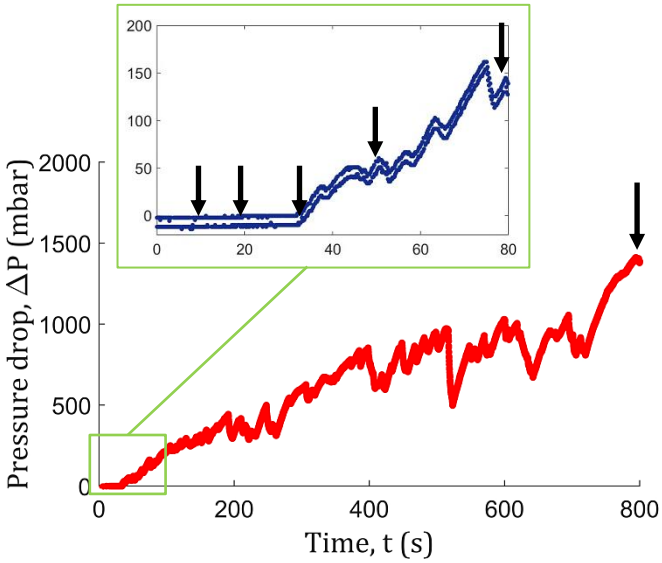

Figure 4-11 Raw data of pressure drop across the Frontal-20 channel for the flow of 0.8%wt. Microgel2000-10 at a constant flowrate, Q= 100µl/hr. (Black arrows correspond to the events shown in Figure 4-10)

As the time proceeds, the aggregates begin to grow further and completely block the channel. The jamming of the channel is evident from the rapid increase in the pressure drop inside the channel and also from the phase contrast snapshot taken at t=105s in Figure 4-10. As the microgel continues to flow, the pressure keeps increasing making the PDMS elastomer to expand in Region A (shown by yellow arrow in Figure 4-12(a)).

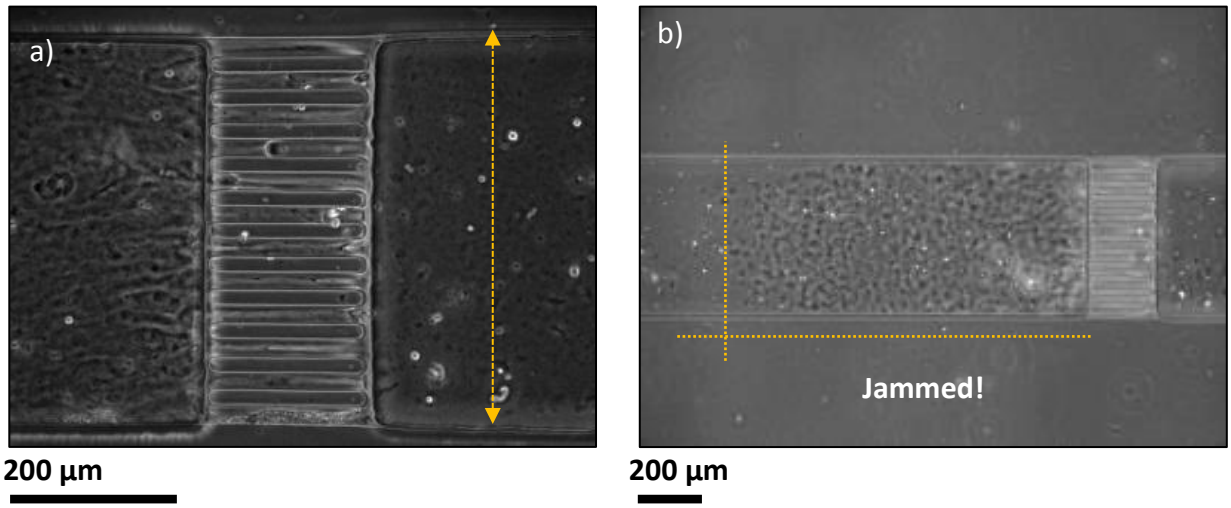

Figure 4-12 (a). Phase contrast snapshots of Frontal-20 porous channel for the flow of 0.8% wt. Microgel2000-10 at a constant flowrate, Q= 100 µl/hr showing the expansion of the PDMS channel due to the increase in pressure owing to jamming in Region B and (b). shows a low magnification phase contrast snapshot showing length upto which Region B is jammed after time, t= 2270 s.

Figure 4-12(b) shows the microgel aggregates with big lumps which span and cover a length of around 1 mm after t=2270s in Region B. In the videographs, it is seen clearly that these aggregated jammed microgel do not move away even when the flow pushes them. It is also important to be sure that the microgel jams along the whole height, h of the Region B. To check this, we flow a 0.8% wt. Microgel2000-10 seeded with tracers (1µl of 1µm carboxylate tracers in 10 ml of microgel suspension)(FluoSphere® carboxylate 1µm (Yellow-green), Life technologies) at flowrate, Q= 100 µl/hr. A small volume of tracers is used to avoid saturation. We then use fluorescence microscopy to focus at each plane of Region B starting from z=0 to z=h with z= 0 corresponding to the base of the channel (see Figure 4-13). We are able to sharply focus on the fluorescent tracers in the jammed microgel at every focal plane from z= 0 to 120 µm in the Region B of the channel. The mere presence of the tracers in all the focal planes clearly indicate that the suspension completely jammed the porous media along its height in Region B.

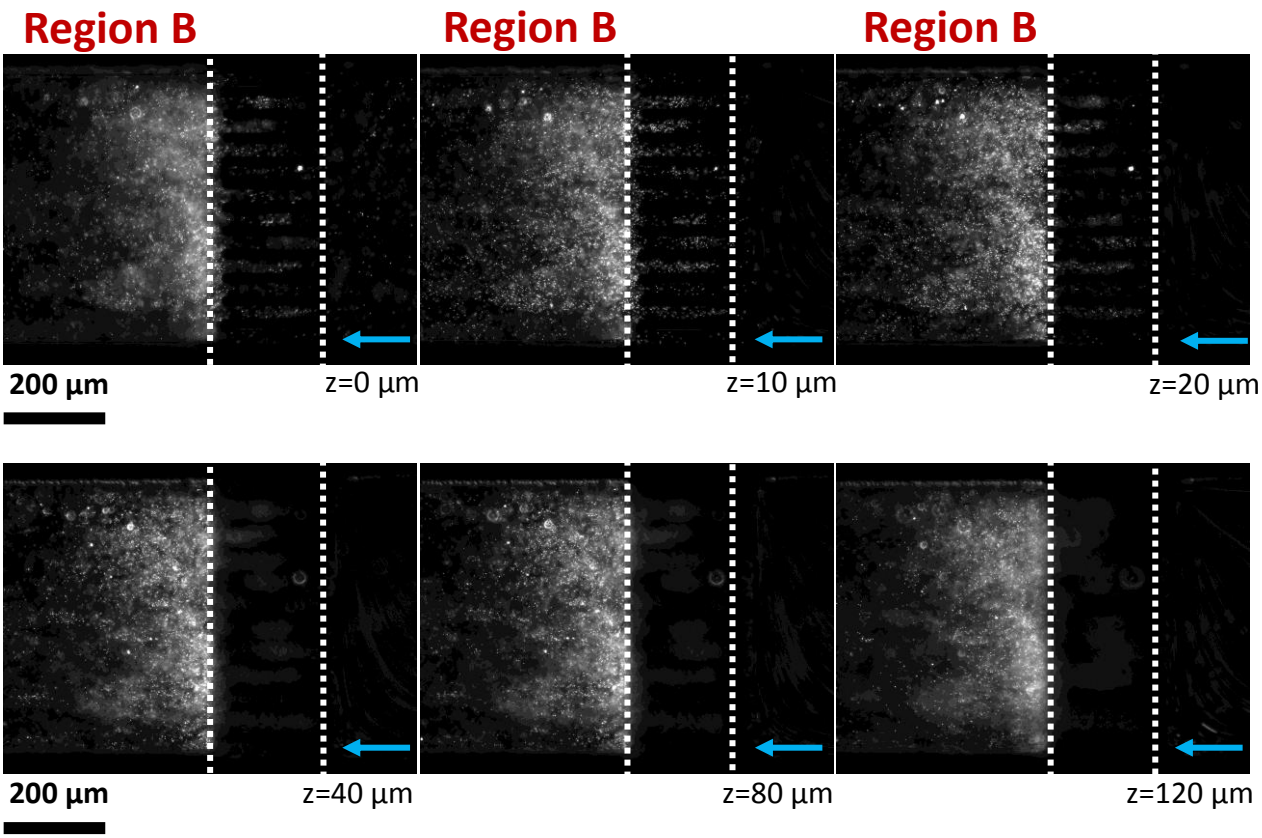

Figure 4-13 Fluorscent micrographs at different z (0 to h= 120µm) showing Frontal-20 porous channel jammed under flow of 0.8% wt. Microgel2000-10 at Q=100µl/hr. The direction of flow is depicted by the blue arrow.

Another interesting thing to notice here is that the channel is completely jammed by a dilute microgel suspension and the fact that the jamming/clogging of the particles is observed on the "other side" of the porous channel (i.e Region B) and not Region A at the entrance as expected. This peculiar phenomenon of jamming is likely to be linked to shear-induced aggregation (section 2.5.6) i.e when the shear is large enough, particles of the suspension overcome the interaction potential and form large viscous aggregates with a non-Newtonian behaviour (Xie et al., 2010). In our channels, such high shear rate is reached quickly inside the pores of the porous array. The gel/aggregates cannot form at the entrance since they have not been aggregated yet but have to form inside the porous channels and can stop flowing at the outlet. Inside the pores, the suspension is only aggregated but not jammed because the pressure gradient and thus the wall shear stresses are high. These aggregates then interconnect to form a solid like sticky gel in Region B at the outlet which may stop flowing because the pressure gradient gets lower and the wall stress in Region B is smaller than the yield stress of the gel. This shear-induced aggregation

observed in porous channels is consistent with our results observed in rheology (see section 2.5.6). In microchannels, shear-induced aggregation can be explained in terms of the hydrodynamic force. For example, Wu et al., studied the jamming in a microchannel bottle neck using a stabilized colloidal dispersion without any electrolytes (Wu, Zaccone, Tsoutsoura, Lattuada, & Morbidelli, 2009). It is noticed that below a critical shear rate, the jamming is slow as the hydrodynamic forces are not enough to overcome the repulsive potential barrier. Above this critical value, aggregates are formed and sometimes possibly breakage of the aggregates can happen (Sendekie & Bacchin, 2016). In our system, for the case of Q= 100 µl/hr, our system is subjected to an average shear rate of 4 s^{-1} in Region A and B of the channel and 3470 s^{-1} inside the pores of the porous array (refer Table 4-6 for Reynold's number and average shear rates for different flowrates used).

Table 4-6 Table summarizing the values of Reynold's number and average shear rates for different flowrates in Region A&B and porous part of Frontal-20 porous channel for the flow of 0.8% wt. Microgel2000-10 (assuming viscosity= 7.5 x 10^{-3} Pa s and density= 1000 kg/m^3).

Flowrate, Q (µl/hr)	**Region A&B**		**Porous Part**	
	R_e	**$\langle\dot{\gamma}\rangle$ (1/s)**	**R_e**	**$\langle\dot{\gamma}\rangle$ (1/s)**
100	0.013	4	0.18	3472
10	0.0013	0.4	0.018	347
20	0.0025	0.8	0.037	694
30	0.0038	1.2	0.056	1042
50	0.0063	2	0.093	1736
75	0.0094	3.1	0.14	2604
200	0.025	8.2	0.37	6944

To further validate the hypothesis, we perform some more experiments to characterize the formation of particle aggregates. In the literature, there are several techniques to measure the formation of particle aggregates. These include light scattering, microscopy, particle counting, turbidity measurements, sedimentation and rheology (Holthoff et al., 1997; Russel W.B, 1989; Xu & Sun, 2011). In all these techniques, the particles are allowed to evolve and form aggregates with time i.e they are all time-resolved techniques.

Turbidity is defined as the degree to which a fluid loses its transparency due to large particles suspended in the fluids. Here, we use 4.5% wt. Microgel2000-10 to get some qualitative measurements on turbidity. The reason for using high concentration for these measurements is because changes in high concentrations are more easily observed, rather quick and less time consuming. We first perform a simple experiment of observing the intensity changes when a 4.5% wt. Microgel2000-10 is stirred at 2500 rpm (which roughly translates to a shear of $2\pi \times 41.6 = 262$ s^{-1}) using a magnetic stirrer of length 1 cm at room temperature (21°C) (see Figure 4-14). Of course, the shear at the tip of the magnetic stirrer will be higher. This is estimated to be around 600 s^{-1}. Hence, the average shear should lie somewhere between 262 and 600 s^{-1}. We place the sample inside a cuvette and use an LED backlight. The stirring caused the turbidity to change which is reflected in the transmitted intensity and is recorded by a DSLR camera (D7200, Nikon). Later, we measure the intensity when the stirring is stopped to know how the system recovers. The images taken by the camera are analysed using ImageJ software. The measured intensity, I_m is normalized with the background intensity, I_g.

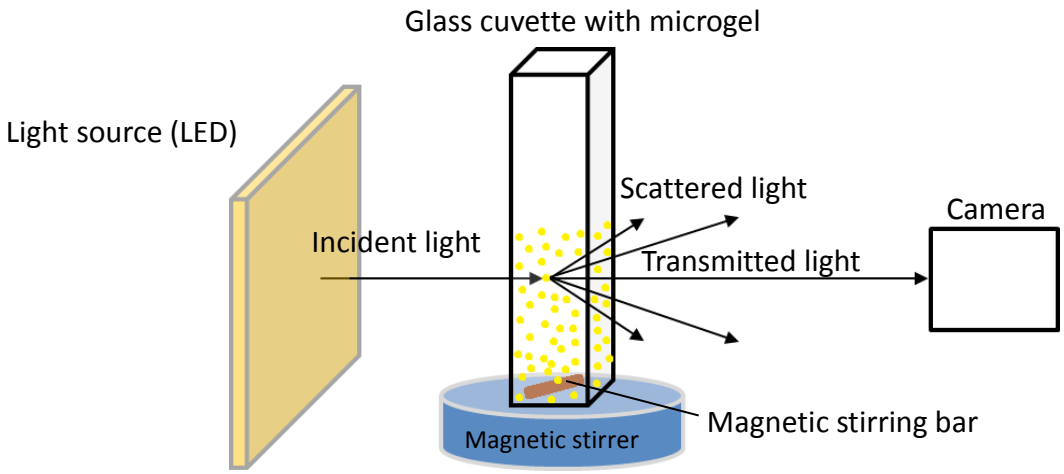

Figure 4-14 Schematic of the setup used to measure the turbidity of microgel suspension under shear.

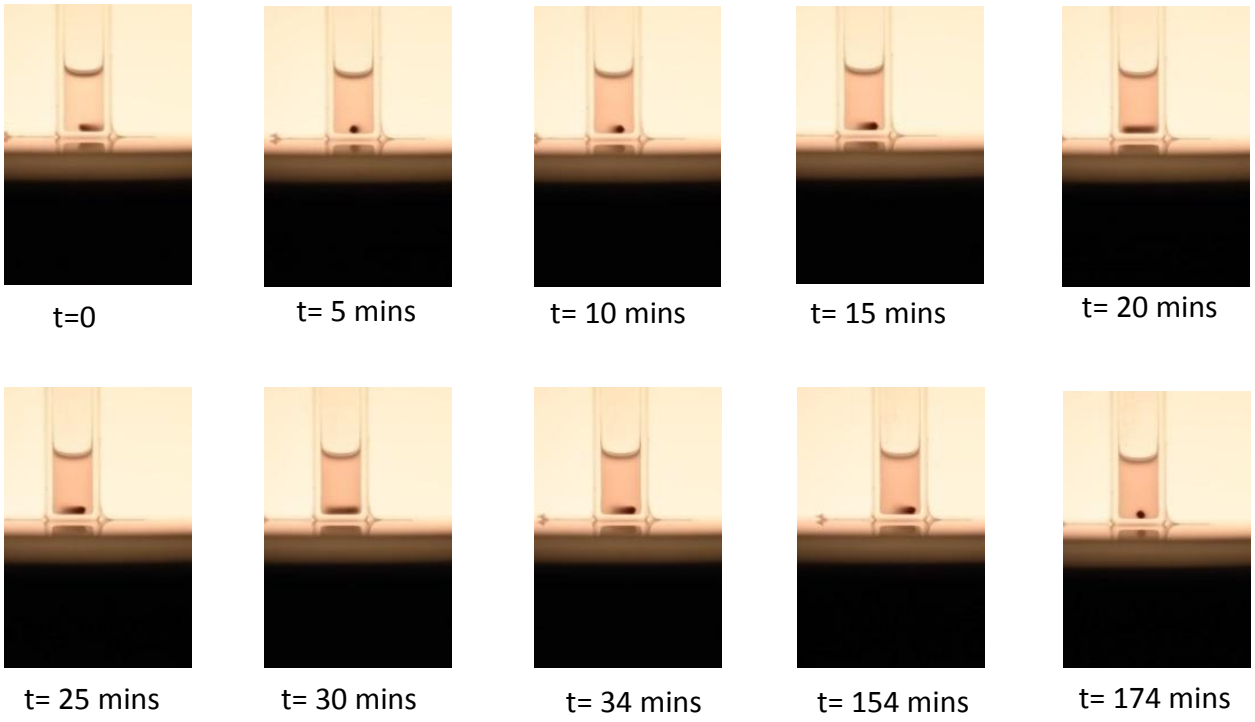

Figure 4-15 Time-resolved camera images of 4.5% wt. Microgel2000-10 under shear (250-600 s^{-1}). The images show a clear change in the intensity with time.

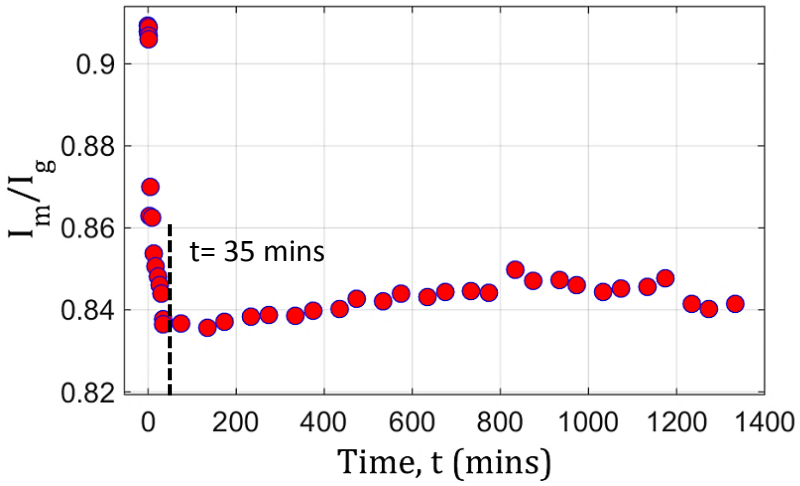

Figure 4-16 Temporal evolution of the intensity of 4.5% Microgel2000-10 under shear due to a magnetic stirrer of length 1cm rotating at 2500 rpm.

The drop in the intensity is a consequence of increasing turbidity in the system which happens when particles form aggregates. These aggregates scatter more than the incident light. This

decrease is found to be rapid within the first 10 mins and later becomes slow till *t*=35 mins (see Figure 4-16). After *t*= 35 mins, no more change in the intensity is observed even though the system is still under shear. This implies that during the early stages of aggregation, the small particles form aggregates faster until they become large enough. Once the particles are sufficiently large, their tendency to further aggregate decreases. We left the experiment to run till time, *t*= 5400 mins and found that the I_m/I_g have the same constant value of 0.84.

The stirring is stopped after *t*=5400 mins and it is observed that the suspension recovers back to its original state (see Figure 4-17). Here again, the recovery process is observed to escalate quickly first and then slowly until it eventually reaches a constant state. Here again, we see similar trend with the sufficiently big particles ready to quickly disassociate to smaller ones.

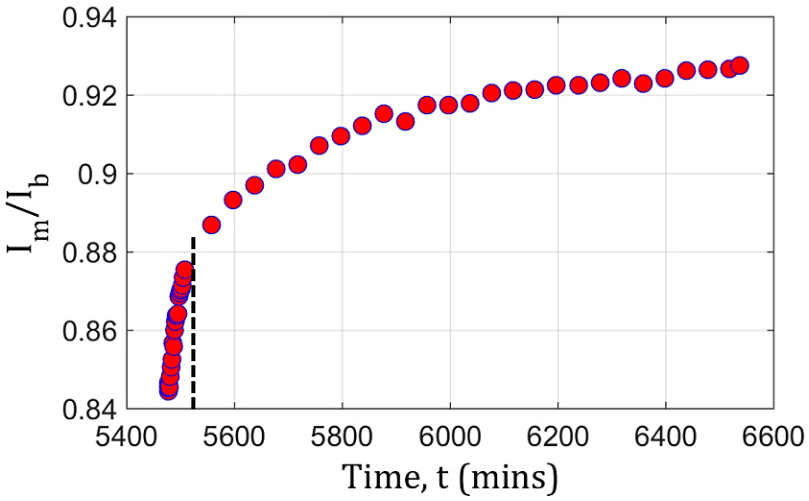

Figure 4-17 Time evolution of the transmitted intensity after the removal of shear at around 5400 mins.

Although these experiments are quite qualitative, they throw some light on the particle aggregation in the microgel suspensions and their subsequent recovery. A quick literature survey shows several reports on shear-induced aggregation in biological fluids and synthetic systems. There are early reports of rheopexy (increase in viscosity with time) due to shear–induced aggregation in blood platelets (Hung, Hochmuth, Joist, & Sutera, 1976; Jen & McIntire, 1984; Peterson, Stathopoulos, Giorgio, Hellums, & Moake, 1987), in proteins (Oates, Krause, Jones, & Colby, 2006) and in colloidal system (Rammensee, Slotta, Scheibel, & Bausch, 2008). The shear induced aggregation of polystyrene-acrylate latex spheres have been studied using light

scattering techniques (Zaccone, Gentili, Wu, Morbidelli, & Del Gado, 2011). In another work, the dramatic effect of shear on the stability of non Brownian particles at low volume fraction is demonstrated (Guery et al., 2006). However, all these reports show an irreversible change in the system which is in contrast with the preliminary results we get from our system i.e optically our system reverts back to its original state. To fully understand, we need further investigations in a controlled system perhaps light scattering and rheo-optics for different concentrations and at different temperature.

We now explore the effects of surface wettabilities, flowrates and pore/particle size ratio on the jamming phenomenon in porous media for frontal filtration.

A. Effect of Surface

We first study the effect of the surface wettabilities of the microchannels on the jamming. For this, we used PDMS microchannels of different wettabilities. For hydrophobic, thermally bonded PDMS channels are used which provides a hydrophobic surface. For completely hydrophilic surfaces, we used a surface modifying agent (both methods are explained in detail in Section 1.3.6). The filtration experiments were performed in porous channels (Width=20µm, Height=20µm) at a constant flowrate, Q= 100 µl/hr and the jamming time, t_j is measured.

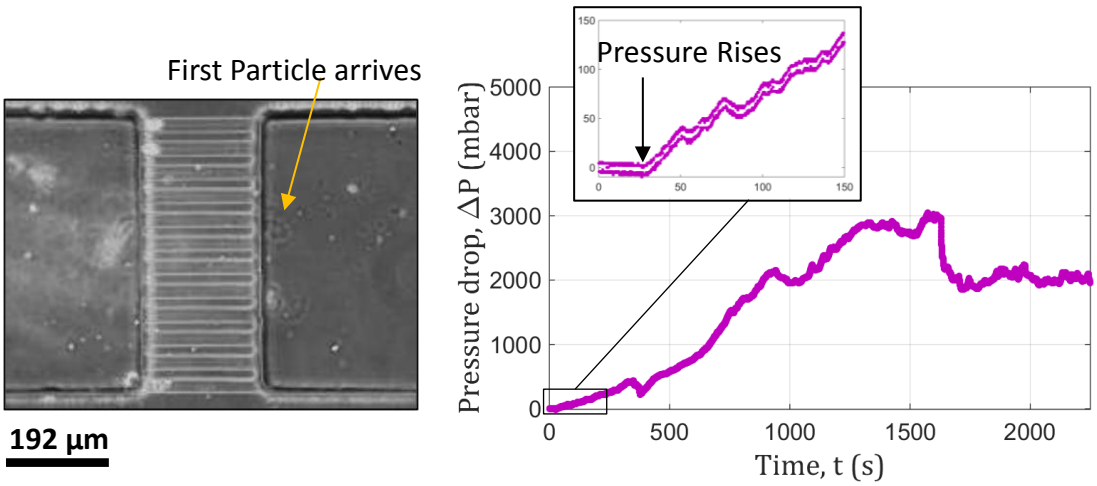

Figure 4-18 (Left) is a phase contrast image of the Hydrophobic porous media just when the first particle arrives the porous part . On right is the raw data for the pressure measurements as a function of time for a constant flowrate, Q= 100 µl/hr.

It can be seen from the above filtration experiment on a hydrophobic porous media that the jamming time is 32s which is same as the jamming time in a hydrophilic porous media (t_j = 32s). This indicates that the surface wettabilities do not really play a major role in assisting in jamming under flow as the forces of adhesion of the particles with the channel walls are overcome by the drag forces.

B. Effect of Pore/Particle Size

In this case, we used 0.7% wt. of Microgel4000-10 which has an average particle size of 13µm and injected it into hydrophilic Frontal-20 channel at a constant flowrate, Q= 100 µl/hr. We observe some aggregates formed but no jamming was observed even till t=500s from the pressure data. In another experiment, we demonstrate jamming in porous media for frontal filtration with a different pore size to further validate the results. We injected 0.8% wt. Microgel2000-10 at a constant flowrate, Q= 100 µl/hr through Frontal-40 porous channels. From the Figure 4-19, it can be clearly seen that although the particles form aggregates, they are either not sufficiently big in size or number to block the channel. To explain the formation of aggregates, we go back to section 2.5.1 and ponder upon the particle size distribution of Microgel2000-10. Clearly, the suspension is not monodispersed but has a moderately narrow distribution. This includes particles having almost the same or even bigger size than the dimension of the channel. These particles are experiencing high shear at the walls of the channels and form aggregates but do not jam the channel completely. Although, one can expect to jam the channel at longer time scales. This means jamming is also dependent on the particle to pore size ratio.

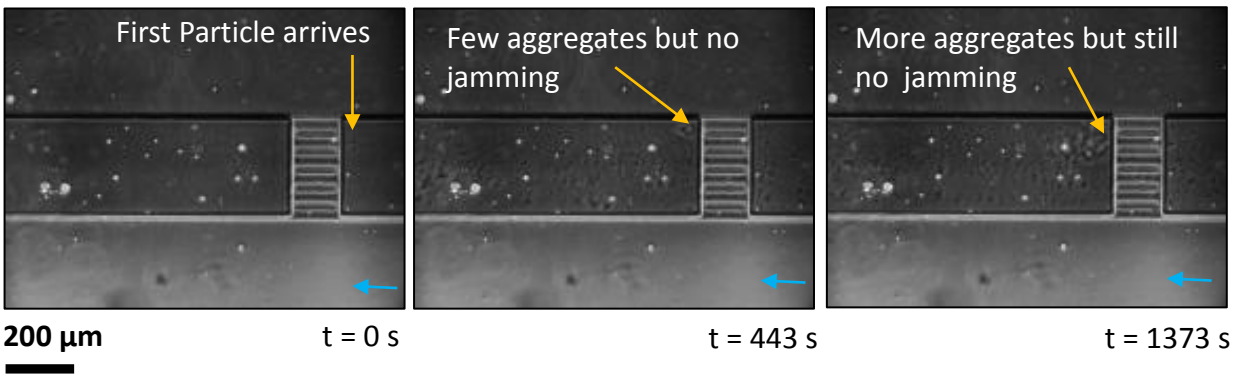

Figure 4-19 Phase contrast images showing the aggregate formation of 0.8% wt. Microgel2000-10 in Frontal-40 porous channel.

C. Effect of Flowrate

We now throw some light on the effects of flowrates on the jamming. We will use only hydrophilic porous media for the filtration experiments for the rest of the work done in this thesis. Figure 4-20 and 4-21 show examples of jamming in Frontal-20 channels at Q= 20 µl/hr and 75 µl/hr respectively.

Q= 20 µl/hr

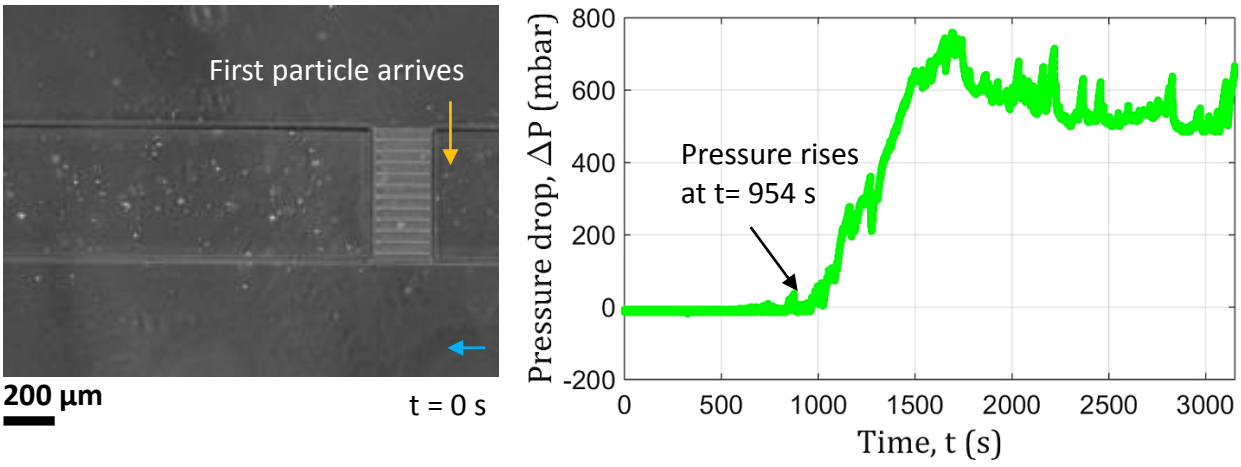

Figure 4-20 (Left) A phase contrast snapshot of Frontal-20 channel with 0.8% wt. Microgel2000-10 flowing at Q= 20µl/hr and the first particle arriving at t=0. (Right) Raw data of pressure rising as a fucntion of time. The total jamming time in this case is 954 s.

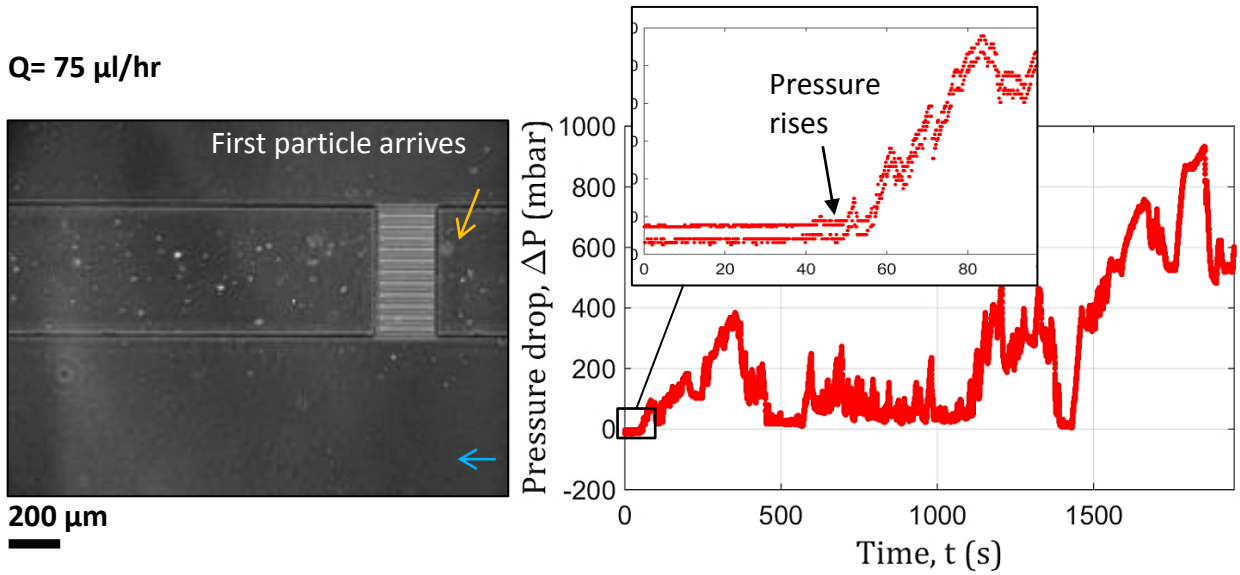

Figure 4-21 (Left) A phase contrast snapshot of Frontal-20 channel with 0.8% wt. Microgel2000-10 flowing at Q= 75µl/hr and the first particle arrives. (Right) Raw data of Pressure riseing as a fucntion of time. The total jamming time in this case is 58 s.

The fluctuations in pressure data is due to the opening and closing of the pore and the aggregates in Region B. For the cases illustrated above and others, we calculated the jamming time, t_j as already mentioned and jamming volume, V_j which is the volume of the suspension required to jam the channel as

$$V_j = Q \, x \, t_j$$

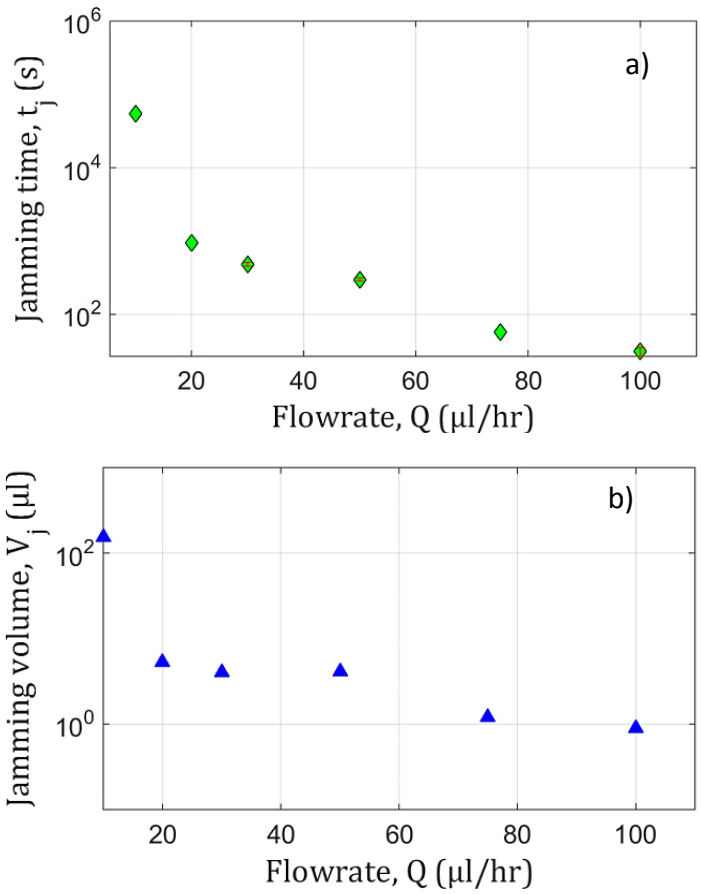

Figure 4-22 Plot of (a). jamming time, t_j as a function of flowrate and (b) jamming volume, V_j as a function of flowrate for 0.8% wt. Microgel2000-10 through Frontal-20 porous channel.

The results can be understood in terms of surface interactions and hydrodynamics. The jamming volume, V_j is seen to decrease with flowrates. Clearly, a delay in jamming is observed for low flowrates. This delay likely occurs due to the high repulsion barrier between the particles and the walls. With the help of microscopic visualization, it is observed that the delay is due to sometimes temporary sticking and sliding of the aggregates formed. As the flowrate increases, the drag forces become high enough to break the repulsion barrier and leads to sticking of the aggregates on the channel wall and eventually blocking it. However, for higher flowrate, Q= 200 µl/hr, we see in Figure 4-23 that there are paths created by the fluid (depicted by yellow arrows) within the aggregates in Region B. At this flowrate, it never completely jams the channel because at this high flowrate, the rate of erosion is greater than the rate at which the aggregates are forming.

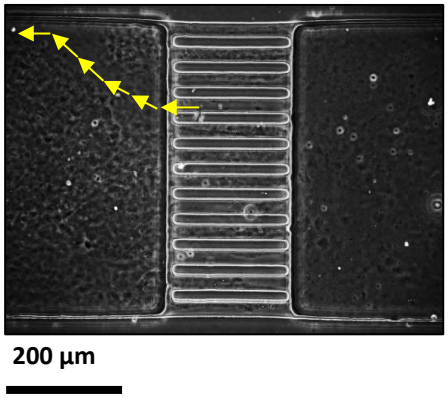

Figure 4-23 Phase contrast image of porous Frontal-20 channel for the flow of 0.8% wt. Microgel2000-10 at Q= 20 µl/hr.

D. Effect of Concentration

Here, we used a different concentration of of Microgel2000-10 in Frontal-20 channels to see how concentration affects the jamming dynamics. We compare the results obtained from flowing 0.4% wt. and 0.8% wt. Microgel2000-10 in the same channel at the same time. We observe that for lower concentration, it is relatively difficult to clog the channels. In Figure 4-24, we see the formation of aggregates but no jamming even at higher time for the flow of 0.4% wt. Microgel2000-10. The filter cake cannot sustain the shear rate as it gets continuously eroded by the fluid. The rate of erosion is greater than the rate of adhesion.

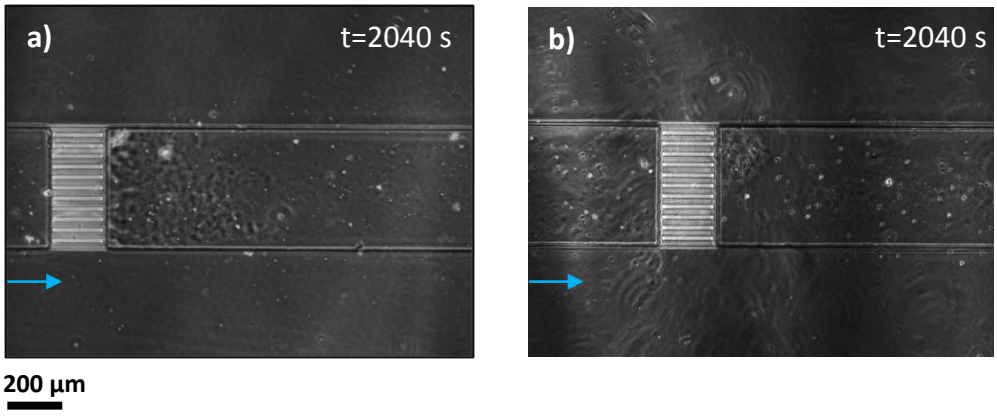

Figure 4-24 Phase contrast micrographs taken at time, t=2040s at constant flowrate, Q= 100 µl/hr of (a). 0.8% wt. Microgel2000-10 and, (b). 0.4% wt. Microgel2000-10.

E. Permeability Measurements

Here, we characterize the permeability of the microgel filter cake formed inside Frontal-20 porous channel. We first estimate the permeability of the porous media itself by flowing DI water at various flowrates and measuring the corresponding pressure drop inside the channel (see Figure 4-25).

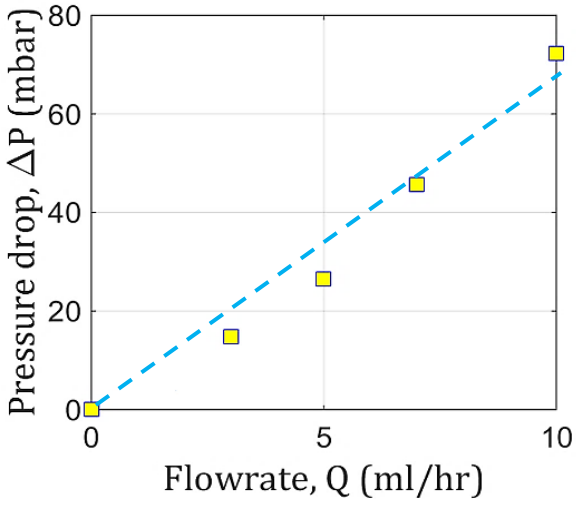

Figure 4-25 Plot of Pressure drop (mbar) as a fucntion of flowrates, Q (ml/hr) for the flow of water through Frontal-20 porous channel.

Using Darcy's law,

$$Q = \frac{\mathcal{K}\, A\, \Delta P}{\eta\, L}$$

The permeability ($\mathcal{K}$) of the Frontal-20 porous channel comes out to be, 1.54 x 10^{-12} m^2 or 1.57 Darcy, which indicates that the porous channel is quite permeable. We now measure the permeability of the filter cake formed inside the Frontal-20 channel as a result of jamming of 0.8% wt. of Microgel2000-10. The filter cake is formed at flowrates, Q= 100 µl/hr. While forming the filter cake, the flow is directed from Region A to Region B of the channel. Once the filter cake is formed, we measure its length and then flow water through it but in the reverse direction i.e. from Region B to Region A in order to avoid the loss of microgel loss during the measurement

(Figure 4-26 and 4-27) (note: since the flow is reversed, the pressure values are recorded in the negative scale due to the unchanged position of the pressure probes in the porous channel). For every flowrate, Q, we read the corresponding pressure drop inside the channel. The plot of the pressure drop versus flowrates is used to calculate the permeability of the microgel filter cake with the help of Darcy's law.

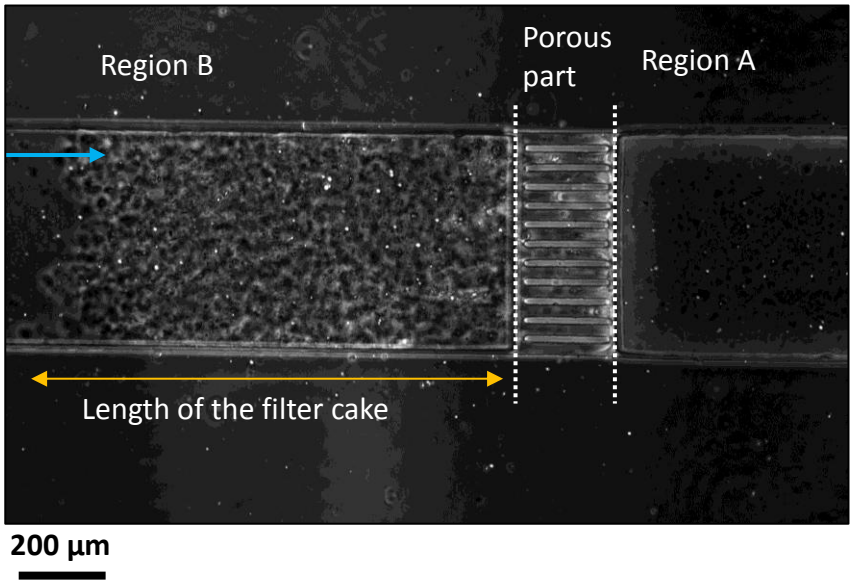

Figure 4-26 Phase contrast image of a jammed Frontal-20 porous channel showing the microgel filter cake formed in Region B at a constant flowrate, Q= 100 µl/hr.

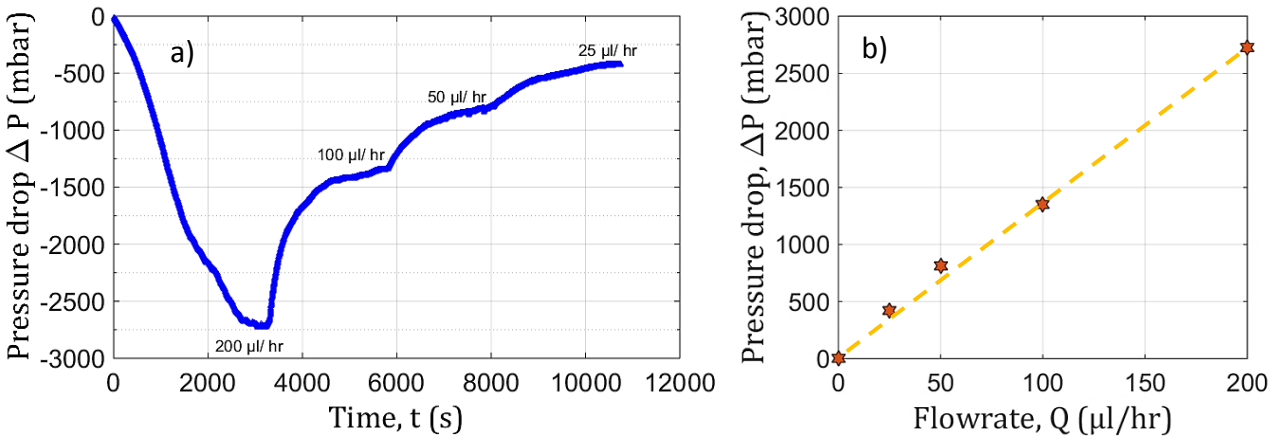

Figure 4-27 (a). Raw data for the pressure drop with time for different flowrates in Frontal-20 porous channel with a 1mm thick microgel filter cake formed at a constant flowrate of 100 µl/hr and (b). Plot of pressure drop as a function of flowrate.

The permeability of the filter cake is calculated to be 3.8 x 10^{-15} m^2 or 3.9 x 10^{-3} Darcy. We will later see in chapter on permeability that the value of permeability can be much lower than the values we get in this particular chapter. The inconsistency in the permeability values is due to the fact that the filter cake here is quite loose as it formed after the pore unlike in the permeability experiments (which we will see later in chapter 5), where the filter cake formed on the supporting membrane is quite dense.

4.4.3 Flow through Porous media- Lateral Filtration

We now know the capability of dilute Microgel2000-10 to form a filter cake when flowed through a porous array in the case of frontal filtration. This microgel filter cake helps in controlling the loss of fluid. However, to be of use in oil-field to prevent the fluid loss through highly permeable rock formations, a typical fluid loss additive should be able to form a thin filter cake in the direction perpendicular to the direction of principal flow (see Figure 4-28).

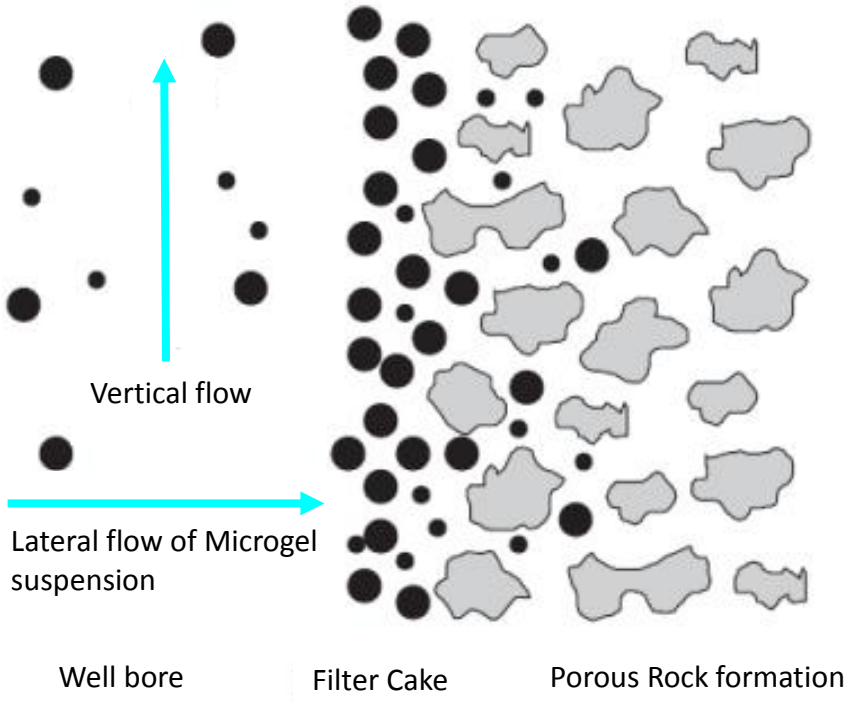

Figure 4-28 Schematic showing the flow of fluid loss additives in both vertical and lateral direction resulting in the formation of the Filter Cake (Image reproduced from:Petroleum Engineer's Guide to Oil Field Chemicals and Fluids by Johanees Fink (Fink, 2015))

Hence, in this section we investigate the formation of filter cake by 0.8% wt. Microgel2000-10 in microfluidic porous media using a lateral filtration porous channel in a pressure driven experiment (refer Table 4-4) and then demonstrate the prevention of fluid loss through the porous array in terms of the reduction in the measured flowrates, Q_m. (Note: All the channels used in this section are hydrophilic as we have already seen that surface wettabilities have no effect on the jamming of microgel suspension).

A. Effect of Pressure

- P_1= 40 mbar, P_2= 20 mbar and P_3= 10 mbar

The measured flowrate at steady state, Q_m at end P_3 for the flow of water through porous media Lateral filtration is 889 ± 23 µl/hr (see Figure 4-29) when the ends P_1, P_2 and P_3 are maintained at constant pressure of 40, 20 and 10 mbars respectively. This very high flowrate through the lateral arm P_3 suggests the high permeability of the porous media.

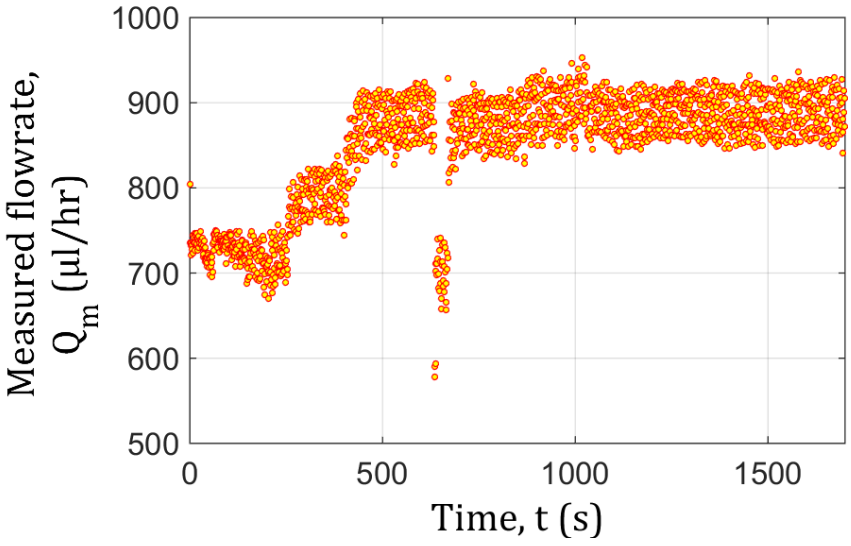

Figure 4-29 Raw data showing the measured flowrates, Q_m at end P_3 for the flow of water through lateral filtration porous media from end P_1 to P_2 where P_1 is maintained at 40mbar, P_2 at 20 mbar and P_3 at 10 mbar.

We now flow 0.8% Microgel2000-10 through the same Lateral-20 channel with all three ends maintained at the same pressure i.e 40, 20 and 10 mbar. Initially, the flowrate has a steady value (see Figure 4-31). The aggregates starts forming after 36 s and continues to grow to form a solid gel like structure. This gel like mass is the filter cake which at 64 s is partially preventing the further

loss of fluid throught it. It is reflected in the drop in the measured flowrate in the lateral arm from 242 µl/hr to 179 µl/hr. As more microgel continues to flow, the filter cake becomes bigger and blocking more fluid till at time, t= 388 s, the measured flowrate drops to 2.4 µl/hr and stay constant till the end of the experiment. At this time, we believe that the filter cake has completely occupied and jammed the porous array and the lateral arm.

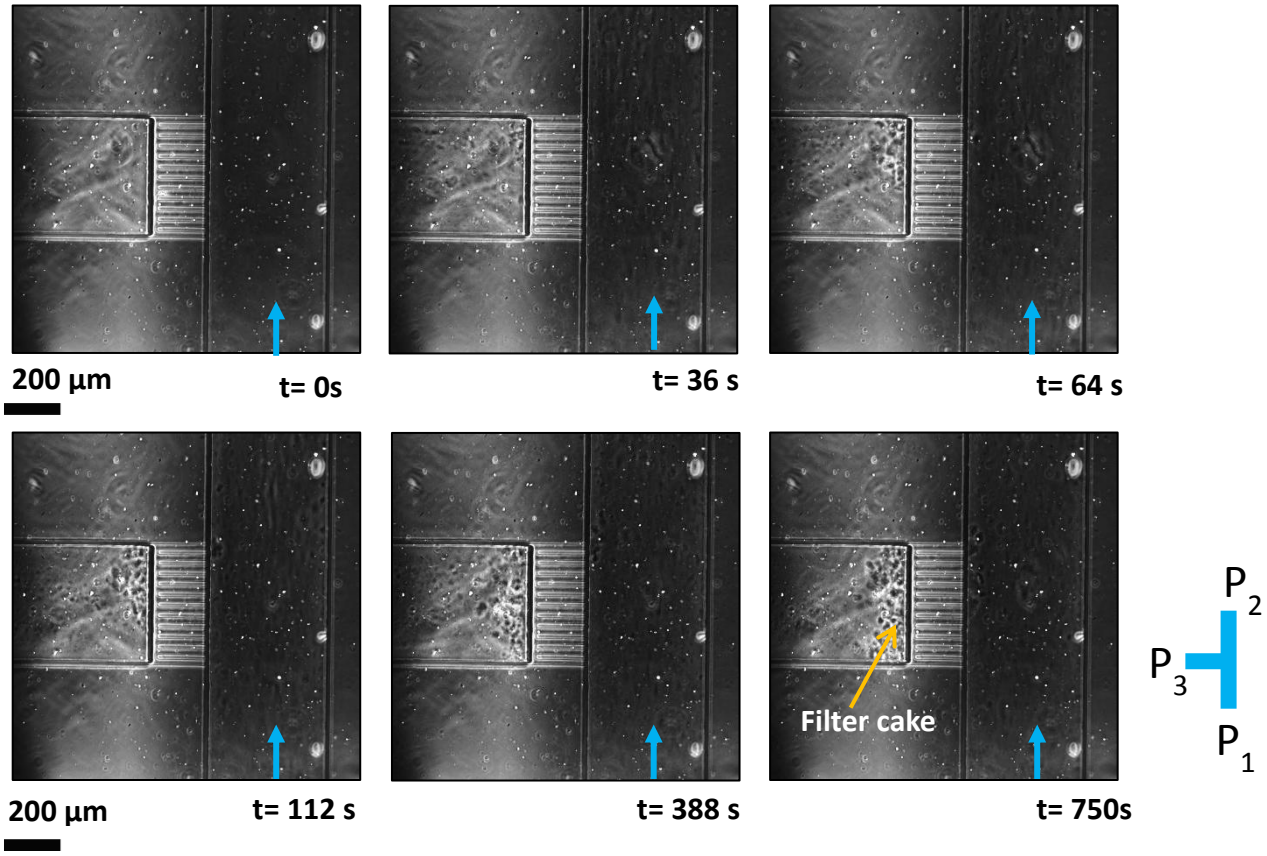

Figure 4-30 Series of phase contrast snapshots over a course of time in porous channel (Lateral-20). The filtration experiment shown here is constant pressure driven experiment with P_1= 40 mbars, P_2= 20 mbars and P_3= 10 mbars.

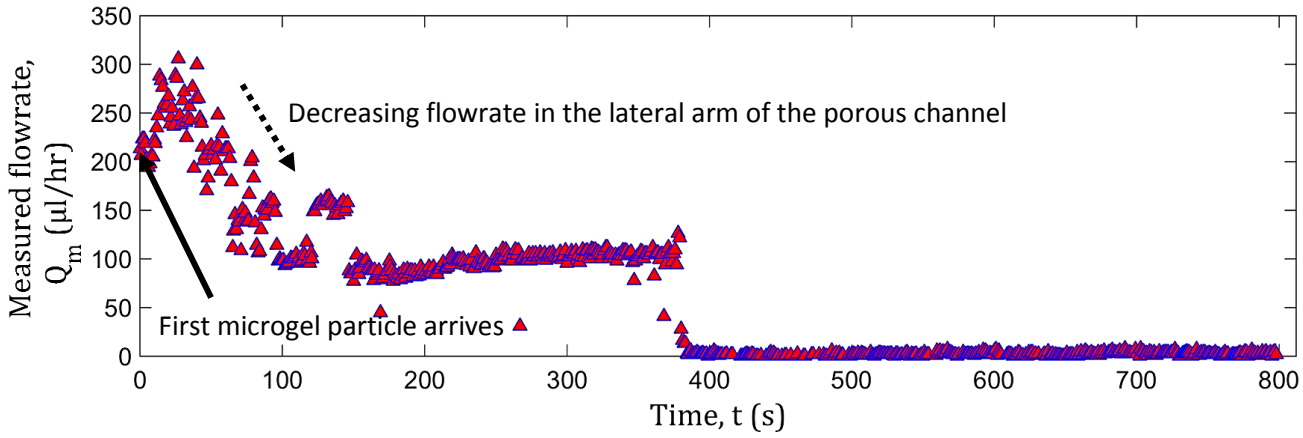

Figure 4-31 Typical raw data recorded by the flow rate sensor showing the temporal evolution of flowrate when 0.8% wt. of Microgel2000-10 is flowed through the Lateral-20 porous channel. The flow is Pressure controlled with P_1= 40 mbars, P_2= 20mbars and P_3= 10 mbars.

The fluid loss is quantified in terms of the drop in the flowrates. Compared to water, we observed a huge drop by 99.7%, while for microgel the drop was 98.87%. For the final reduced flowrate, Q= 2.4 µl/hr (at t= 750s), we calculate the permeability of the filter cake using the pressure drop, $\Delta P = \frac{P_1 + P_2}{2} - P_3$ = 20 mbars and the approximate thickness of the filter cake, L= 140 µm.

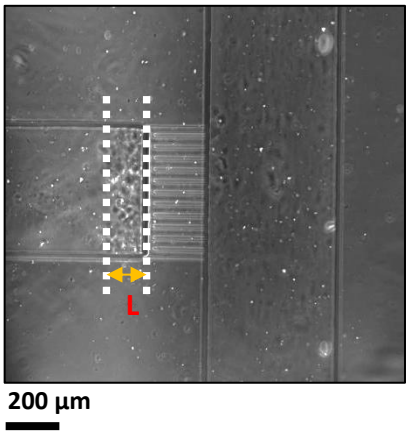

The permeability of the filter cake is estimated to be 5.4 x 10^{-16} m^2. Here again, the high permeability of the filter cake as compared to the values obtained in chapter 5 signifies that the filter cake formed here is not dense. Similar experiments with varied pressures at end P_1, P_2 and P_3 show a dynamics build-up of the microgel filter cake in the lateral arm of the channel which progressively helps prevent the loss of fluid.

4.5 Conclusions and Perspectives

The results from the flow experiments in linear microchannels of cross sectional area 1350 μm^2 and 5100 μm^2 shows that the very dilute 0.8% wt. Microgel2000-10 behaves like a Newtonian fluid with no change in the viscosity even if the wall shear rate are as high as few thousand s^{-1}. The viscosities of Microgel2000-10 are calculated from the hydrodynamic resistance and are found to be 2.8 and 2.3 mPas which is in good agreement with the value from the bulk rheology. However, in a channel with the same dimension as the size of the particle i.e channel with cross section 300 μm^2, the results are contrasting. Here, we observed an increase in the apparent viscosity which is due to the impact of size effects on the hydrodynamic resistance. In frontal filtration, our experiments illustrate interesting jamming with dilute microgel suspension at the exit. We show the impact of high shear rates on the suspension leading to formation of aggregates. These aggregates link and stick further to form a gel like mass. The formation of these aggregates is controlled by the repulsive potential barrier between the particles. At low shear rates and low concentration, the collision frequency is low, hence there is a delay in jamming. High shear rates causes the particles to overcome the barrier between them leading to the formation of aggregates that stick to the wall. In lateral filtration, we have shown how fluid loss is stopped through the porous media after a filter cake of the microgel suspension is formed again at the exit. The fluid loss is quantified in terms of the reduction in the measured flowrates in the channel. We observe that the suspension forms the filter cake with the same mechanism as in frontal filtration and this filter cake very effectively stops the further flow. For the various applied pressure, we found that the flowrate is significantly reduced in a matter of few minutes.

Chapter 5

Permeability Measurements of Microgel Filter Cake

Table of Contents

Chapter 5 Permeability Measurements of Microgel Filter Cake

5.1 Research Objectives

The main objective of this chapter is to measure how effectively the dense microgel filter cake limits the flow of water i.e. to determine the permeability of the porous filter cake. Here, we present a simple experimental setup to form a porous filter cake of microgel suspension on a filter membrane by slow compression using high pressure flow (>6 bars) inside a millifluidic polycarbonate (PC) cell and to measure the permeability of the filter cake under weak flows using Darcy's law. We also systematically characterize the rheology of the filter cake formed to get a quantitative idea about the mechanical properties from rotational flow and from deformation under normal forces and the viscoelastic properties from oscillatory measurements.

5.2 Background

The flow of viscous fluids through porous media has long been of considerable interest, with direct applications in diverse fields such as heterogeneous catalysis, powder metallurgy, chromatography in gels, groundwater flow, transport through biological tissue and enhanced oil recovery. Speaking strictly in context of soft gel systems which apparently have widespread use in food industries because of their easy deformation and a very strong holding power (Ambari, Amiel, Gauthier-Manuel, & Guyon, 1986), it is of great importance to study the permeability and rheological properties of the filter cake formed by these gel systems. However, there are several limitations when investigating the flow processes happening inside the filter cake arising from the random distribution of structures on wide length scales and in-accessibilities of the system characteristics such as porosity, tortuosity. For this reason, many semi-empirical laws have been proposed to describe the flow properties that take into account two important characteristics, one of which define the volume fraction of the voids in the porous system and is known as porosity, ϕ_p. The permeability is related to porosity of the porous media. This is given by the relation by Carman-Kozeny.

$$\mathcal{K} = \alpha \frac{{\phi_p}^3 D_p^2}{\left(1-\phi_p\right)^2} \tag{5-a}$$

where, ϕ_p is the porosity of the porous media, α is a constant of proportionality and unit factor (m^2/Darcy), D_p is the average diameter of the equivalent particles constituting the porous

medium (by analogy with granular material) and $\mathcal{K}$ is the permeability (m^2 or Darcy) which is the second characteristic of the porous media and is defined as the frictional loss in the porous media when the flow of fluid through it. Physically speaking, it is a volume of a fluid of unit viscosity passing through a porous media of unit cross section in unit time under the influence of a unit pressure gradient. It is a characteristic of the structure of the porous media and is independent of the absolute pressure and velocities or the nature of the fluid (Wyckoff, Botset, Muskat, & Reed, 1933). An empirical relation given by H. Darcy more than a century ago is of utmost use to determine the permeability of a porous media. Darcy's law (Equation 5-b and Figure 5-1) connects the macroscopic flow property, Permeability, $\mathcal{K}$, to the applied pressure, ΔP and the volumetric flow rate Q (Darcy, 1856).

$$\boldsymbol{Q} = \frac{\boldsymbol{\mathcal{K}\, A\, \Delta P}}{\boldsymbol{\eta\, L}} \qquad \text{(5-b)}$$

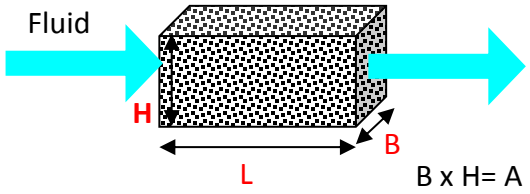

Figure 5-1 Pictorial represenation of a porous media with thickness, L and cross sectional area, A.

where, A is the cross section area of the porous media, η is the viscosity of the fluid flowing through the porous media, L is the thickness of the porous structure. This empirical linear relation is valid only for single phase fluid flows in porous media at low Reynolds number, R_e regimes (Loosveldt, Lafhaj, & Skoczylas, 2002). The fluid is considered to be inert i.e. no chemical reaction in the porous media and incompressible. This relation is a macroscopic result of the Navier-Stokes equation when solved for porous media with multiple connected boundaries (Wyckoff et al., 1933). The filter cake acts as a dense porous media and its permeability can be calculated using Darcy's law by measuring the pressure gradient across the filter cake (representative volume) for applied flow rates. The SI unit of permeability is m^2 but the unit Darcys [D] is more commonly used. The two units are related as 9.8 x 10^{-13}Darcy = 1 m^2. Conventionally, Darcy's law are

applicable to only rigid porous media i.e. when the porous structure is not modified by the flow of fluid across it. On the contrary, in this Chapter we consider the case of a weak porous system of microgels which deforms on the application of external stresses coming from the applied flowrates. Hence, the permeability, κ is expected to depend on the flowrates. In section 5.3, we provide a detailed method of estimating the permeability of the soft filter cake (gel phase) on filter membrane and its variation with the applied flowrates. The experimental determination of permeability shown in this chapter consists of two steps: 1). Formation of the filter cake and 2). Flow of water through the filter cake. A detailed explanation of the two steps is given in section 5.3.

As already been mentioned one can expect a dependence of permeability on flowrate i.e. how the fluid is deformed. Moreover, for applications of microgel suspension as water based fluid loss additive that assists in forming a thin filter cake with very low permeability in oil reservoirs, it is important to study its mechanical properties. Several reports show that the viscosity of the drilling fluids increased a lot with the addition of the fluid loss additives like xanthum gum (Baba Hamed & Belhadri, 2009; Benchabane & Bekkour, 2006; Hamida, Kuru, & Pickard, 2009), polyacrylates, polyethylemine (Alemdar, Öztekin, Güngör, Ece, & Erim, 2005), polyacrylamides, guar gum, scleroglucan (Baba Hamed & Belhadri, 2009), carbopol (Kelessidis, Poulakakis, & Chatzistamou, 2011), polyvinyl alcohol (İşci, Günister, Ece, & Güngör, 2004) etc. A good additive should be viscous, thixotropic shear thinning fluids with yield stress (Coussot, Bertrand, & Herzhaft, 2004; Wakadikar, Sil, Kolekar, Tandon, & Kumar, 2011). This increase in viscosity drastically effects the liquidity of the drilling fluid hence, it is important to study their rheological properties.

5.3 Experimental Procedure

5.3.1 Set-up

We present here a leak-proof geometry, developed and built by Dr. Jeremy Decock, to measure the permeability of the microgel filter cake on a membrane filter as supporting base (Decock, 2017). The geometry consists of three parts:

A. One part contains the millifluidic channel that holds the microgel suspension which eventually forms the porous filter cake (**filter cake retention part**) (see Figure 5-2A)

B. One part consists of intermediate elements made up of a stack of membranes and the PC slab (**intermediate part**) (see Figure 5-2B)

C. One part serves as the passage for the filtrate (water) to the bin (**filtrate part**) (see Figure 5-2C)

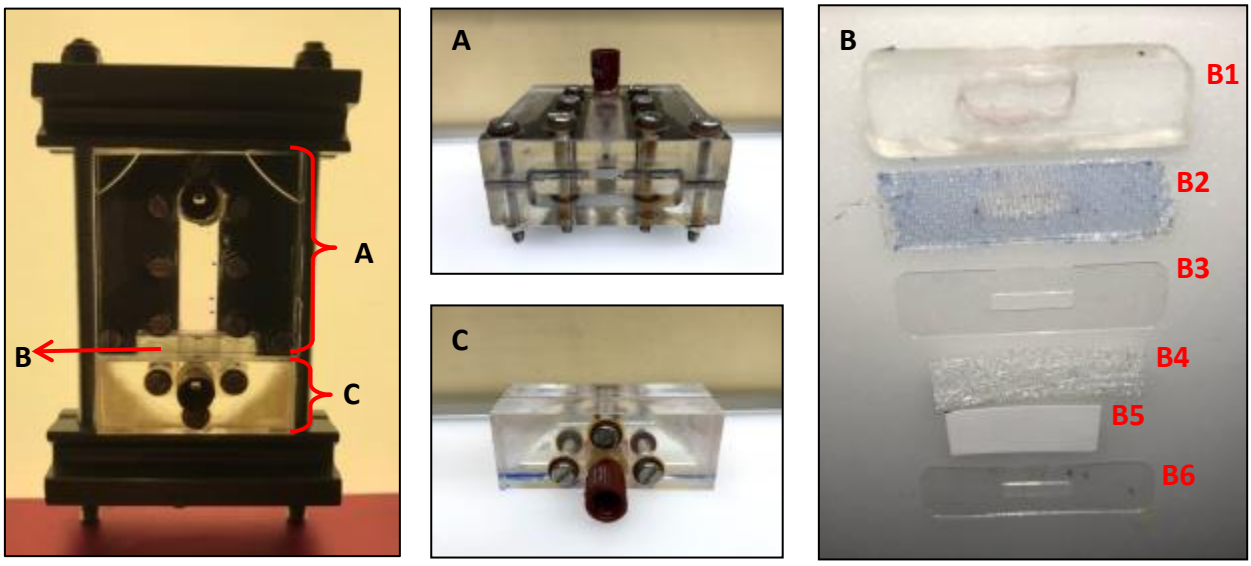

Figure 5-2 Millifluidic geometry used for the measurement of the permeability of porous filter cake. All the parts assembled in an Auminium (Left). (A) depicts the Filter cake retention part with the ports for input flow, and pressure sensor. This part has a black mask fixed in between the two PC blocks. The black mask (same as used for photolithography) helps to block the light and therefore avoids the saturation of the camera. In this case, we do not need it as we are not using the camera for further image analysis), (B) shows the intermediate part which is stack of membranes and PC slab with a hole (from B1 to B6) and (C) shows the filtrate part.

Filter cake retention part

The filter cake retention part (A) is made of 2 PC blocks with a channel on each assembled together with the help of 2 attaching membranes. These 2 PC blocks are attached to each other perfectly with the help of M2.5 screws of length 30mm. After the 2PC blocks are assembled, the final dimensions of the channel inside the block is 38mm x 10.2 mm x 2.1mm (Table 5-1). On the side of one of the PC blocks, there is an input connection (Luer-lock 1/ 4-28 Female) to flow the

fluid into the channel which is stuck to the PC block with the help of epoxy resin. The input connection is cut at the base to remove the Luer-lock portion and is inserted in the hole of adequate diameter to a depth of 6mm (see Figure 5-3).

Table 5-1 Table summarizing the dimensions of the channel where the filter cake is formed inside the PC blocks

Length, L_c (mm)	Width, W_c (mm)	Height, H_c (mm)	Surface area, A (mm^2)	Volume, V_c (ml)
10.2	2.1	38	21.4	0.8

The back side of the block has a secondary connection that connects the pressure sensor for measuring the pressure gradient through the porous filter cake for the constant flow experiments. The PC block is drilled to insert a nanoport connection from inside. This is done to avoid any risk of leakage and detachment of the connection as the pressure in system can be very high (up to 7 bars). The nanoport is glued to the PC block with the help of the epoxy resin.

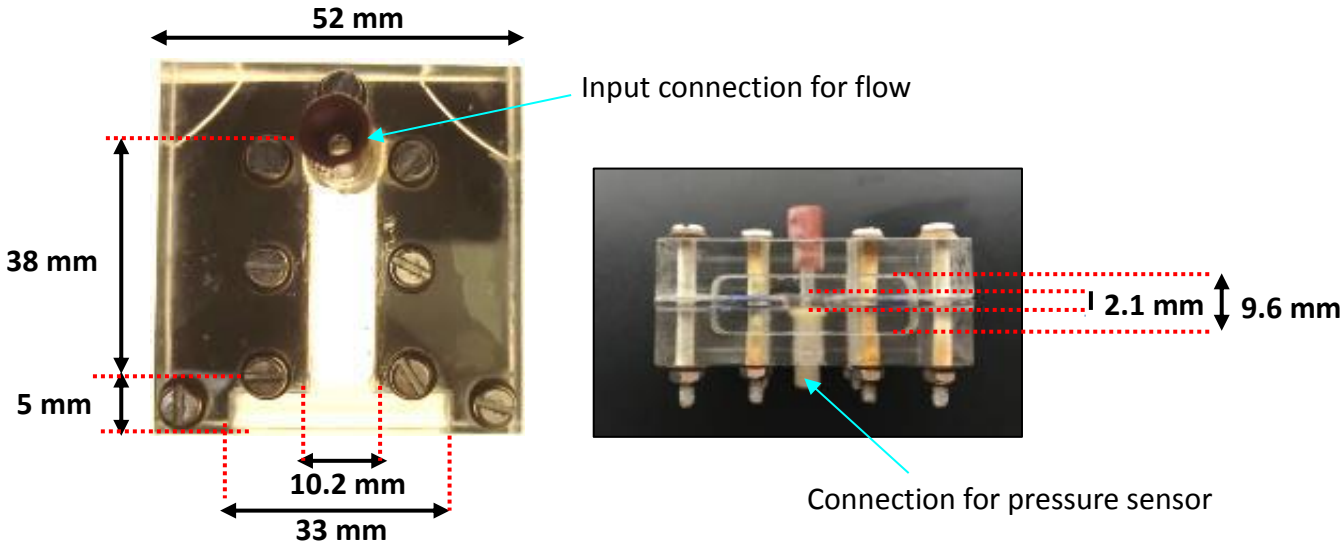

Figure 5-3 Picture showing the frontal and transverse section of the Filter cake retention part with its dimensions and the connections for the input flow and pressure sensor.

Filtrate part

The filtrate part (C) is assembled in accordance to the same principle as mentioned above. The filtrate part consists of two external 9.5 mm thick PC blocks, one with an output connector (Luer lock 1 /4-28 female) and the other with a nanoport glued to the block epoxy resin. The output

connection leads to a bin (maintained at atmospheric pressure) with the help of a tubing. The two PC blocks are assembled together with the help of screws M2.5 (see Figure 5-2C).

Intermediate part

The intermediate part (B) is the part with the most elements (check Figure 5-4). This part is crucial to avoid any leakage and also to provide mechanical support to the membrane filter. The elements starting from the filter cake retention part going to the filtrate part are as follows:

- A PDMS film (B6)
- The membrane filter, Whatman ® (B4 or B5)
- Second PDMS film (B3)
- Mesh (B2)
- A PC block of thickness 8mm (B1)

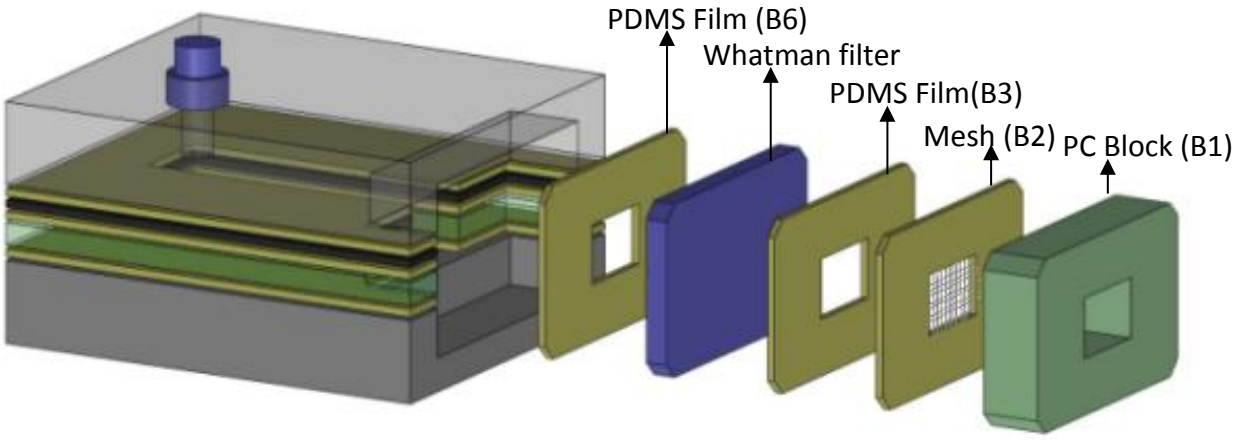

Figure 5-4 A pictorial representation of the stack of membrane, namely, PDMS Film (thickness 25 µm), Filter membrane(Whatman filter), Mesh (Solvay filter) and a PC block arranged in the order as used in the experiments along with the filter cake retention part.

The mesh and the membranes are cut to the dimensions 33 x 9.6 mm^2 and 31 x 8 mm^2 respectively. These dimensions fit perfectly to the indentation cavity. The PDMS film (thickness= 250 µm) ensures tightness of the system and avoids the membrane from slipping. The mesh provides mechanical support to the membrane. The frame is made of two aluminium blocks and two

stainless steel threaded rods. The Al blocks can move along the threaded rods for adjustments. When all the elements are in place the screws on the rods are tightened enough to have a leak proof system. The membrane filter (refer Table 5-2) is used as a support base for the filter cake to rest. The choice of the membrane filter's pore size is dependent on the average particle size of the suspension used as we do not want the particle to pass through the membrane. We use Membrane_1 (see Figure 5-5a) as a base for Microgel2000-10 and Microgel4000-10 while Membrane_5 (see Figure 5-5b) is used for Microgel-IN. A highly permeable mesh (Solvay®) provides mechanical support to the membrane filter (as the pressure in the cell can rise upto 7 bars) without blocking the flow of the fluid. The PMMA block offers more mechanical support and a passage for the filtrate to flow to the bin.

Table 5-2 Table presenting the membrane filter used as a supporting base for the porous filter cake with the pore size and thickness.

	Pore size (µm)	**Thickness (µm)**	**Name given**
Whatman Nylon Membrane filter	1	100	Membrane_1
Whatman TE38 (PTFE supported) filter	5	700	Membrane_5
Mesh	NA	460	Mesh

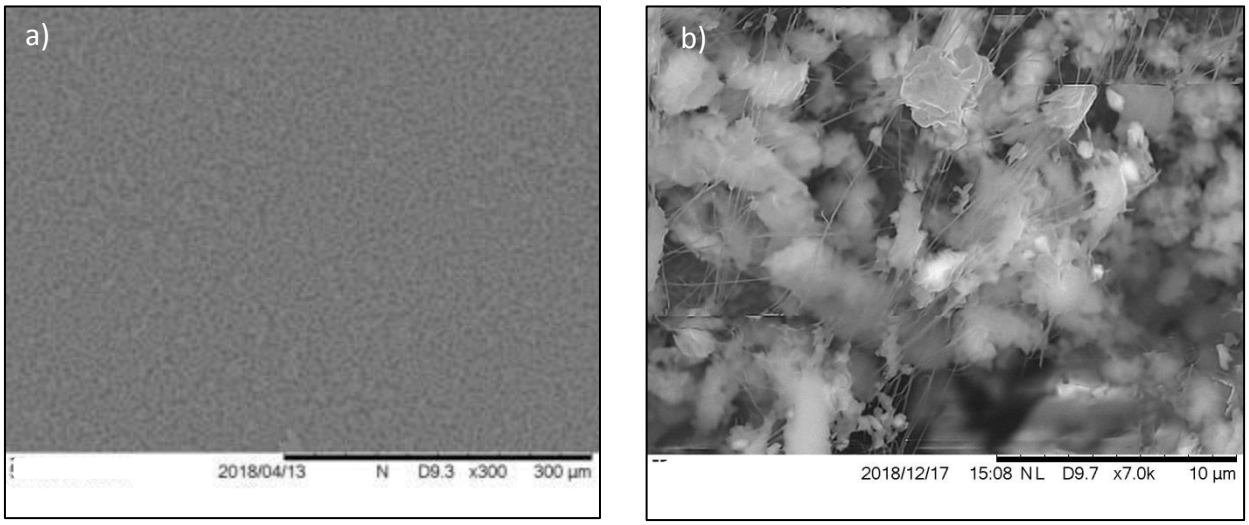

Figure 5-5 SEM micrographs of the membrane filters, a). Pore size= 1µm and, b). Pore size= 5µm

For the flow experiments, the input connection of the PC block is connected to a 50ml syringe (Gastight, Hamilton) with a 1/8th PFA tube (ID 2.4 mm). The syringe is positioned on a syringe

pump (Harvard PHD 4400) which controls the flowrate. The output is connected to a beaker which for the filtrate. An analog pressure sensor of 100 psi is connected to the nanoport of the filter cake retention part. The sensor delivers a voltage that is measured by the computer via an acquisition card and software (MATLAB ®).

5.3.2 Calibration of the Pressure sensor

Before taking the measurements, it is important to ensure the correctness of the pressure data from the pressure sensor, hence we calibrate the pressure sensor using a pressure controller (7 Bar, Fluigent MFC). The sensor converts the voltage signal to pressure. We applied an input pressure using pressure controller and recorded the output by the sensor as a function of time using Arduino card and MATLAB data acquisition tool at 10Hz. The data obtained is shown in Figure 5-6). We estimated the error to be less than 6% between the input pressures applied and the output pressure measured.

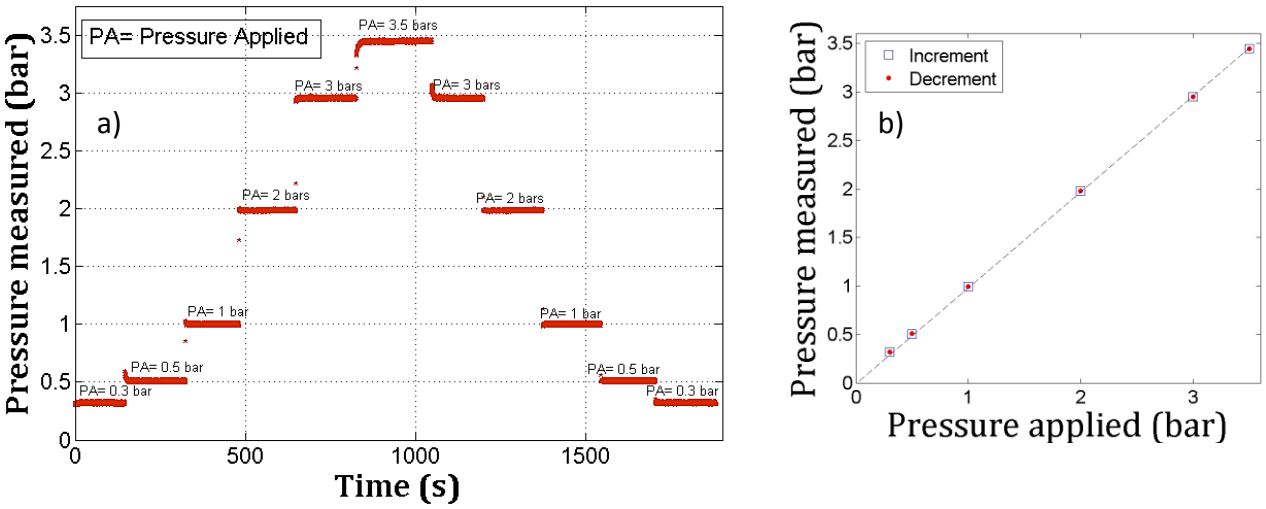

Figure 5-6 (a) Typical plot for pressure measured for applied pressures using pressure controller by Fluigent and (b) displays the linear curve of the measured pressure versus applied pressures.

5.3.3 Formation of the Filter Cake

The Microgel suspension filter cake is formed by a method of compression at room temperature. We first put together the parts A, B and C of the geometry as mentioned in Section 5.3.1 to ensure no leakage. We close the nanoport for the pressure sensor of the cell with a plug and then fill the cell with microgel suspension (1.8% wt. Microgel4000-10 and Microgel2000-10 and 2% wt.

Microgel-IN) upto a quarter of the volume of the channel. The rest of the volume of the cell is filled with deionized water using a 3ml syringe (VWR) fitted with a long needle (Note: care was taken to avoid air bubbles and to unduly disturb the already placed suspension). Deionized water was then injected by a 2.5ml syringe (Gastight, Hamilton) with a downwards flow at a constant flowrate, Q= 100µl/hr for 15 hrs using a syringe pump through the channel to form the filter cake of microgel on to the filter membrane (see Figure 5-7). This total volume of 1.5ml ensures that there is enough water to push the microgel suspension into forming a filter cake on the membrane (Figure 5-8). The filter cake formed is quite densely packed as can be seen in the phase contrast micrograph in Figure 5-9.

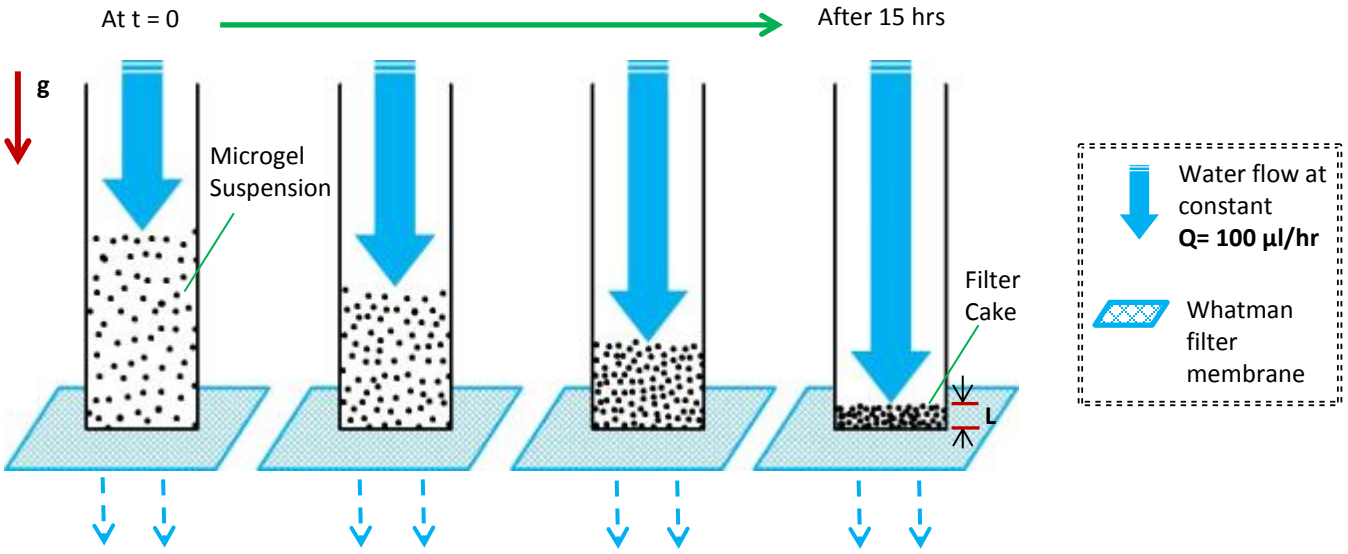

Figure 5-7 Schematic showing the formation of the filter cake of Microgel suspension on a membrane which is permeable to fluid but not solid by flowing water at Q= 100µl/hr (downwards) in the PC Millifluidic cell

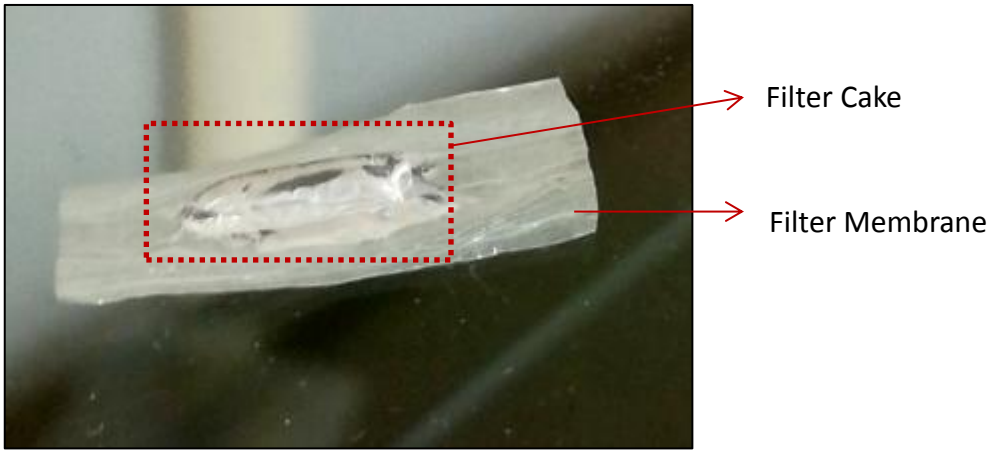

Figure 5-8 Picture of the actual filter cake of Microgel4000-10 formed on 1µm Pore size Whatman filter membrane.

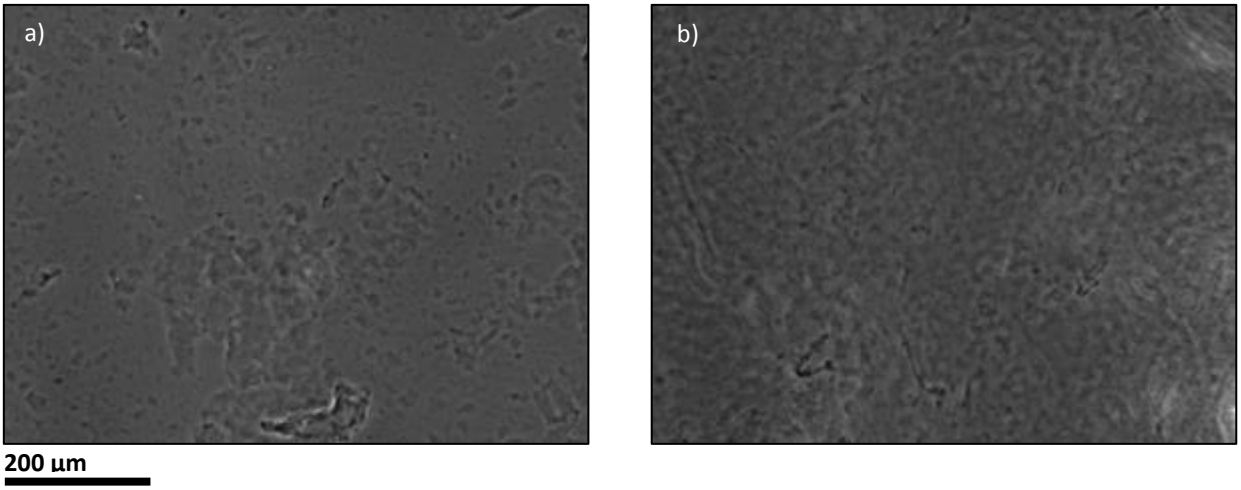

Figure 5-9 Phase contrast images of (a). 2% wt. Microgel-IN and (b) the dense filter cake formed from Microgel-IN

5.3.4 Measurements

I. Permeability measurements

The membrane permeability measurement is simple and is done by flowing water at different flow rates though the membrane filter using the syringe pump and measuring the corresponding steady state pressure gradient in the channel using the pressure sensor.

However, for the case of microgel filter cake, we first form the porous filter cake using the method as mentioned in section 5.3.3. After this, we start the measurements by injecting de-ionised water at a constant flowrate, Q= 100µl/hr until the pressure reaches 6-7 bars. This is done to subject

the filter cake to the same pressure conditions in which it is formed. We then start decreasing the flowrate and take the corresponding steady-state pressure readings. Since, the filter cake is a deformable porous media, care was taken to work in the low flowrate regimes so as to not excessively deform the filter cake.

The permeability, $\mathcal{K}$ is calculated using the equation below:

$$\boldsymbol{\mathcal{K}} = \frac{\boldsymbol{\eta\, L}}{\boldsymbol{A}*(\frac{\boldsymbol{\Delta P}}{\boldsymbol{Q}})} \tag{5-c}$$

where, $\frac{\Delta P}{Q}$ is the slope of the ΔP versus Q plot obtained from curve fitting, A is the area of cross section of the filter cake (same as the cross section of the channel) and η is the viscosity of the fluid (i.e. water in this case) = 0.99 mPa s (as measured in chapter 2).

II. Rheology of Microgel filter cake

The rheological measurements were performed on the filter cake using commercial rheometer (Malvern Ultra+) with a sand blasted parallel plate geometry of diameter 40mm and a gap of 100µm. Oscillatory shear measurements, shear ramp tests with logarithmic ramp up from 0.001 s^{-1} to 10 s^{-1} and normal force measurements were performed on the filter cake. Since the volume of the filter cake recovered is quite small, it wets only a small area of the parallel plate geometry.

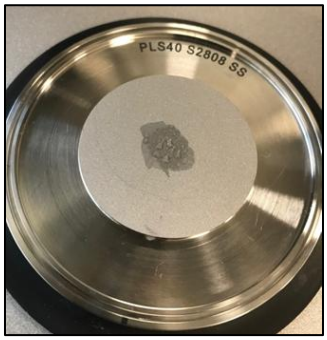

Therefore, all the stress, strain and shear rates values measured by the rheometer were corrected using the relation given below:

$$\sigma = \frac{2M}{\pi\, R_{Real}^3} \tag{5-d}$$

$$\gamma = \frac{\theta\, R_{Real}}{h} \tag{5-e}$$

$$\dot{\gamma} = \frac{\dot{\theta}\, R_{Real}}{h} \tag{5-f}$$

where, M is torque measured by the rheometer (Nm), θ is the angular displacement, $\dot{\theta}$ is the angular velocity, h is the distance between the plates and R_{Real} is the true radial dimension of the filter cake, as measured from the observed wetted area on the plate geometry at the end of the experiment.

We also performed rheological measurement in compression by squeezing the filter cake between two parallel plates and recording the normal force vs gap. Normal force measurements were performed on all the three filter cakes using the same geometry. measurements were performed rather slowly with the upper plate moving at a speed of 1 µm/s from a gap of 500 µm to 10 µm. Throughout each step, we monitor the evolution of normal force as a function of gap distance.

5.4 Results

5.4.1 Permeability

I. Permeability of membrane filter and mesh

The permeability is calculated using Darcy's equation for the flow of water through the already formed filter cake/membrane from the graphical plot of steady state pressure against volumetric flowrate.

Figure 5-10 (a,b) displays a typical plot of volumetric flowrate against the pressure through Membrane_5 and Membrane_1. A small pressure offset is seen in all measurements and it is assumed to be due to the resistance of the filter. This offset has been deducted from the data. As can be seen in each case, the pressure follows a fine linear variation with flowrate indicating a laminar flow in the cell. For the range of flowrates used, the fluid flow follows Darcy's flow regime.

The linear fit is found to be quite good with R^2=0.98 for Membrane_5 and is 0.99 for both Membrane_1 respectively.

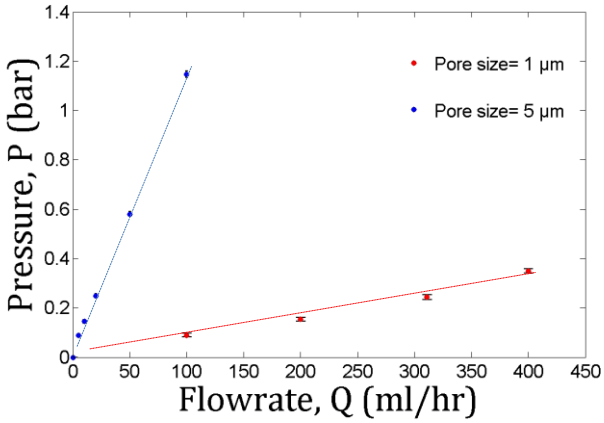

Figure 5-10 Plot of volumetric flowrate against the pressure build up on the filter membrane (1µm and 5µm).

The linear fitting gives the value of the slopes as 0.0097 and 0.0008 bar/(ml/hr) for Membrane_5, Membrane_1 respectively. Using this data along with A, thickness (as mentioned in Table 5-2) and η values (as given in 5.4.1), the permeability $\mathcal{K}$ calculated for Membrane_5, and Membrane_1 respectively are given below.

Permeability , $\mathcal{K}$= 9.3 x 10^{-15} m^2 or 0.0095 Darcy for **Membrane_5**

16 x 10^{-15} m^2 or 0.0165 Darcy for **Membrane_1**

Given the different pore size of the membranes, the permeability is almost same for membrane. This is believed to be due to different porosity (ϕ_p) of the membranes. Using equation 5-a along with the values of permeability and pore size of Membrane_1 and Membrane_5, we calculate the porosity (ϕ_p) as shown below.

Porosity , ϕ_p= 7 % for **Membrane_5**

25% for **Membrane_1**

Clearly, the membrane with the smaller pore size (Membrane_1) has higher porosity than the membrane with the higher pore size (Membrane_1) which explains the almost same permeabilities.

II. Filter Cake Permeability

After the filter cake has been formed (as explained in section 5.3.3), the flow experiments were carried out to measure the permeability of the microgel filter cake. The system is first subjected to a very high pressure (6-7 bars) by the application of a flowrate, Q= 100µl/hr. Once the pressure reaches ~6 bars (to avoid saturating the sensor), we decrease the flowrates and measure the corresponding pressure gradient in the steady state. As an example, we show in Figure 5-11, the typical raw data which illustrates the temporal evolution of pressure under flow for various flowrates for the case of 2% wt. Microgel-IN. To check the accuracy of the experiments, we repeated the measurements twice for Microgel-IN only. Measurement for the other microgel system were performed only once since for these measurements and especially at lower flowrates, the pressure may take as long as 3-4 days to stabilize leading to a total run time of around 15 days. The stabilization period for the pressure is seen to increase with decrease in the applied flowrates, as might be expected.

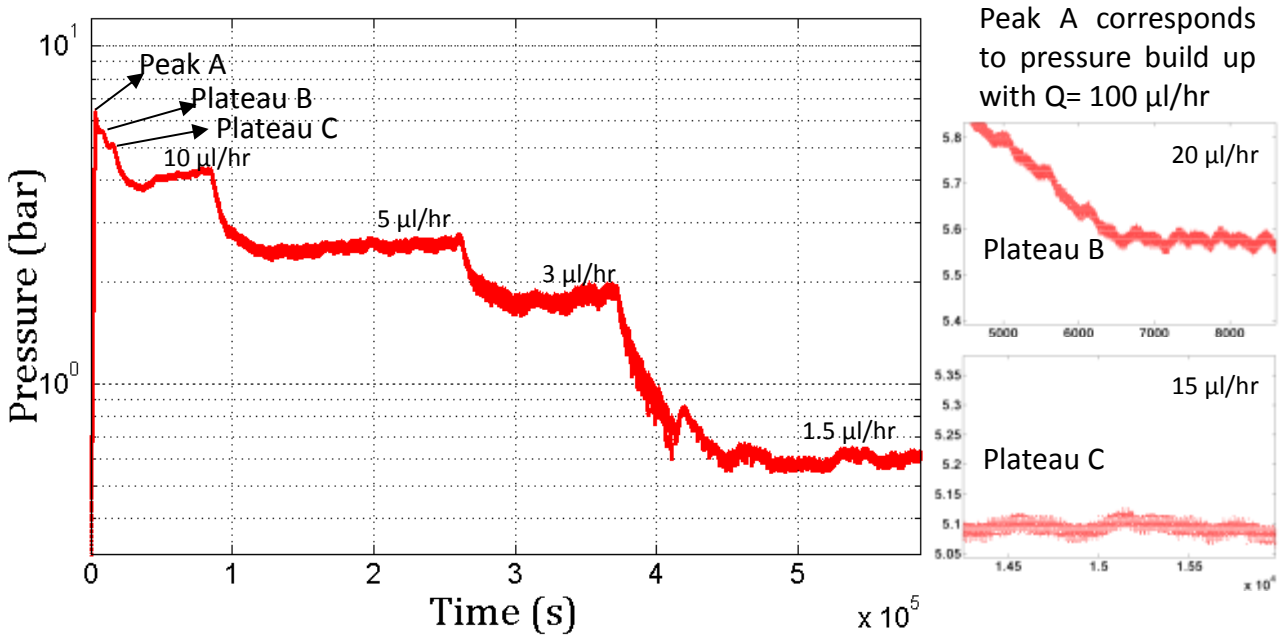

Figure 5-11 Typical Raw data curve we get from the measurements depicting the temporal evolution of the pressure across the cell under different flowrates applied.

The steady-state pressure values for each flowrate extracted from the raw data are displayed in Figure 5-12, 5-13 and 5-14 for Microgel-IN, Microgel4000-10 and Microgel2000-10 respectively.

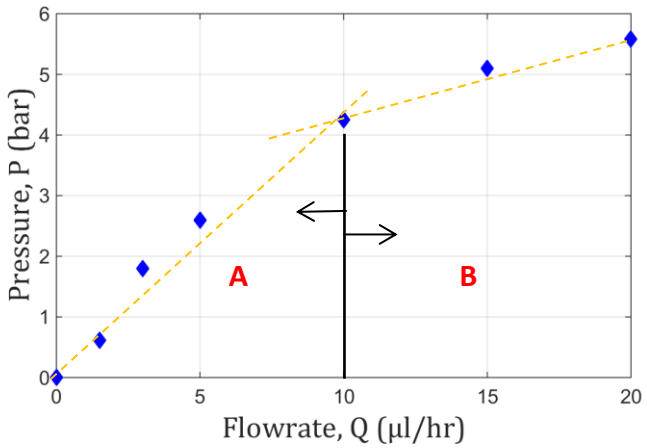

Figure 5-12 Pressure versus flowrate, Q (on µl/hr) for Microgel-IN filter cake

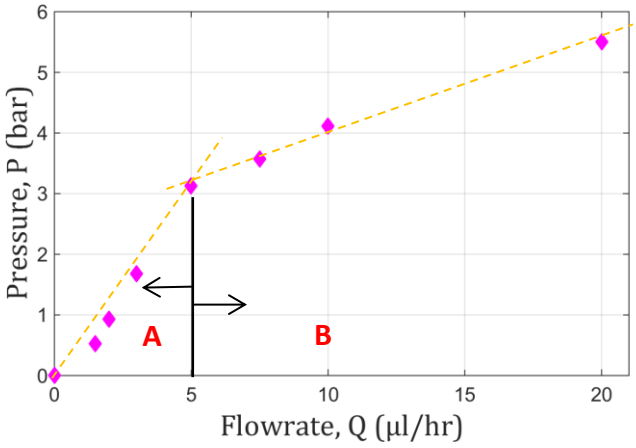

Figure 5-13 Pressure versus flowrate plot for filter cake of Microgel4000-10

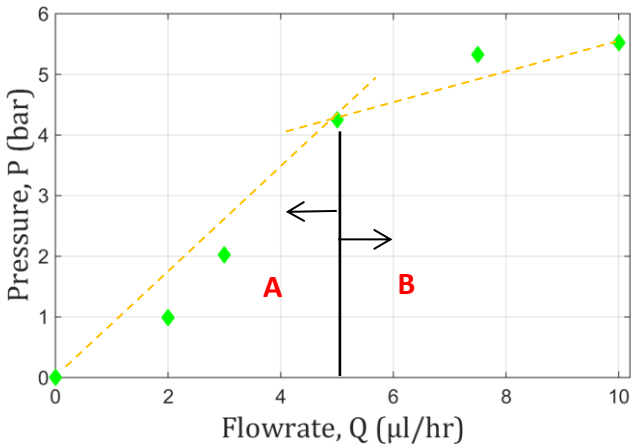

Figure 5-14 Pressure versus flowrate curve of filter cake of Microgel2000-10

We clearly see a significant decrease in the value of slopes at higher flowrates. The values of the slopes in region A and B of the plots are summarized in the Table 5-3. This appreciable departure from the linear regime occurred at Q= 5µl/hr for Microgel4000-10 and Microgel2000-10 and at Q= 10 µl/hr for Microgel-IN is believed to be due to the deformation of the deformable microgel filter cake as result of the high pressure gradient. We speculate this is due to deformation causing holes in the filter cake or non-uniform thickness of the filter cake causing the fluid to pass easily through the filter and therefore causing a gradual rise of pressure at higher flow rates.

Table 5-3 Table summarizing the values of the slope as calculated from the Pressure gradient versus Flowrate curves in both region A & B for Microgel-IN, Microgel4000-10 and Microgel2000-10.

	Slope (= $\frac{\Delta P}{Q}$) (bar/(µl/hr)	
	Region A	**Region B**
Microgel-IN	0.454	0.133 (with y-intercept= 2.982)
Microgel4000-10	0.579	0.150 (with y-intercept= 2.524)
Microgel2000-10	0.771	0.254 (with y-intercept= 3.128)

Since Darcy's law is applicable only in the linear regime, we use the slopes of the curve in region A to evaluate the permeability of the filter cake. Using c_0 , L_0 , m_f and m_0 as the initial concentration, initial microgel suspension height, mass of filter cake formed and the initial mass of the microgel injected in the cell respectively, we can easily calculate the thickness of the filter cake, L, (assuming that there is no significant deformation or mass loss from the suspension through the membrane i.e. the volumetric mass remains constant) as:

$$L = \frac{L_0 * m_f}{m_0} \tag{5-g}$$

Here, m_f is measured by weighing the membrane with the filter cake and without (after scraping off the filter cake) using a sensitive weighing balance and subtracting both the masses.
Also, assuming that the mass of the polymer is conserved i.e. no microgel particles pass through the membrane, we can estimate the amount of water removed from the microgel suspension to get the final filter cake. The concentration c_f of the filter cake is then given as:

$$c_f = \frac{c_0 * m_0}{m_f} \tag{5-h}$$

Another method to measure the concentration of the filter cake is to perform dry mass measurements (refer section 1.3.3) on it. After the permeability measurements, the cell is opened, the filter membrane with filter cake stuck on it is removed carefully. The microgel filter cake is scrapped off from the membrane using a spatula. The filter cake is then dried at high temperature inside IR Moisture Analyser (Model IR 60, Denver Instruments) (see 1.3.3) which records the mass

before and after drying and give the total dry mass. The estimated final concentration (c_f) by these methods is presented in Table 5-5. The c_f directly measured by dry mass measurements are similar for the three microgel suspensions i.e. around 12% wt., whereas the indirect method shows that the Microgel-IN filter cake is much more concentrated then Microgel2000-10 and Microgel4000-10. The source of this huge error is actually the filter cake left over on the membrane filter or stuck in the pores while scraping off the cake for weighing to estimate c_f using the Equation 5-h. Another reason is the mass loss from the microgel suspension through the filter membrane due to its high pore size. However, this scraping off have no effect as the concentration is believed to be uniform in the filter cake. This makes dry mass measurements, a more reliable method to evaluate the final concentration of the filter cake. This concentration of the filter cake can be thought as the concentration for maximum packing of the microgel particles.

Table 5-4 Table comparing the concentration of the filter cake calculated by two methods, firstly, using the relation, $\boldsymbol{c_f = \frac{c_0 * m_0}{m_f}}$ and then the dry mass measurements

	Using $\boldsymbol{c_f = \frac{c_0 * m_0}{m_f}}$	Using dry mass measurements	% Error in final concentration	Thickness, L (mm) (using $\boldsymbol{\frac{L_0 * m_f}{m_0}}$)	Thickness, L (mm) (calculated using dry mass)
Microgel-IN	20	12.6	57.5	0.64	1.01
Microgel4000-10	9.1	12.1	24.8	1.65	1.24
Microgel2000-10	9.5	12.3	22.8	2.12	1.73

Using the thickness, L (as calculated using $\frac{L_0 * m_f}{m_0}$) and the viscosity, η, we estimate the permeability of the filter cake as 1.4 x 10^{-7} ± 2 x 10^{-9} Darcy or 1.4 x 10^{-19} ± 2 x 10^{-21} m^2 for Microgel-IN. The small deviation in the estimated permeability of Microgel-IN filter cake indicates that the technique used here is accurate, reproducible and gives a precise measurement of permeability. For Microgel4000-10 and Microgel2000-10, the permeability is calculated to be 3.8 x 10^{-7} Darcy or 3.7 x 10^{-19} m^2 and 3.7 x 10^{-7} Darcy or 3.6 x 10^{-19} m^2 respectively. Similarly, using this dry mass measurement for each microgel filter cake, we back calculate the thickness (L) of the filter cake and use it to calculate the permeability. The values are found to be 2.4 x 10^{-19}, 3.3 x 10^{-19} and 3 x 10^{-19} m^2 for Microgel-IN, Microgel4000-10 and Microgel2000-10 respectively. Such low permeability is often observed impervious materials such as granite rock which has permeability

values typically between 10^{-19} to 10^{-22} m^2. Also, by a simple comparison of permeability calculated in region A for each case, one can simply conclude that in cases with low permeability, the viscous regime persists till relatively higher flowrates (Wyckoff et al., 1933) thereby explaining the departure from viscous regime occurs at Q= 10µl/hr for Microgel-IN but at Q= 5µl/hr for Microgel4000-10 and Microgel2000-10.

Table 5-5 Table depicting the values of permeability for Microgel-IN, Microgel4000-10 and Microgel2000-10 as calculated using Darcy's law.

	Permeability, $\mathcal{K}$ (m^2) using L= $\frac{L_0 * m_f}{m_0}$	**Permeability, $\mathcal{K}$ (m^2) using L calculated from dry mass**
Microgel-IN filter cake	1.4 x 10^{-19}	2.4 x 10^{-19}
Microgel4000-10 filter cake	3.7 x 10^{-19}	3.3 x 10^{-19}
Microgel2000-10 filter cake	3.6 x 10^{-19}	3 x 10^{-19}

From Table 5-6, it can be seen that the permeability estimation for Microgel-IN using different thicknesses is lower than the values for Microgel4000-10 and Microgel2000-10. This is perhaps because of the polydispersity of the suspension which results in accommodating more deformable particles in a small volume.

Now, setting D_p =20 µm, we compute the magnitude of the porosity using the values of permeability calculated using dry mass in the Carman-Kozeny equation.

ϕ_p= 0.1% for **all cases**

The low value of ϕ_p is consistent with the dense array of deformed particles as assumed when we say that 12% wt. (which is the maximum concentration) of the particles is equal to 100% of the volume occupied.

5.4.2 Rheology of Filter Cake

I. Linear viscoelasticity of the filter cake

The strain dependence of the storage (G') and the loss modulus (G'') was measured for each filter cake at frequency 1Hz. For example, in Figure 5-15 we show the linear viscoelastic behaviour of Microgel-IN filter cake (the values have been corrected to take into account the filter cake contact area on the plate). The filter cake is found to be predominantly elastic with G'>G'' and a constant for the all the strain used in the measurements indicating a linear regime characteristic of a highly elastic cross-linked closed packed network. The values of G' and G'' along with the concentration of each filtercake are given in the Table 5-7. A quick comparison the G' and G'' of the filter cake with the values given in (refer Figure 2-26 in chapter 2) indicates that even though the difference between the values of G' and G'' was increasing with concentration for Microgel-IN, Microgel4000-10 and Microgel2000-10, there is one point where this difference reduces to zero i.e. G'=G'' and beyond that the elastic behaviour dominates. The filter cake formed in these experiments lie beyond critical concetration as we have already seen in the dry mass measurements.

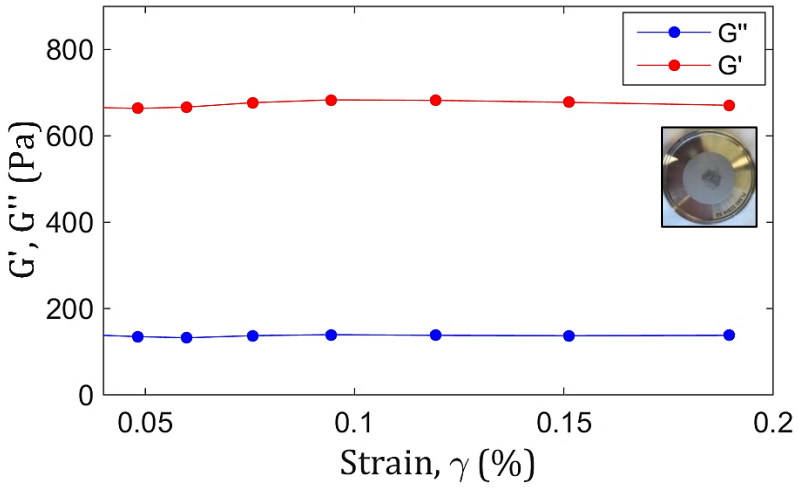

Figure 5-15 Plot of elastic modulus, G' and Viscous modulus, G'' as fucntion of strain at a constant frequency of 1 Hz for Microgel-IN.

II. Shear flow measurements

We measure the flow behaviour of the microgel filter cake in shear ramp tests with logarithmic ramp up from 0.001 s^{-1} to 10 s^{-1}. The shear stress and shear rates are corrected keeping in mind the area of the parallel plate wetted by the filter cake. Figure 5-16 displays the flow properties of the Microgel-IN filter. The flow curve indicate shear thinning behaviour with the filter cake of Microgel-IN possessing a yield stress. A similar behaviour was also observed for Microgel4000-10 and Microgel2000-10 filter cakes. The concentration of the filter cake represents the c_m of the microgel suspensions. From the flow curve, the yield stress, σ_y, is found to be 26 Pa, 20 Pa and 23 Pa for Microgel-IN, Microgel4000-10 and Microgel2000-10 respectively. Although, not very high, this yield stress prevent the filter cake to flow and just jam the porous structures once it is formed as we have seen in the previous chapter 4.

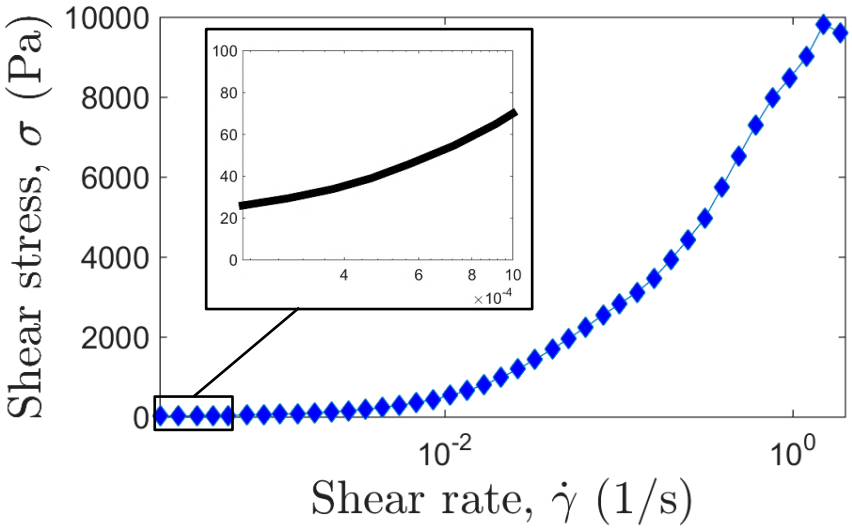

Figure 5-16 Typical flow curve depicting the Shear stress (corrected values)- shear rate dependence of Microgel-IN filter cake.

The un-corrected results from bulk rheology were found to be quite reproducible. With corrections i.e taking into account the wetted area, the value of the yield stress, elastic and viscous modulus are presented in Table 5-7.

Table 5-6 Table summarizing the rheological measurements, G' and G'' along with the yield stress of the filter of the microgel formed in the cell for the permeability measurements.

	Concentration of the filter cake, c_f (% wt.)	**Radius wetted (mm)**	**G' (Pa)**	**G'' (Pa)**	**σ_y (Pa)**
Microgel-IN filter cake	12.6	~ 5.5	682	140	26
Microgel4000-10 filter cake	12.1	~ 6	501	111	20
Microgel2000-10 filter cake	12.3	~ 6	501	108	13

III. Squeeze flow measurements

We performed the squeeze flow measurements on the microgel filter cake using the rotational rheometer (Malvern Ultra+)(see section 1.3.4). When the material is compressed between two plates, it undergoes squeezing flows in radially outward direction due to the change in the geometry and inhomogenous flows (see Figure 5-17). It gives information about the elastic behaviour of the material.

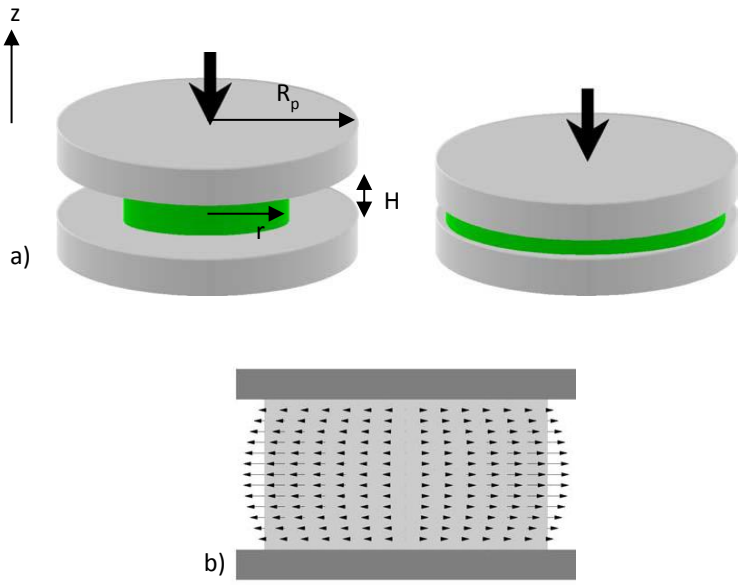

Figure 5-17 (a) Pictorial representation of axisymmetric squeeze flow with constant mass of sample between the plates, (b). Velocity fields and velocity component fields for squeeze flow with no slip (Engmann, Servais, & Burbidge, 2005).

The working equations can be very easily derived assuming no slip condition and boundary condition that the volume is conserved (Engmann, Servais, & Burbidge, 2005). The equation is

valid only in the elastic regime. The small change in force, F as the gap between the plates changes by $\boldsymbol{\delta h}$ is given as

$$\delta F = \frac{\pi R^4 \delta h}{2h^3} \times G' \tag{5-i}$$

Integrating as the gap changes from h_0 to h

$$F(h) = \int_{z=h_o}^{z=h} \frac{\pi G' R^4(z) dz}{2 z^3} \tag{5-j}$$

We get

$$F(h) = -\frac{\pi G' R_0^4 h_0^2}{8}\left(\frac{1}{h_0^4} - \frac{1}{h^4}\right) \tag{5-k}$$

where, G' is the elastic shear modulus, $h(t)$ is the gap at any time, t, h_o is the initial thickness of the sample (when the force, F_z starts to be non zero) and R_0 is the initial radius at h_0. Figure 5-18 displays the normal force versus gap between the parallel plates for Microgel-IN filter cake.

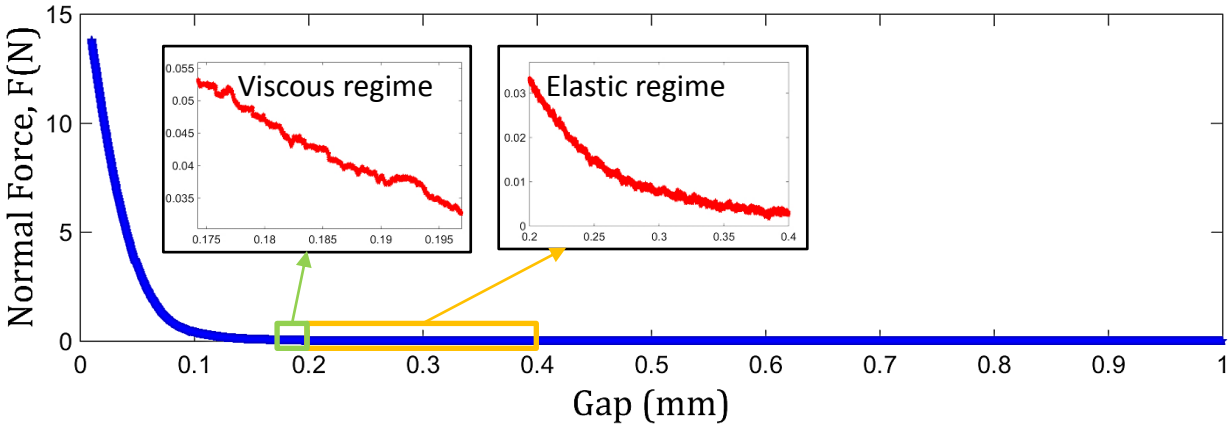

Figure 5-18 Plot of Normal force measured as a function of gap between the two parallel plate geometry (starting from 1mm and going till 10 µm) for the filtercake formed for Microgel-IN.

At gap= 1mm, the Microgel-IN is found to wet an area which corresponds to a radius, R_0= 1.5 mm on the parallel plate. For Microgel-IN, as the gap between the plates starts to decrease, no normal

force is measured (which means there is no change in the radius) until at height, h= 0.4 mm when the normal, F_z suddenly starts to become non-zero, while the filter cake stays in the elastic regime. However, as the gap decreases beyond 0.2mm the microgel filter starts behaving as a viscous fluid. Since, the equation we use for normal force is valid in only the elastic regime, we fit this curve it to the normal force measurements between gap 0.4 to 0.2 mm using curve fitting tool (MATLAB®)(see Figure 5-19). It would be possible to describe the viscous regime too, but this is beyond the scope of this manuscript.

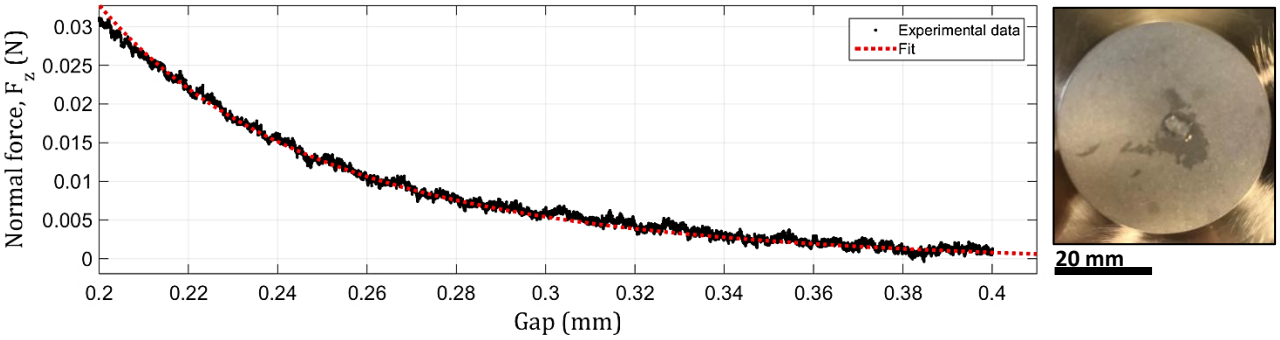

Figure 5-19 Typical plot of normal force measured between parallel plates for filter cake of Microgel-IN as the gap changes from 0.4 to 0.2 mm. The red line represent the fit corresponding to equation

We can see that the fit for equation to the experimental data is pretty good (R^2 =0.99). The fitting tool returns the free fitting parameter,elastic modulus, G' as 57.2 Pa. We follow the same procedure to for the equation to the force curves for Microgel4000-10 and Microgel2000-10 filter cakes. The elastic regime in these two cases was found between gap 0.2 to 0.4/0.42 mm. From the fitting, we obtained the elastic modulus, G' as 48.4 Pa and 41.4 Pa for Microgel4000-10 with R^2=0.99 and Microgel2000-10 with R^2= 0.97 for the $R_0 \sim$ 2.1 mm for both. The value of the elastic moduli for all three filter cakes are summarized in Table 5-7.

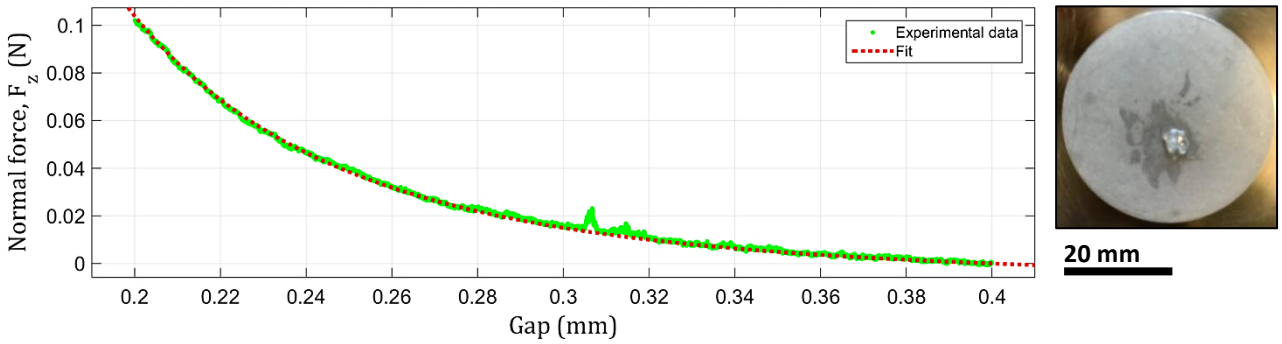

Figure 5-20 Typical plot of normal force measured between parallel plates for filter cake of Microgel4000-10 as the gap changes from 0.4 to 0.2 mm. The red line represents the fit. The initial radius is taken as 2.1 mm.

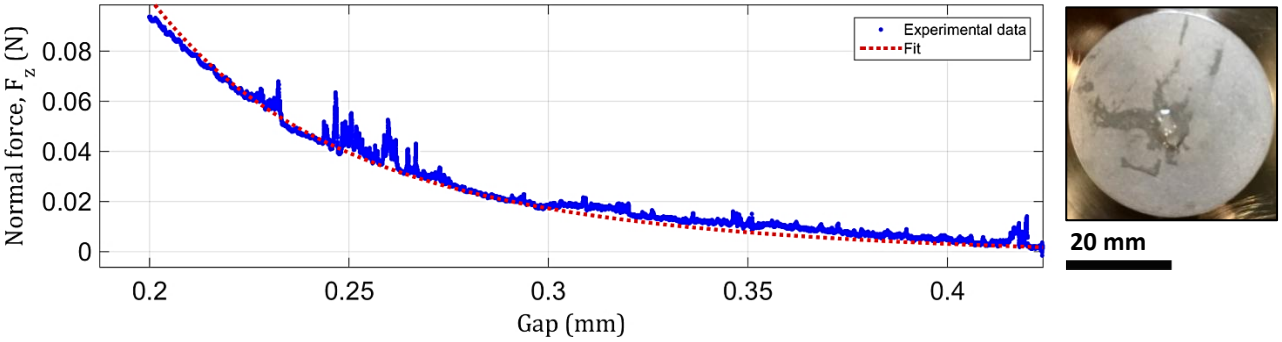

Figure 5-21 Typical plot of normal force measured between parallel plates for filter cake of Microgel2000-10 as the gap changes from 0.42 to 0.2 mm. The red line represents the fit. The initial radius is 2.1 mm.

Table 5-7 Table summarizing the values of elastic modulus obtained from fitting the normal force versus gap for Microgel-IN, Microgel4000-10 and Microgel2000-10 filter cakes between two parallel plates.

	Elastic Modulus, G' (Pa)
Microgel-IN	57.3
Microgel2000-10	48.4
Microgel4000-10	41.4

Howewer, the results from the squeeze flow measurements are not consistent with the results from the oscillatory measurements. This is probably because the geometry of the sample is not well known and also at small gaps, the gap is not accurate. All computations done for the fit depend strongly on the assumed gap and radius. To conclude, squeeze flow measurements

provide an easy and quick method to characterize the rheology of filter cake if one can precisely recompute the sample dimensions until the 2 measurements are in agreement.

5.5 Conclusions and Perspectives

In this chapter, we presented an experimental technique to estimate the permeability of dense microgel filter cake on a supporting membrane. We show a method of forming the filter cake of microgel suspension on a membrane filter steadily. The membrane filters used in this chapter have small pore sizes of 1 and 5 μm. We showed the applicability of Darcy's law in the linear regime to calculate permeability of even deformable porous media. The membranes are found to be highly permeable with permeability of the order of 10^{-15} m^2, which means that these membranes do not obstruct the flow of the fluid while the filter cake is formed by the method of compression and eventually does not have any significant impact on the measurement of permeability of the microgel filter cake. In case of microgel, we observed that the relationship between pressure gradient and flowrates deviates from the linear regime at higher flowrates. This behaviour is believed to be due to the deformation causing holes in the deformable filter cake pointing to crucial role of lower flowrates in evaluating accurate values of permeability. To measure the thickness and concentration of the filter cake, we use dry mass measurement and a simple method taking in account the mass of the water lost from the suspension while forming the filter cake. We found dry mass measurement to be a more reliable method. Using the thickness of the filter cake calculated from the dry mass measurement, we evaluate the permeability, $\mathcal{K}$ for the filter of Microgel-IN as $2.4 \times 10^{-19} \pm 10^{-21}$ m^2. The small standard deviation in the value shows the precision and reproducibility of the technique for the permeability measurement. Similarly, the value of permeability is found to be 3.3×10^{-19} m^2 and 3×10^{-19} m^2 for Microgel4000-10 and Microgel2000-10 respectively. Such low permeability have been reported for rocks like granite implying the very impervious nature of the filter cake for the flow of water. The gap between the particles in the filter cake is seen to lie between 10-100 nm using Kozeny-Carman equation (assuming very low porosity) indicating how densely packed the filter cake is. The bulk rheological measurements show that the filter cake is highly elastic with yield

stress of the order of 10 Pa for all microgels. The results from squeeze flow measurements also throw light on the elastic behavior of the filter cake.

Concluding Remarks and Future Outlook

This thesis dealt with the understanding the jamming of soft dilute deformable microgel suspensions in model porous media in form of porous microfluidic channel and the parameters that affect this jamming. This complete understanding of the mechanism of jamming is achieved by:

a. Transforming the highly polydispersed industrial suspension to a more model suspension with a well defined particle size distribution by controlling the polydispersity with the help of a non-destructive technique.
b. Developing a method to achieve higher concentration of the suspensions without destroying the inherent structure and properties of the particles.
c. Understanding how concentration affects the size distribution of the suspesnions and predicting the critical concentration above which aggregates start to form, from the size distribution.
d. Performing rheological measurements over a range of concentrations of the microgel suspensions and predicting the accurate rheological model that describe their flow behaviour and estimating the jamming concentration.
e. Validating the jamming concentration as obtained from bulk rheology, with the help of simple optical method during the confined drying of the droplet of microgel suspension and understanding the effect of confinement on the jamming.
f. Interpreting the jamming of porous media for frontal filtration with the help of shear induced aggregation phenomenon and identifying the critical conditions in terms of concentration, particle size, pore size and flowrates that affect jamming.
g. Demonstrating fluid loss in porous media for lateral filtration.
h. Estimating the permeability of the jammed microgel 'filter cake' with the help of Darcy's law.

We now summarize the key results obtained in this work and provide suggestions for future work in this field.

Concluding Remarks

Owing to the polydispersity and inhomogeneity of the industrial suspension, it is a challenging task to turn the suspension into a more model suspension with a control over the particle size. We have been able to control the size of the particle by getting rid of the bigger particles using centrifugation, which is seen to work best without destroying the particles The average particle size changed from 105 to 27 µm and 13 µm with a narrower width of the distribution. The rheological and particle size measurements both indicate that above a concentration of 2% wt. for the centrifuged microgel suspension, aggregates starts forming because the already sticky particles come closer as the concentration rises and stick with each other to form the aggregates. The flow behaviour is seen to be very well described by power law model upto a certain concentration. Beyond this concentration the centrifuged microgel is seen to have a yield stress and is described by Herschel-Bulkley model. This concentration is 7.5% wt., 7% wt. and 3.3% wt. for Microgel4000-10, Microgel2000-10 and Microgel-IN. The relative viscosity dependence on concentration showed an unusual viscosity plateau between the concentration range 2-7% wt. This unusual behaviour is explained by considering the particles to be elongated rather than spheres which leads to the reasoning as of why the microgels are shear-thinning and why Krieger-Dougherty is not the best model for our system. The dilute centrifuged suspension are found not to age with time making it feasible to use the same prepared ssuspension for the filtration experiments for over 15 days. The centrifuged suspensions are found to be more viscous than elastic. We showed an interesting phenomenon of shear-induced aggregation in the microgel suspensions with the aid of linear viscoelasticity measurements and changes in viscosity after the application of high deformation. Of course, more detailed and systematic investigation is needed to understand this phenomenon perhaps at different concentrations and temperatures to also see their effect on aggregation. We quantitatively show the affinity of the microgel suspension towards hydrophilic surface. We need further investigation to fully understand the particle-wall interactions. We also show the possibility of getting some quantitative idea of jamming fraction

by a simple experiment consisting of drying of a microgel droplet and optically monitoring the change in the grayscale intensity and in the shape of the droplet. Our results in regards with the jamming concentration are more or less consistent with the results obtained from bulk rheology. In model porous media for frontal filtration, we show the progressive jamming of the initially dilute microgel suspension with an average particle size of 27 µm. This jamming is explained in terms of the shear-induced aggregation of the suspension when it undergoes a high shear in the pores of the porous media. The initially dilute suspension forms aggregate and eventually a gel like mass after passing through the pores, in the region of low shear rate where the wall stresses are lower than the yield stress of the aggregates. We have shown the effects of flowrates, surface wettabilities and particle/pore size ratio on the jamming. In porous media for lateral filtration, we demonstrate the phenomenon of building up of the filter cake formed as a results of particle aggregation and the eventual fluid loss control in terms of the rapid decrease in the flowrate within few minutes. We have shown a technique to precisely measure the permeability of the microgel filter cake formed as a result of compression. The filter cake is found to be very dense, highly elastic, have a yield stress and have low permeability of the order of 10^{-19} m^2. The permeability calculated for the filter cake inside frontal and lateral channels show a higher value as compared to these values mainly because the filter cake formed in the channels is not dense but loose.

References

1. Alemdar, A., Öztekin, N., Güngör, N., Ece, Ö. I., & Erim, F. B. (2005). Effects of polyethyleneimine adsorption on the rheological properties of purified bentonite suspensions. *Colloids and Surfaces A: Physicochemical and Engineering Aspects, 252*(2), 95-98. doi:https://doi.org/10.1016/j.colsurfa.2004.10.009
2. Alexander, F. R. (2013). Drying of thin colloidal films. *Reports on Progress in Physics, 76*(4), 046603.
3. Ambari, A., Amiel, C., Gauthier-Manuel, B., & Guyon, E. (1986). An experimental measurement of the permeability of deformable porous media. *Rev. Phys. Appl. (Paris), 21*(1), 53-58.
4. Baba Hamed, S., & Belhadri, M. (2009). Rheological properties of biopolymers drilling fluids. *Journal of Petroleum Science and Engineering, 67*(3), 84-90. doi:https://doi.org/10.1016/j.petrol.2009.04.001
5. Baker, W. O. (1949). Microgel, A New Macromolecule. *Industrial & Engineering Chemistry, 41*(3), 511-520. doi:10.1021/ie50471a016
6. Ball, R. C., & Richmond, P. (1980). Dynamics of Colloidal Dispersions. *Physics and Chemistry of Liquids, 9*(2), 99-116. doi:10.1080/00319108008084770
7. Barnes, H. A., Hutton, J. F., & Walters, K. (1989). *An Introduction to Rheology*: Elsevier.
8. Bartlit., F. H. (2011). *Macondo the gulf oil disaster*. Retrieved from
9. Batchelor, G. K. (2006). The effect of Brownian motion on the bulk stress in a suspension of spherical particles. *Journal of Fluid Mechanics, 83*(1), 97-117. doi:10.1017/S0022112077001062
10. Benchabane, A., & Bekkour, K. (2006). Effects of anionic additives on the rheological behavior of aqueous calcium montmorillonite suspensions. *Rheologica Acta, 45*(4), 425-434. doi:10.1007/s00397-005-0063-1

11. Berejnov, V., Djilali, N., & Sinton, D. (2008). Lab-on-chip methodologies for the study of transport in porous media: energy applications. *Lab on a Chip, 8*(5), 689-693. doi:10.1039/B802373P
12. Bhattacharya, S., Datta, A., Berg, J. M., & Gangopadhyay, S. (2005). Studies on surface wettability of poly(dimethyl) siloxane (PDMS) and glass under oxygen-plasma treatment and correlation with bond strength. *Journal of Microelectromechanical Systems, 14*(3), 590-597. doi:10.1109/JMEMS.2005.844746
13. Bird, R. B. (2010). Chemical Engineering Education: A Gallimaufry of Thoughts. *Annual Review of Chemical and Biomolecular Engineering, 1*(1), 1-17. doi:10.1146/annurev-chembioeng-073009-100922
14. Borrega, R., Cloitre, M., Betremieux, I., Ernst, B., & Leibler, L. (1999). Concentration dependence of the low-shear viscosity of polyelectrolyte micro-networks: From hard spheres to soft microgels. *EPL (Europhysics Letters), 47*(6), 729.
15. Bulkley, W. H. H. a. R. (1926). Konsistenzmessungen von Gummi-Benzollösungen. *Kolloid-Zeitschrift, 39*, 291--300. doi:https://doi.org/10.1007%2Fbf01432034
16. Cazabat, A.-M., & Guéna, G. (2010). Evaporation of macroscopic sessile droplets. *Soft Matter, 6*(12), 2591-2612. doi:10.1039/B924477H
17. . Chapter 1 - Drilling muds. (2015). In J. Fink (Ed.), *Petroleum Engineer's Guide to Oil Field Chemicals and Fluids (Second Edition)* (pp. 1-61). Boston: Gulf Professional Publishing.
18. . Chapter 2 - Fluid loss additives. (2015). In J. Fink (Ed.), *Petroleum Engineer's Guide to Oil Field Chemicals and Fluids (Second Edition)* (pp. 63-120). Boston: Gulf Professional Publishing.
19. Clément, F., & Leng, J. (2004). Evaporation of Liquids and Solutions in Confined Geometry. *Langmuir, 20*(16), 6538-6541. doi:10.1021/la0495534
20. Cloitre, M. (2011). Yielding, Flow, and Slip in Microgel Suspensions: From Microstructure to Macroscopic Rheology. *Microgel Suspensions*. doi:doi:10.1002/9783527632992.ch11

21. 10.1002/9783527632992.ch11
22. Cloitre, M., Borrega, R., Monti, F., & Leibler, L. (2003). Structure and flow of polyelectrolyte microgels: from suspensions to glasses. *Comptes Rendus Physique, 4*(2), 221-230. doi:https://doi.org/10.1016/S1631-0705(03)00046-X
23. Coussot, P., Bertrand, F., & Herzhaft, B. (2004). Rheological Behavior of Drilling Muds, Characterization Using Mri Visualization. *Oil & Gas Science and Technology - Rev. IFP, 59*(1), 23-29.
24. D Haw, M. (2004). *Jamming, Two-Fluid Behavior, and "Self-Filtration" in Concentrated Particulate Suspensions* (Vol. 92).
25. Darcy, H. (1856). *Les Fontaines Publiques de la Ville de Dijon*.
26. Decock, J. r. m. (2017). *Approches micro/milli-fluidiques pour l'étude in situ de procédés de filtration frontale.* Retrieved from http://www.theses.fr/2017BORD0788/document Available from http://www.theses.fr/2017BORD0788
27. Deegan, R. D., Bakajin, O., Dupont, T. F., Huber, G., Nagel, S. R., & Witten, T. A. (1997). Capillary flow as the cause of ring stains from dried liquid drops. *Nature, 389*, 827. doi:10.1038/39827
28. Delhommer, H. J. H., TX), Walker, Clarence O. (Richmond, TX). (1987). United States Patent No.
29. Duchěne, D., Touchard, F., & Peppas, N. A. (1988). Pharmaceutical and Medical Aspects of Bioadhesive Systems for Drug Administration. *Drug Development and Industrial Pharmacy, 14*(2-3), 283-318. doi:10.3109/03639048809151972
30. Duffy, D. C., McDonald, J. C., Schueller, O. J. A., & Whitesides, G. M. (1998). Rapid Prototyping of Microfluidic Systems in Poly(dimethylsiloxane). *Analytical Chemistry, 70*(23), 4974-4984. doi:10.1021/ac980656z
31. Einstein, A. (1906). A new determination of molecular dimensions. *Ann. phys, 19*(2), 289-306.

32. Engmann, J., Servais, C., & Burbidge, A. S. (2005). Squeeze flow theory and applications to rheometry: A review. *Journal of Non-Newtonian Fluid Mechanics, 132*(1), 1-27. doi:https://doi.org/10.1016/j.jnnfm.2005.08.007

33. Ferer, M., Ji, C., Bromhal, G. S., Cook, J., Ahmadi, G., & Smith, D. H. (2004). Crossover from capillary fingering to viscous fingering for immiscible unstable flow: Experiment and modeling. *Physical Review E, 70*(1), 016303. doi:10.1103/PhysRevE.70.016303

34. Fink, J. (2015). *Petroleum Engineer's*

35. Guide to Oil Field

36. *Chemicals and Fluids*.

37. Fuerstman, M. J., Lai, A., Thurlow, M. E., Shevkoplyas, S. S., Stone, H. A., & Whitesides, G. M. (2007). The pressure drop along rectangular microchannels containing bubbles. *Lab on a Chip, 7*(11), 1479-1489. doi:10.1039/B706549C

38. Glowka, D. A., Loeppke, G. E., Rand, P. B., & Wright, E. K. (1989, 1989-01-01). *Laboratory and field evaluation of polyurethane foam for lost circulation control*, United States.

39. Guery, J., Bertrand, E., Rouzeau, C., Levitz, P., Weitz, D. A., & Bibette, J. (2006). Irreversible Shear-Activated Aggregation in Non-Brownian Suspensions. *Physical Review Letters, 96*(19), 198301. doi:10.1103/PhysRevLett.96.198301

40. Guichard, B. V., FR), Wood, Barry (Hornchurch, GB), Vongphouthone, Patrick (Sceaux, FR). (2008). United States Patent No.

41. Hamida, T., Kuru, E., & Pickard, M. (2009). Rheological characteristics of aqueous waxy hull-less barley (WHB) solutions. *Journal of Petroleum Science and Engineering, 69*(3), 163-173. doi:https://doi.org/10.1016/j.petrol.2009.08.003

42. Happel, J. (1957). Viscosity of Suspensions of Uniform Spheres. *Journal of Applied Physics, 28*(11), 1288-1292. doi:10.1063/1.1722635

43. Hartnett, J. P., & Kostic, M. (1989). Heat Transfer to Newtonian and Non-Newtonian Fluids in Rectangular Ducts. In J. P. Hartnett & T. F. Irvine (Eds.), *Advances in Heat Transfer* (Vol. 19, pp. 247-356): Elsevier.

44. Herzig, J. P., Leclerc, D. M., & Goff, P. L. (1970). Flow of Suspensions through Porous Media—Application to Deep Filtration. *Industrial & Engineering Chemistry, 62*(5), 8-35. doi:10.1021/ie50725a003

45. Hillborg, H., Ankner, J. F., Gedde, U. W., Smith, G. D., Yasuda, H. K., & Wikström, K. (2000). Crosslinked polydimethylsiloxane exposed to oxygen plasma studied by neutron reflectometry and other surface specific techniques. *Polymer, 41*(18), 6851-6863. doi:https://doi.org/10.1016/S0032-3861(00)00039-2

46. Hillborg, H., & Gedde, U. W. (1998). Hydrophobicity recovery of polydimethylsiloxane after exposure to corona discharges. *Polymer, 39*(10), 1991-1998. doi:https://doi.org/10.1016/S0032-3861(97)00484-9

47. Holthoff, H., Schmitt, A., Fernández-Barbero, A., Borkovec, M., Cabrerízo-Vílchez, M. á., Schurtenberger, P., & Hidalgo-álvarez, R. (1997). Measurement of Absolute Coagulation Rate Constants for Colloidal Particles: Comparison of Single and Multiparticle Light Scattering Techniques. *Journal of Colloid and Interface Science, 192*(2), 463-470. doi:https://doi.org/10.1006/jcis.1997.5022

48. Hung, T. C., Hochmuth, R. M., Joist, J. H., & Sutera, S. P. (1976). SHEAR-INDUCED AGGREGATION AND LYSIS OF PLATELETS. *ASAIO Journal, 22*(1).

49. İşci, S., Günister, E., Ece, Ö. I., & Güngör, N. (2004). The modification of rheologic properties of clays with PVA effect. *Materials Letters, 58*(12), 1975-1978. doi:https://doi.org/10.1016/j.matlet.2004.01.001

50. J, P. s. e. J. a. R. (1998). Transmitted-light microscopy for biology:

51. a physicist's point of view, part 2. *Proceedings of the Royal*

52. *Microscopical Society, 36*, 196–205.

53. James, D. F., & McLaren, D. R. (2006). The laminar flow of dilute polymer solutions through porous media. *Journal of Fluid Mechanics, 70*(4), 733-752. doi:10.1017/S0022112075002327

54. Jean, B., Emanuel, B., Nicolas, L., & Jérôme, B. (2004). Bio-specific recognition and applications: from molecular to colloidal scales. *Journal of Physics: Condensed Matter, 16*(15), R469.

55. Jeffrey, D. J., & Acrivos, A. (1976). The rheological properties of suspensions of rigid particles. *AIChE Journal, 22*(3), 417-432. doi:10.1002/aic.690220303

56. Jen, C. J., & McIntire, L. V. (1984). Characteristics of shear-induced aggregation in whole blood. *The Journal of Laboratory and Clinical Medicine, 103*(1), 115-124. doi:10.5555/uri:pii:0022214384901598

57. Kelessidis, V. C., Poulakakis, E., & Chatzistamou, V. (2011). Use of Carbopol 980 and carboxymethyl cellulose polymers as rheology modifiers of sodium-bentonite water dispersions. *Applied Clay Science, 54*(1), 63-69. doi:https://doi.org/10.1016/j.clay.2011.07.013

58. Ketz, R. J., Prud'homme, R. K., & Graessley, W. W. (1988). Rheology of concentrated microgel solutions. *Rheologica Acta, 27*(5), 531-539. doi:10.1007/BF01329353

59. Kohn, R. S. S., NJ). (1988). United States Patent No.

60. Krieger, I. M., & Dougherty, T. J. (1959). A Mechanism for Non‐Newtonian Flow in Suspensions of Rigid Spheres. *Transactions of the Society of Rheology, 3*(1), 137-152. doi:10.1122/1.548848

61. Kulicke, W. M., & Haas, R. (1984). Flow behavior of dilute polyacrylamide solutions through porous media. 1. Influence of chain length, concentration, and thermodynamic quality of the solvent. *Industrial & Engineering Chemistry Fundamentals, 23*(3), 308-315. doi:10.1021/i100015a008

62. Leng, J. (2010). Drying of a colloidal suspension in confined geometry. *Physical Review E, 82*(2), 021405. doi:10.1103/PhysRevE.82.021405

63. Litster, S., Sinton, D., & Djilali, N. (2006). Ex situ visualization of liquid water transport in PEM fuel cell gas diffusion layers. *Journal of Power Sources, 154*(1), 95-105. doi:https://doi.org/10.1016/j.jpowsour.2005.03.199

64. Loosveldt, H., Lafhaj, Z., & Skoczylas, F. (2002). Experimental study of gas and liquid permeability of a mortar. *Cement and Concrete Research, 32*(9), 1357-1363. doi:https://doi.org/10.1016/S0008-8846(02)00793-7

65. Macosko, C. W., & Larson, R. G. (1994). Rheology: principles, measurements, and applications.

66. Makamba, H., Kim, J. H., Lim, K., Park, N., & Hahn, J. H. (2003). Surface modification of poly(dimethylsiloxane) microchannels. *ELECTROPHORESIS, 24*(21), 3607-3619. doi:doi:10.1002/elps.200305627

67. Marshall, R. J., & Metzner, A. B. (1967). Flow of Viscoelastic Fluids through Porous Media. *Industrial & Engineering Chemistry Fundamentals, 6*(3), 393-400. doi:10.1021/i160023a012

68. Mata, A., Fleischman, A. J., & Roy, S. (2005). Characterization of Polydimethylsiloxane (PDMS) Properties for Biomedical Micro/Nanosystems. *Biomedical Microdevices, 7*(4), 281-293. doi:10.1007/s10544-005-6070-2

69. Mewis, J., & Wagner, N. J. (2009). Current trends in suspension rheology. *Journal of Non-Newtonian Fluid Mechanics, 157*(3), 147-150. doi:https://doi.org/10.1016/j.jnnfm.2008.11.004

70. Mooney, M. (1951). The viscosity of a concentrated suspension of spherical particles. *Journal of Colloid Science, 6*(2), 162-170. doi:https://doi.org/10.1016/0095-8522(51)90036-0

71. Morra, M., Occhiello, E., Marola, R., Garbassi, F., Humphrey, P., & Johnson, D. (1990). On the aging of oxygen plasma-treated polydimethylsiloxane surfaces. *Journal of Colloid and Interface Science, 137*(1), 11-24. doi:https://doi.org/10.1016/0021-9797(90)90038-P

72. Newton, I. (1687). *Philosophiae naturalis principia mathematica*. Londini: Jussu Societatis Regiæ ac Typis Josephi Streater. Prostat apud plures Bibliopolas.
73. Oates, K. M. N., Krause, W. E., Jones, R. L., & Colby, R. H. (2006). Rheopexy of synovial fluid and protein aggregation. *Journal of The Royal Society Interface, 3*(6), 167.
74. Pabst, W., Gregorová, E., & Berthold, C. (2006). Particle shape and suspension rheology of short-fiber systems. *Journal of the European Ceramic Society, 26*(1), 149-160. doi:https://doi.org/10.1016/j.jeurceramsoc.2004.10.016
75. Perrin, C. L., Tardy, P. M. J., Sorbie, K. S., & Crawshaw, J. C. (2006). Experimental and modeling study of Newtonian and non-Newtonian fluid flow in pore network micromodels. *Journal of Colloid and Interface Science, 295*(2), 542-550. doi:https://doi.org/10.1016/j.jcis.2005.09.012
76. Peterson, D. M., Stathopoulos, N. A., Giorgio, T. D., Hellums, J. D., & Moake, J. L. (1987). Shear-induced platelet aggregation requires von Willebrand factor and platelet membrane glycoproteins Ib and IIb-IIIa. *Blood, 69*(2), 625.
77. Poon, W. C. K., Weeks, E. R., & Royall, C. P. (2012). On measuring colloidal volume fractions. *Soft Matter, 8*(1), 21-30. doi:10.1039/C1SM06083J
78. Psaltis, D., & Fainman, Y. (2006). *Optofluidics*.
79. Rammensee, S., Slotta, U., Scheibel, T., & Bausch, A. R. (2008). Assembly mechanism of recombinant spider silk proteins. *Proceedings of the National Academy of Sciences, 105*(18), 6590.
80. Rawle, A. F. (2010). *Analytical Tools for Suspension Characterization*. New York, NY: Springer.
81. Rousseau, D., Chauveteau, G., Renard, M., Tabary, R., Zaitoun, A., Mallo, P., . . . Omari, A. (2005). *Rheology and Transport in Porous Media of New Water Shutoff / Conformance Control Microgels*. Paper presented at the SPE International Symposium on Oilfield Chemistry, The Woodlands, Texas.

82. Russel W.B, S. D. A., Schowalter W. R. (1989). *Colloidal Dispersions*: Cambridge University press.

83. Sadowski, T. J., & Bird, R. B. (1965). Non‐Newtonian Flow through Porous Media. I. Theoretical. *Transactions of the Society of Rheology, 9*(2), 243-250. doi:10.1122/1.549000

84. Saunders, B. R., & Vincent, B. (1999). Microgel particles as model colloids: theory, properties and applications. *Advances in Colloid and Interface Science, 80*(1), 1-25. doi:https://doi.org/10.1016/S0001-8686(98)00071-2

85. Savins, J. G. (1969). NON-NEWTONIAN FLOW THROUGH POROUS MEDIA. *Industrial & Engineering Chemistry, 61*(10), 18-47. doi:10.1021/ie50718a005

86. Sendekie, Z. B., & Bacchin, P. (2016). Colloidal Jamming Dynamics in Microchannel Bottlenecks. *Langmuir, 32*(6), 1478-1488. doi:10.1021/acs.langmuir.5b04218

87. Senff, H., & Richtering, W. (1999). Temperature sensitive microgel suspensions: Colloidal phase behavior and rheology of soft spheres. *The Journal of Chemical Physics, 111*(4), 1705-1711. doi:10.1063/1.479430

88. Seyssiecq, I., Ferrasse, J.-H., & Roche, N. (2003). State-of-the-art: rheological characterisation of wastewater treatment sludge. *Biochemical Engineering Journal, 16*(1), 41-56. doi:https://doi.org/10.1016/S1369-703X(03)00021-4

89. Son, Y. (2007). Determination of shear viscosity and shear rate from pressure drop and flow rate relationship in a rectangular channel. *Polymer, 48*(2), 632-637. doi:https://doi.org/10.1016/j.polymer.2006.11.048

90. Staudinger, H., & Husemann, E. (1935). Über hochpolymere Verbindungen, 116. Mitteil.: Über das begrenzt quellbare Poly‐styrol. *Berichte der deutschen chemischen Gesellschaft (A and B Series), 68*(8), 1618-1634. doi:10.1002/cber.19350680841

91. Stokes, J. R., & Frith, W. J. (2008). Rheology of gelling and yielding soft matter systems. *Soft Matter, 4*(6), 1133-1140. doi:10.1039/B719677F

92. Sydansk, R. D. L., CO). (1990). United States Patent No.

93. Tamburic, S., & Craig, D. Q. M. (1995). An investigation into the rheological, dielectric and mucoadhesive properties of poly(acrylic acid) gel systems. *Journal of Controlled Release, 37*(1), 59-68. doi:https://doi.org/10.1016/0168-3659(95)00064-F

94. Tan, B. H., Pelton, R. H., & Tam, K. C. (2010). Microstructure and rheological properties of thermo-responsive poly(N-isopropylacrylamide) microgels. *Polymer, 51*(14), 3238-3243. doi:https://doi.org/10.1016/j.polymer.2010.04.059

95. Tan, B. H., Tam, K. C., Lam, Y. C., & Tan, C. B. (2005). Microstructure and rheological properties of pH-responsive core–shell particles. *Polymer, 46*(23), 10066-10076. doi:https://doi.org/10.1016/j.polymer.2005.08.007

96. Tirumkudulu, M. S., & Russel, W. B. (2005). Cracking in Drying Latex Films. *Langmuir, 21*(11), 4938-4948. doi:10.1021/la048298k

97. van der Werff, J. C., & de Kruif, C. G. (1989). Hard‐sphere Colloidal Dispersions: The Scaling of Rheological Properties with Particle Size, Volume Fraction, and Shear Rate. *Journal of Rheology, 33*(3), 421-454. doi:10.1122/1.550062

98. Wakadikar, K., Sil, A., Kolekar, N., Tandon, S., & Kumar, R. (2011). *Effect of non-aqueous drilling fluid and its synthetic base oil on soil health as indicated by its dehydrogenase activity* (Vol. 64).

99. Walker, C. O. R., TX). (1986). United States Patent No.

100. Walker, C. O. R., TX). (1987). United States Patent No.

101. Wu, H., Zaccone, A., Tsoutsoura, A., Lattuada, M., & Morbidelli, M. (2009). High Shear-Induced Gelation of Charge-Stabilized Colloids in a Microchannel without Adding Electrolytes. *Langmuir, 25*(8), 4715-4723. doi:10.1021/la803789s

102. Wyckoff, R. D., Botset, H. G., Muskat, M., & Reed, D. W. (1933). The Measurement of the Permeability of Porous Media for Homogeneous Fluids. *Review of Scientific Instruments, 4*(7), 394-405. doi:10.1063/1.1749155

103. Wyss, H. M., Blair, D. L., Morris, J. F., Stone, H. A., & Weitz, D. A. (2006). Mechanism for clogging of microchannels. *Physical Review E, 74*(6), 061402. doi:10.1103/PhysRevE.74.061402

104. Xia, Y., & Whitesides, G. M. (1998). Soft Lithography. *Angewandte Chemie International Edition, 37*(5), 550-575. doi:10.1002/(SICI)1521-3773(19980316)37:5<550::AID-ANIE550>3.0.CO;2-G

105. Xie, D., Wu, H., Zaccone, A., Braun, L., Chen, H., & Morbidelli, M. (2010). Criticality for shear-induced gelation of charge-stabilized colloids. *Soft Matter, 6*(12), 2692-2698. doi:10.1039/C002043E

106. Xu, S., & Sun, Z. (2011). Progress in coagulation rate measurements of colloidal dispersions. *Soft Matter, 7*(24), 11298-11308. doi:10.1039/C1SM06237A

107. Zaccone, A., Gentili, D., Wu, H., Morbidelli, M., & Del Gado, E. (2011). Shear-Driven Solidification of Dilute Colloidal Suspensions. *Physical Review Letters, 106*(13), 138301. doi:10.1103/PhysRevLett.106.138301